Generation of Short Pulse THz Radiation from Accelerator Based Light Sources



Thakonwat Chanwattana
St. Cross College
University of Oxford

Thesis submitted in fulfilment of the requirements for the degree of Doctor of Philosophy at the University of Oxford

Trinity Term 2016

Generation of Short Pulse THz Radiation from Accelerator Based Light Sources

Thakonwat Chanwattana, St. Cross College, University of Oxford

Thesis submitted in fulfilment of the requirements for the degree of Doctor of Philosophy at the University of Oxford

Trinity Term, 2016

Abstract

High power and short pulse THz radiation has become increasingly important in the investigation of dynamics of organic and chemical molecules. Such radiation can be effectively generated with accelerator-based light sources. This thesis reports a series of studies on the generation of short pulse THz radiation from storage rings and from compact accelerators that can be based in University sized laboratories. The first part of this thesis reviews THz radiation, synchrotron radiation and free electron laser (FEL). The second part presents the studies of short pulse THz radiation generated from the Diamond storage ring in a new operating mode known as ultra-low alpha mode to extend spectrum of coherent radiation to higher THz frequency. The numerical simulations of a single bunch dynamics show qualitative agreements with the measurements taken at the Diamond storage ring. The third part is dedicated to the design of a compact RF linac-based THz radiation source for producing short pulse THz self-amplified spontaneous emission (SASE) FEL with an undulator and THz coherent synchrotron radiation (CSR) with a bending magnet. Start-to-end simulations of SASE FEL and CSR were performed to analyse the beam dynamics and the generation of THz radiation. The SASE FEL reaches saturation within the undulator length of 5 m, whereas the CSR spectrum covers frequency below 16 THz. In the fourth part, we investigated a THz/IR radiation source driven by a Laser Plasma Wakefield Accelerator (LPWA). Extensive 2D particle-in-cell (PIC) simulations were done to generate an ultra-short electron bunch from self-injection in a nonlinear bubble regime. The 60-MeV electron bunch was obtained with 6% energy spread and 18 mrad beam divergence. The self-injected electron beam was used to drive the SASE FEL using a normal undulator and a transverse gradient undulator (TGU) to exploit the electron bunch with large energy spread. The results show that the energy spread of 6% is too large even for the TGU. Although the energy spread is reduced to 1%, the FEL saturation cannot be reached because the bunch length of the LPWA driven beam is shorter than the FEL cooperation length. The last part of this thesis discusses the Accelerator Science Laboratory (ASL) project at the University of Oxford. The designs of THz radiation sources driven by the RF linac and the LPWA previously presented were considered as potential options for the ASL. The radiation shielding for the ASL was investigated with Monte Carlo simulations to design a proper beam dump and shielding covering the beam dump.

Acknowledgements

I would like to give my first thanks to my supervisor Professor Riccardo Bartolini who has offered great guidance and shared his knowledge and experience in Accelerator Physics and light sources with me throughout my DPhil. He is also a role model of a physicist who works hard and dedicates his life for research. My second thanks go to my co-supervisor Professor Emmanuel Tsesmelis who has always been supportive. He gave great guidance and support both at Oxford and at CERN with helpful support from Ilias Efthymiopoulos. Thanks to lecturers and staffs of John Adams Institute of Accelerator Science and Particle Physics Sub-department who provided helpful training and support during my study. Many discussions essential for my thesis were provided by colleagues at Diamond Light Source, especially Accelerator Physics group and Diagnostic group, and are gratefully acknowledged. I would also like to thank to my college St. Cross College for providing great welfare support.

I would like to express my gratitude to Ministry of Science and Technology, the Royal Thai Government and Synchrotron Light Research Institute, Thailand who have funded my DPhil study.

I thank all my friends in the UK and Thailand who always provide cheerful support and friendship. I am greatly thankful to my best friend Patcha Sooksabai. She always encourages me and makes me feel better with her extremely positive thinking. Thanks to my whole big family, in particular my parents, brother and sister. I could not have done everything in my life without their support, their love and care. I know they are always proud of me and I will do my best to take care of them upon my return. I cannot end this acknowledgement without giving my final thanks to myself for being patience and determined to complete this work and to overcome all difficult situations that arose in my life.

Contents

Abstract ..... **ii**
Acknowledgements ..... **iii**
Contents ..... **iv**
List of Figures ..... **vii**
List of Tables ..... **xiv**
Chapter 1 THz and Short Pulse Radiation **1**
1.1 Introduction 1
1.2 THz Radiation Sources 3
1.2.1 Accelerator based THz Radiation sources 4
1.3 Synchrotron Radiation 6
1.3.1 Synchrotron radiation from a dipole bending magnet 8
1.3.2 Synchrotron radiation from insertion devices 11
1.4 Coherent Synchrotron Radiation 14
1.5 Free Electron Laser 16
1.5.1 Self-amplification spontaneous emission 18
1.5.2 The FEL parameterisation 18
1.6 Compact THz radiation sources 22
1.7 Thesis Layout 23
Chapter 2 Generation of Short Pulse THz radiation with Storage Rings **24**
2.1 Background of low alpha operating mode 26
2.1.1 Relation between natural bunch length and alpha in storage rings 26
2.1.2 Low alpha lattice 27
2.1.3 Collective effects in storage rings 29
2.1.4 Relevant longitudinal impedance sources 32
2.2 Simulations of beam dynamics in storage rings 34
2.2.1 Single bunch tracking code 35
2.2.2 Tracking simulations of THz radiation 37
2.3 Simulations of THz CSR generated in ultra-low alpha mode in Diamond storage ring 55
2.3.1 Bunch lengthening 57

2.3.2 Spectrogram 58
2.3.3 CSR spectrum 59
2.3.4 Longitudinal phase space 60
2.4 Measurements of THz CSR generated in ultra-low alpha mode 62
2.4.1 Measurement techniques for diagnostics of CSR in Diamond storage ring 62
2.4.2 Measurements of CSR generated from ultra-low alpha mode in Diamond storage ring 66
2.5 Summary of comparisons of THz ultra-low alpha operating mode at Diamond storage ring 73
2.5.1 Bunch lengthening 73
2.5.2 Spectrogram 75
2.5.3 FTIR spectrum 75
2.6 Summary 76
Chapter 3 THz Radiation and Short Pulses with an RF Linac 78
3.1 RF linac driven THz radiation source 79
3.2 Accelerator physics in linac-based sources 81
3.2.1 Beam generation 81
3.2.2 Bunch compression 86
3.2.3 Radiation generation 91
3.3 Start-to-End Simulations 91
3.3.1 THz FEL 92
3.3.2 THz CSR source 105
3.4 Summary 115
Chapter 4 THz Radiation and Short Pulses with a LPWA 118
4.1 Physics of laser plasma acceleration 119
4.1.1 Excitation of plasma wakefield by an intense laser pulse 120
4.1.2 Laser plasma wakefield acceleration in the bubble regime 123
4.1.3 Self-injection in the bubble regime 125
4.1.4 Self-focussing and matching conditions of the laser 125
4.1.5 Energy gain in plasma acceleration 126
4.2 Simulation of a self-injected electron beam 128
4.2.1 Particle-in-cell simulation 128
4.2.2 2D PIC simulation of nonlinear LPWA 129

4.3 FEL driven by large energy spread beam using a transverse gradient undulator 137
4.3.1 Analysis of FELs driven LPWA and transverse gradient undulator 139
4.4 Summary 146
Chapter 5 The Accelerator Science Laboratory 148
5.1 Proposal of Accelerator Science Laboratory 149
5.2 Design of compact radiation sources for the ASL 150
5.3 Radiation safety of the ASL 152
5.3.1 Quantities related to radiation protection 154
5.3.2 Radiation levels 155
5.3.3 Simulations of radiation shielding for the ASL 156
5.4 Summary 164
Chapter 6 Conclusion 165
6.1 Generation of Short Pulse THz Radiation with Storage Rings 165
6.2 THz Radiation and Short Pulses with an RF Linac 166
6.3 THz Radiation and Short Pulses with a LPWA 167
6.4 The Accelerator Science Laboratory 168
6.5 Conclusion 169
Related Publications 171
Appendix A Single Particle Dynamics 172
A.1 Longitudinal dynamics 172
A.2 One turn map in longitudinal phase space in storage rings 173
A.3 Transverse dynamics 174
A.4 One turn map in transverse phase space in storage rings 176
Bibliography 179

List of Figures

1.1 Synchrotron radiation in (a) centre of mass frame and (b) laboratory frame. 9

1.2 Frequency distribution of synchrotron radiation of an electron from a bending magnet with a bending radius $\rho = 1.72\ m$ at the energy of 20, 40 and 60 MeV. 10

1.3 An example of insertion device with the gap width g and the period length λ_u. 11

1.4 Distribution of radiation in the harmonics as a function of the horizontal angle (left), of the undulator parameter (middle) and line-shape spectrum of the planar undulator radiation (right) [34]. 14

1.5 Frequency distribution of ISR (black solid line) and CSR (red solid line) emitted from a 500-pC bunch with rms bunch length of 200 fs (60 μm) at 60 MeV in a bending magnet of bending radius 1.72 m. The black dashed line and the red dashed line show the critical frequency and the frequency associated to the inverse bunch length Equation (1.25), respectively. 16

1.6 Phase condition to sustain energy transfer between electric field of synchrotron radiation and an electron [36]. 17

2.1 Dispersion function in a dipole for standard user mode (left), low alpha with high emittance (middle), and low alpha with low emittance (right) lattices. 29

2.2 Wakefield represented by electric field lines produced by the charged particle q traveling at the speed of light [48]. 31

2.3 Diagram flow of the simulation of the single bunch dynamics with *sbtrack*. The turn-by-turn output include the 6D phase space, bunch profiles, and the THz signal received by a detector in a given bandwidth. 36

2.4 Longitudinal phase space of Diamond standard optics in nominal alpha mode at bunch current 1, 10, 100 μA and 1 mA. 40

2.5 Radiated power in time domain (left) and in frequency domain (right) in the range of 33-50 GHz of an electron bunch in nominal alpha mode. The top plots refer to 10 μA the bottom plots refer to 100 μA. 41

2.6 Longitudinal bunch profile in 30000th turn in nominal alpha mode at different bunch current. 42

2.7 Form factor in 30000th turn given by Fourier transform of the profile at bunch current 10 μA, 100 μA and 1 mA operated in nominal alpha. 42

2.8 Bunch lengthening with bunch current in nominal alpha operation. 43

2.9 Longitudinal phase space in standard low alpha mode at bunch current 1, 10, 100 μA and 1 mA, after 30000 turns. 44

2.10 Longitudinal phase space of $\alpha = -1 \times 10^{-5}$ and RF voltage of 3 MV at 100 μA. The phase space rotates clockwise. 44

2.11 Radiated power in time domain (left) and in frequency domain (right) in the range of 33-50 GHz of an electron bunch in standard low alpha mode. The top plots refer to 10 μA the bottom plots refer to 100 μA. 45

2.12 Longitudinal bunch profile of a bunch in standard low alpha mode after 30000 turns at 10 μA (left) and at 100 μA (right). 46

2.13 Form factor given by Fourier transform of the profile at bunch current 10 μA (left) and 100 μA (right) operated in standard low alpha mode. 46

2.14 Bunch lengthening in standard low alpha mode. Compare with Figure 2.8 for the bunch lengthening curve for nominal operating parameters. 47

2.15 Simulated spectrogram from standard low alpha mode in eight bandwidths of SBDs available at Diamond. 49

2.16 Longitudinal phase space in positive low alpha mode at bunch current 1, 10, 100 μA and 1 mA after 30000 turns. 51

2.17 Longitudinal phase space of $\alpha = +1 \times 10^{-5}$ and RF voltage of 3 MV at 100 μA. The phase space rotates anticlockwise. 51

2.18 Radiated power in time domain (left) and in frequency domain (right) in the range of 33-50 GHz of an electron bunch in positive low alpha mode. Top plots refer to 10 μA and bottom plots refer to 100 μA. 52

2.19 Longitudinal bunch profile in positive low alpha mode after 30000 turns at 10 μA (left) and at 100 μA (right). 53

2.20 Form factor given by Fourier transform of the profile operated in positive low alpha mode. Left plot refers to 10 μA and right plot refers to 100 μA. 53

2.21 Bunch lengthening in positive low alpha mode. Compare with Figure 2.14 for the bunch lengthening curve for standard low alpha mode. 53

2.22 Simulated spectrogram from positive low alpha mode in eight bandwidths of SBDs available at Diamond. 54

2.23 Simulated rms bunch length as a function of the single bunch current for $\alpha = -2 \times 10^{-6}$ (blue) and $\alpha = -1 \times 10^{-6}$ (red). The circles are the theoretical values for the zero current bunch length. This can be compared with the simulated rms bunch length for low alpha mode shown in Figure 2.14 (valid for negative alpha). 57

2.24 Simulated spectrogram for $\alpha = -2 \times 10^{-6}$ in the specific ranges of the SBD detectors. 58

2.25 Simulated spectrogram for $\alpha = -1 \times 10^{-6}$ in the specific ranges of the SBD detectors. 59

2.26 Form factor of the simulated bunch for $\alpha = -2 \times 10^{-6}$ at 10 μA. 60

2.27 Form factor of the simulated bunch for $\alpha = -1 \times 10^{-6}$ at 10 μA. 60

2.28 Longitudinal phase space for a case with $\alpha = -2 \times 10^{-6}$ at 10 μA. 61

2.29 Longitudinal phase space for a case with $\alpha = -1 \times 10^{-6}$ at 10 μA. 61

2.30 Arrangement of array of SBDs [60]. 63

2.31 The schematic of Michaelson interferometer for FTIR interferometer [61]. 64

2.32 Basic configuration of the conventional streak camera [63]. 66

2.33 Measured rms bunch length of $\alpha = -2 \times 10^{-6}$ (blue, solid) and $\alpha = -1 \times 10^{-6}$ (red, dashed) from the streak camera. 67

2.34 CSR spectrograms for $\alpha = -2 \times 10^{-6}$ measured with 8 SBD channels. 68

2.35 CSR spectrograms for $\alpha = -1 \times 10^{-6}$ measured with 8 SBD channels. 69

2.36 Spectra for $\alpha = -2 \times 10^{-6}$ measured with FTIR interferometer at different bunch current. 70

2.37 Spectra for $\alpha = -1 \times 10^{-6}$ measured with FTIR interferometer at different bunch current. 71

2.38 The 100% transmission lines for the ultra-low alpha experiments given by the ratio between two consecutive spectra for giving a measure of the SNR of the CSR source. 72

2.39 Comparison of rms bunch length between simulation and measurement for $\alpha = -2 \times 10^{-6}$. 74

2.40 Comparison of rms bunch length between simulation and measurement for $\alpha = -1 \times 10^{-6}$. 74

2.41 Comparison between measured and simulated spectra for $\alpha = -2 \times 10^{-6}$ at 7.5 μA. 76

2.42 Comparison between measured and simulated spectra for $\alpha = -1 \times 10^{-6}$ at 5.75 μA. 76

3.1 Schematic layout of a linac based THz source (FLUTE) [27]. 80

3.2 Layout of a compact linac-based THz source with three simulation regions. Simulation in each region is performed with the indicated numerical codes. Blue and green components are solenoids and quadrupole triplets, respectively. 81

3.3 Emittance compensation scheme [68]. (Top left) Initial transverse phase space at the cathode has small thermal emittance, (top middle) the phase space rotates anticlockwise due to space charge force at the region between the cathode and the solenoid, (top right) the solenoid provides the focussing field which rotates the phase space clockwise, (bottom left) after drifting from the solenoid the space charge force re-acts and forces the phase space rotating anticlockwise again, and (bottom middle) phase space ellipses are aligned around the invariant envelop at the end of the booster linac. 85

3.4 4-bend magnetic chicane for longitudinal bunch compression. 86

3.5 Schematic of bunch compression. (Left) the initial longitudinal phase space before acceleration by the RF cavity, (middle) the phase space after going through the RF cavity with off-crest phase introducing the energy chirp, (right) the phase space after the bunch compressor shown in under-compression and over-compression schemes. 87

3.6 Components in the injector simulation region. Solenoids are illustrated in blue. 92

3.7 Transverse phase space (top) and distribution (bottom) at the cathode. 93

3.8 Longitudinal phase space (left) and distribution (right) at the cathode. 94

3.9 Dependence of FEL resonance wavelength λ_r on relativistic factor γ at different undulator parameter K. 96

3.10 Normalised transverse emittance (left) and transverse beam size (right) along the injector region. 96

3.11 Horizontal (left) and vertical (right) phase space (top) and distribution (bottom) at the end of the booster linac. 97

3.12 Slice emittance of slices along the bunch (left) and slice ellipses in horizontal phase space (right) at the end of the booster linac. Each ellipse represents each slice in which black and grey ellipses are of the slices at the tail and head respectively. 97

3.13 Longitudinal phase space (left) and distribution (right) at the end of the booster linac. 98

3.14 Bunch compression region has X-band harmonic cavity, magnetic chicane, and three quadrupole triplets (displayed in green). 98

3.15 Optics functions along the bunch compression region including harmonic cavity and magnetic chicane. 100

3.16 rms bunch length in the bunch compression region. 101

3.17 Longitudinal distribution of bunch current at the photoinjector (left) and after compression (right). 101

3.18 Longitudinal phase space at the beginning of the bunch compression region (left), after passing the X-band cavity (middle) and at the end of the region (right). 102

3.19 Horizontal (top) and vertical (bottom) phase space before (left) and after (right) bunch compression. 102

3.20 Peak power radiated from the 500-pC bunch along the undulator length. 104

3.21 The initial bunch profile (blue) and the power profile at 4.7 m (orange). 104

3.22 FEL spectrum at the undulator length of 4.7 m. 104

3.23 Layout of the THz CSR source. The last chicane dipole is used as a radiator. Blue and green components are solenoids and quadrupole triplets, respectively. 106

3.24 Transverse phase space (top) and distribution (bottom) at the cathode. 107

3.25 Longitudinal phase space (left) and distribution (right) at the cathode. 107

3.26 Normalised transverse emittance (left) and transverse beam size (right) along the injector region. 109

3.27 Horizontal (left) and vertical (right) phase space (top) and distribution (bottom) at the end of the booster linac. 109

3.28 Slice emittance of slices along the bunch (left) and slice ellipses in horizontal phase space (right) at the end of the booster linac. Each ellipse represents a bunch slice and black and grey ellipses are of the slices at the tail and head of the bunch respectively. 110

3.29 Longitudinal phase space (left) and distribution (right) at the end of the booster linac. 110

3.30 Optics functions along the bunch compression region including harmonic cavity and magnetic chicane. 112

3.31 rms bunch length in the bunch compression region. 113

3.32 Longitudinal distribution of bunch current from the beam generation region (left) and from the compression region (right). 113

3.33 Longitudinal phase space at the beginning of the bunch compression region (left), after passing the X-band cavity (middle) and at the end of the region (right). 114

3.34 Horizontal (top) and vertical (bottom) phase space before (left) and after (right) bunch compression. 114

3.35 Spectrum of radiation emitted by the 500-pC bunch at the last chicane bending magnet with 1.85 m bending radius. 115

4.1 Examples of linear (left) and nonlinear (right) plasma wakefields [80]. 122

4.2	Accelerating field in a bubble region. The red arrows show the accelerating/decelerating forces and the green arrows show the direction of focussing forces inside the plasma bubble (adapted from [85]).	124
4.3	Self-injection in bubble regime [86].	125
4.4	2D electron density at 0.2 ps.	130
4.5	Transverse electric field at $z = 44\ \mu m$ corresponding to the position of the first bubble (left) and longitudinal electric field on axis of laser propagation (right) at 0.2 ps.	131
4.6	Longitudinal phase space of the self-injected electron bunch in the bubble at 3 ps.	131
4.7	2D electron density at 1 ps.	132
4.8	Longitudinal phase space of the self-injected electron bunch in the bubble at 1 ps.	133
4.9	Current distribution of the self-injected bunch at 1 ps laser propagation time.	133
4.10	Peak power emitted in a planar undulator by the 57-MeV beam from the LPWA.	135
4.11	Spectrum of total radiation (CSR and ISR) emitted by the self-injected bunch (solid) compared with the spectrum of ISR (dashed) assuming a 0.3-m dipole magnet with bending radius of 1.85 m.	136
4.12	An undulator canted the magnetic poles to introduce transverse gradient of magnetic field in the horizontal plane.	138
4.13	The peak power generated by propagating a 57-MeV electron beam with energy spread of 5.8% along TGU and normal planar undulator.	140
4.14	Spectrum of radiation generated by TGU and normal planar undulator at undulator length of 3.5 m.	141
4.15	The peak power along TGU and normal planar undulator emitted by a 57-MeV beam with energy spread of 1% simulated with Elegant.	141
4.16	Spectrum in TGU and normal planar undulator at undulator length of 2 m emitted by a 57-MeV beam with energy spread of 1% simulated with Elegant.	142
4.17	Peak power along the undulator radiated by the 750-MeV beam with energy spread of 1% in normal undulator and TGU.	144
4.18	Spectrum of SASE FEL generated by a 750-MeV beam with energy spread of 1% at 5 m in normal undulator and TGU.	144
4.19	Peak power of SASE FEL generated with TGU in the fundamental, third and fifth harmonics.	145
4.20	Layout of LPWA-based THz/IR source.	145

5.1 Top view of the ASL floor plan [94]. 149

5.2 Layout of compact RF driven THz sources: FEL (top) and CSR (bottom). Components in blue are solenoids and in green are the quadrupoles. 150

5.3 Layout of THz FEL driven by LPWA. 151

5.4 Side view (a) and top view (b) of the accelerator area of the ASL in FLUKA simulation. The concrete shielding is in purple. The accelerator elements and the beam dump are also shown. All dimensions are given in cm. 157

5.5 Front view (a) and side view (b) of the optimised design of the beam dump. All length is given in cm. 159

5.6 2D dose equivalent rate shown in three directions: side view (a), top view (b) and direction facing the beam (c) in the accelerator room of the ASL from FLUKA simulations. The minimum of colour scale shown is at 0.5 μSv/h. 161

5.7 Prompt dose equivalent rate averaged over the area (a) above concrete ceiling on top of the beam dump and (b) behind concrete wall in the beam direction. The area behind the concrete wall that the beam is directed towards includes 3 m distance from the beam axis in horizontal and vertical plane, and the area above the ceiling covers 3 m distance from the beam axis in the horizontal plane and 3 m on axis above the beam dump and shielding. 162

5.8 Residual dose equivalent rate inside the accelerator area in horizontal (a), vertical (b) and longitudinal (c) direction at time the beam terminated (0s), and after beam operations for one hour (1h) and eight hours (8h). Shaded green area shows the region occupied by the dump shielding. 163

A.1 Schematic of transfer matrices in a beamline for transferring a particle from the longitudinal position s_0 to s_n. 177

List of Tables

1.1	Examples of storage rings operating in low alpha mode for the production of THz radiation.	5
1.2	Examples of linac-based THz sources (TR: transition radiation, SR: synchrotron radiation, ER: edge radiation).	6
2.1	Main parameter used in the simulation of the Diamond storage ring.	38
2.2	SBD detectable frequency range.	49
2.3	Machine parameters for ultra-low alpha operating mode at Diamond storage ring.	56
2.4	FTIR signal-to-noise (SNR) ratios with sampling velocity 10 kHz.	73
3.1	Laser beam parameters at the cathode of the photoinjector for THz FEL design.	93
3.2	Parameters for locating a beam waist at 1.435 m from the cathode.	94
3.3	Optimised parameters of booster linac and solenoid 2 for THz FEL design.	95
3.4	Parameters of X-band harmonic cavity and 4-bend magnetic chicane for THz FEL design.	99
3.5	Initial and final beam parameters in the bunch compression region for THz FEL design.	100
3.6	Parameters for the THz FEL design in GENESIS simulations.	103
3.7	Laser beam parameters at the cathode of the photoinjector for THz CSR source design.	106
3.8	Parameters for locating a beam waist at 1.327 m from the cathode.	107
3.9	Optimised parameters of booster linac and solenoid 2 for THz CSR source design.	108
3.10	Parameters of X-band harmonic cavity and 4-bend magnetic chicane for THz CSR source design.	111
3.11	Initial and final beam parameters in the bunch compression region for THz CSR source design.	112
4.1	EPOCH parameters for generation lower and higher energy electron bunch from the LPWA in the bubble regime.	130
4.2	Parameters of self-injected bunch from *epoch2d* simulations.	134
4.3	Parameters for generation of SASE FEL using TGU to compensate energy spread effects.	140

4.4 Parameters for 750-MeV electron beam generated with Elegant and undulator parameters used in GENESIS simulation for this case. 143

5.1 Properties of materials used in beam dump design for the ASL. 160

Chapter 1

THz and Short Pulse Radiation

1.1 Introduction

Terahertz (THz) radiation sources are used in the investigation of a large variety of physical systems ranging from life sciences to material science, cultural heritage and medical applications [1]–[3]. The main characteristics of THz radiation that makes it a unique enabling tool for scientific research and applications are related to the fact that it is a non-ionising, non-invasive, and non-destructive radiation. THz radiation spans the frequency range between 0.3-10 THz and has many properties in common with infrared and microwave radiation. It can penetrate through non-conducting materials, although with lower penetration depth than microwave radiation, and it is non-ionising like both infrared and microwave radiation [4]. It can pass through many materials such as paper, plastic, fabric, wood and ceramics but it is absorbed by metal, water and many organic substances. More importantly, its wavelength is in the useful range for investigating vibration levels of biological molecules and the dynamics of chemical reactions. With these characteristics, applications of THz radiation have been studied and developed on very diverse fields such as:

- security,
- drug manufacturing,
- medical imaging, and
- communications

In security applications, THz radiation can be used for security scanning to uncover hidden weapons on a person, in particular at airports, thanks to penetration of THz radiation through clothes but not through metal, water and explosive materials. Unlike X-rays, THz radiation allows full-body scanning to be done without revealing body details, which protects personal privacy rights.

In drug manufacturing, THz spectroscopy is used to distinguish between different polymorph forms of drugs. Measurement of the drug tablet coating thickness can be done with Terahertz pulsed imaging (TPI). Tablet coatings are semi-transparent to THz frequencies so that THz pulses can penetrate through the different coating layers. At each interface, a portion of THz radiations is reflected back to the detector. By knowing the refractive index of coating materials, the coating thickness can be determined from the transit time of the pulse to each interface. Non-destructive quality assurance and control can be performed on pharmaceutical products by measuring the unique physical-chemical properties of a product by THz spectroscopy.

In medical imaging, coherent THz radiation pulses can be used to obtain phase and amplitude information from tissue and hence determine the absorption and refractive index of the medium. In cancer diagnosis, TPI can provide structural and functional information for investigating distinguishing type, lateral spread, and depth of skin tumours. THz imaging can detect tooth decay at an early stage in the enamel layers of teeth and monitor early erosion of the enamel at the surface of the tooth due to the characteristic of different types of tooth tissue. With the development of THz source and detector technology, live THz imaging may be possible and hence allow examination of epithelial cancer on patients without removing the tissue from the patients to diagnose.

In communication, THz wave can be used in high-altitude telecommunications between satellites or aircrafts and satellites above altitudes where the signal is absorbed by water vapour. THz frequency band have potential to alleviate capacity limitation of wireless systems and provide ultra-high-speed data communication within 10-m range [5].

New applications of THz radiation are continuously proposed and there is an ever increasing demand for high quality THz sources. With progress in the science of time resolution, the need for short pulses THz radiation has also increased, for example, to analyse properties of hybrid metal-organic perovskite solar cells 40 fs temporal resolution is required [6]. There is therefore an increasing need for high power short pulses THz radiation sources.

1.2 THz Radiation Sources

The frequency range of THz radiation is too high for such radiation to be generated by an electronic device, normally used in radio waves and microwaves. The conventional electronic devices are oscillating circuits based on high-speed transistors and semiconductor lasers, respectively. Such transistors have a bandwidth limited to about 0.3 THz in principle and 50 GHz in practice (600 μm to 2 mm wavelengths). The existing THz radiation sources include far infrared laser, semiconductor lasers, quantum cascade laser, photo-mixing source, resonant tunnelling diode (RTD), vacuum tube like gyrotrons, orotrons, and backward oscillators (BWO) [7]. While conventional laser systems, based on transition between atomic levels in a medium, and vacuum tubes can reach IR and THz frequency range, they lack properties such as tunability and the capability of generating high-power ultra-short pulses. Therefore, the provision of THz sources with adequate and flexible properties in terms of wavelength reach, tunability, high-peak power, broadband (i.e. ultra-short pulses) is still lacking. This situation is commonly dubbed as “THz-gap”.

The lack of conventional laser systems covering the THz spectrum has stimulated the development of alternative sources based on the use of electron beams to generate THz radiation exploiting different emission mechanisms like synchrotron radiation from dipoles and undulators, or coherent radiation from metallic interfaces (coherent transition radiation CTR [8]) and gratings (e.g. coherent Smith-Purcell radiation [9]). In particular, synchrotron light sources and free electron lasers (FELs) have the potential to produce THz radiation with higher power and shorter pulse length than any others. Therefore, in a number of existing synchrotrons and FEL facilities, new beamlines or experimental stations have been constructed, and more beam time dedicated to application of THz radiation has been reserved for an increasing number of experiments. The THz radiation properties in terms of power, pulse length and efficiency can be far superior to those of the commonly used THz sources.

1.2.1 Accelerator based THz Radiation sources

The THz radiation generated by accelerator-based sources has important specific characteristics such as the continuous covering of a wide spectral range (1 μm to 1 mm), high average power, high pulsed power, small beam divergence, and short pulses.

In storage rings, the THz radiation is generated in dedicated operating modes with special optics design to shorten the electron bunch length (low-alpha optics). The THz emission is based on the coherent synchrotron radiation emitted in dipole bending magnets. These operating modes are strongly susceptible to high-current driven beam instabilities and are not compatible with the standard user mode operation. For this reason they are normally offered to dedicated users in special beam time session where the storage ring is operated with much reduced stored current. Therefore, there is a strong incentive in tailoring and exploiting the source to its ultimate performance in the THz region. Chapter 2 of this thesis is dedicated to numerical and experimental studies focussed on the possibility

of further extending the capabilities of storage ring based THz radiation sources. A list of the main facilities offering THz radiation is reported in Table 1.1.

Table 1.1: Examples of storage rings operating in low alpha mode for the production of THz radiation.

Source	Beam energy	Bunch length (rms)	RF voltage	Horizontal emittance	Alpha	Average power
ANKA [10]–[12]	1.3 GeV	≥ 1 ps	0.6 MV	-	$> 1.4\times10^{-4}$	≤ 0.2 mW
SPEAR3 [13][14]	3 GeV	1 ps	≤ 3.2 MV	42 nm·rad	5.6×10^{-5}	0.3 mW
SLS [15]	2.4 GeV	6 ps	2.1 MV	13 nm·rad	5.3×10^{-5}	-
BESSYII [16]	1.7 GeV	3 ps	1.5 MV	30 nm·rad	3.5×10^{-5}	≥ 1 mW
SOLEIL [17]	2.75 GeV	4.8 ps	3.2 MV	8 nm·rad	1.7×10^{-5}	-
DLS [18]	3 GeV	3.5 ps	3.4 MV	4.5 nm·rad	-4.5×10^{-6}	~1 mW
ELETTRA* [19]	< 2 GeV	> 1 ps	-	5.7 nm·rad	2×10^{-4}	-

*ELETTRA generates THz radiation mainly by lowering beam energy

THz radiation can also be generated in linac-based radiation sources using the coherent synchrotron radiation (CSR) generated from bending magnets or THz FELs. A large number of THz facilities based on FEL oscillators are operating to-day around the world: a comprehensive list is reported in [20]. In this thesis, however, we focus our interest on the generation of high power (MW) and short pulses (< few ps), hence we considered mostly CSR radiators and THz FEL based on high-brightness linac and self-amplified spontaneous emission (SASE) from undulators. Alternatively, linac-based X-ray FELs are also used parasitically to drive THz sources. While storage rings provide radiation with high repetition rates, linacs offer electron beams with shorter pulses and smaller beam emittance which are essential features required by an increasing number of applications. Therefore, more compact THz sources driven by linacs are planned and constructed worldwide. A list of the main accelerator facilities that operated THz source from linacs is reported in Table 1.2 [21].

Table 1.2: Examples of linac-based THz sources (TR: transition radiation, SR: synchrotron radiation, ER: edge radiation).

Source	Type of radiation	Beam energy	Bunch charge	Pulse duration	Repetition rate	Frequency	Pulse energy
PAL [22]	TR	75 MeV	≤ 0.5 nC	≤ 150 fs	≤ 30 Hz	0.3-3 THz	> 10 μJ
SPARC [23]	TR	120 MeV	≤ 0.5 nC	≤ 500 fs	10 Hz	0.1-5 THz	> 1 μJ
FLASH [24]	TR/SR/ undulator	0.4-1.2 GeV	≤ 1 nC	≤ 6 ps	10 Hz	0.1-30 THz	> 0.1 mJ
FACET [25]	TR	23 GeV	3.2 nC	80 fs	10 Hz	0.5-5 THz	0.6 mJ
JLAB* [26]	SR/FEL	150 MeV	≤ 135 pC	0.1-2 ps	≤ 75 MHz	0.1-5 THz	> 1 μJ
FLUTE [27]	TR/SR/ ER	41 MeV	≤ 3 nC	< 1ps	10 Hz	0.1-25 THz	> 0.1 mJ

*JLAB operates FEL oscillators driven by superconducting linac.

It is also important to observe that the accelerator-based THz sources based on storage ring and large linacs, are necessarily located in large national laboratories. Chapter 3 and 4 of this thesis are focussed on the options of generating high-power short pulses THz radiation in compact facilities that can be hosted in small laboratories or universities. As such we will consider CSR and FEL sources from a low-energy high-brightness linac (Chapter 3) and we will investigate the issues associated with the use of Laser Plasma Wakefield Accelerators (LPWAs) to drive a THz source (Chapter 4). The main goal is to design facilities which are small, economic, highly performant and at the same time could be hosted in relatively small laboratory areas. An example discussed in this thesis is the possibility of installing such type of radiation source in the Accelerator Science Laboratory (ASL) in the University of Oxford (Chapter 5).

1.3 Synchrotron Radiation

In this chapter we review the basic properties of synchrotron radiation which will be used in the thesis. Synchrotron radiation is the electromagnetic radiation generated by a charged particle when travelling in an arc of a circumference under the influence of a static

magnetic field. It is generated copiously in electron storage rings where the electrons of energy E travel along arc of circles with constant radius ρ in dipole magnets with field B related by

$$B = \frac{E}{ec\rho} \tag{1.1}$$

where e is the elementary charge ($e > 0$) and c is the speed of light.

Synchrotrons radiation sources have been used since the 1950-ies after the first observation of synchrotron radiation at the 70-MeV electron synchrotron at General Electric in 1947 [28]. The first generation of synchrotron light sources used parasitically synchrotrons that were designed primarily for high-energy and nuclear physics experiments. The second generation light sources, in the 1980-ies, consisted of storage rings specifically built to produce synchrotron radiation, mostly based on dipole bending magnets. With the increased demand on higher photon brightness and flux, the third generation light sources were developed in the 1990-ies to generate low-emittance electron beams with dedicated optics. The storage ring lattice was also optimised to have long straight sections between curved parts of the storage rings for installing insertion devices (i.e. undulators and wigglers), which enhance brightness, photon flux and spectral range of the synchrotron radiation. Presently, the novel lattice designs are aimed at reducing the emittance of the electron beam to the so-called diffraction limit [29] also dubbed fourth-generation storage rings, which guarantees an even higher brightness and full transverse coherence of the radiation emitted.

In parallel to these developments, linac driven SASE FELs have become popular after the successful operation of the Linear Coherent Light Source (LCLS) at Stanford, the first X-ray FEL [30][31]. Also, these light sources are usually called fourth-generation light sources and produce radiation with higher coherence and shorter pulse length than the

previous generations. Further advances in the field consists in the numerical and experimental studies on the possibility of driving light source or FELs with advanced acceleration technology such as LPWAs. Radiation sources based on LPWAs have the potential to become the fifth generation light sources, which could revolutionise the field of photon science. However, as we will see in Chapter 5, they still have to overcome some fundamental limitation in the beam quality before being fully exploited, even for the generation of THz radiation.

The main properties of synchrotron radiation are:

- broad spectrum covering microwave up to X-ray,
- high flux,
- high brightness,
- high stability, and
- short pulse time structure.

These can be computed analytically from Maxwell's equations.

1.3.1 Synchrotron radiation from a dipole bending magnet

When relativistic charged particles pass through a dipole magnet, they are deflected by the magnetic forces perpendicular to their trajectory and they then travel in a circular path. Under the transverse acceleration, the relativistic particle beam with energy E in a path with bending radius ρ will emit synchrotron radiation with power given by

$$P = \frac{e^2 c}{6\pi\varepsilon_0} \frac{1}{(m_0 c^2)^4} \frac{E^4}{\rho^2} \tag{1.2}$$

here ε_0 is the permittivity of free space and m_0 is the rest mass of the particle. As can be seen in Equation (1.2), the emitted power is inversely proportional to the fourth power of

the rest mass. This shows that electron machines are more suitable as a radiation source compared to heavier charged particles.

In a centre of mass reference frame of the electrons, the radiation is emitted in all directions perpendicular to the accelerating direction as shown in Figure 1.1 (a). In the laboratory frame, due to the relativistic Lorenz transformations, the radiation is peaked in the direction of the velocity: the opening angle between the synchrotron radiation and the particle trajectory is inversely proportional to the relativistic factor γ given by

$$\theta \approx \frac{1}{\gamma}. \tag{1.3}$$

as shown in Figure 1.1 (b). This characteristic feature of the synchrotron radiation is extremely useful, allowing experiments on samples with extremely small surface area.

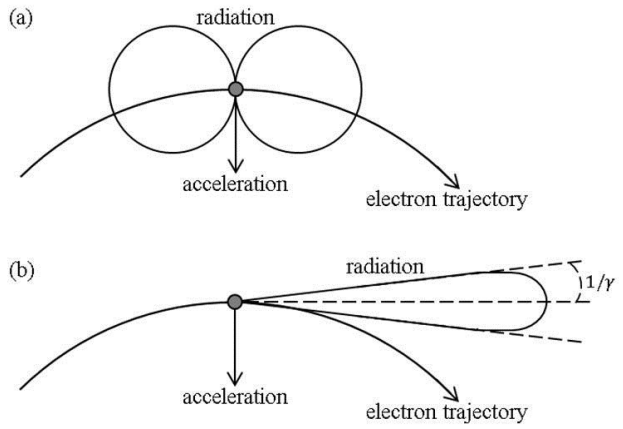


Figure 1.1: Synchrotron radiation in (a) centre of mass frame and (b) laboratory frame.

The radiated energy distribution in frequency and solid angle can be expressed as [32]

$$\frac{d^2I}{d\omega d\Omega} = \frac{e^2\omega^2\rho^2}{12\pi^3\varepsilon_0 c^3}\left(\frac{1+\gamma^2\theta^2}{\gamma^2}\right)\left[K_{\frac{2}{3}}^2(\xi) + \frac{\gamma^2\theta^2}{1+\gamma^2\theta^2}K_{\frac{1}{3}}^2(\xi)\right] \tag{1.4}$$

where θ is the vertical angle to the plane of the beam orbit, $K_n(\xi)$ is the modified Bessel function with the parameter

$$\xi = \frac{\omega}{2\omega_c}(1+\gamma^2\theta^2)^{3/2} \tag{1.5}$$

here $\omega_c = \frac{3c\gamma^3}{2\rho}$ is the critical frequency, beyond which the intensity of the emitted radiation decreasing rapidly.

Integrating Equation (1.4) over all angles gives the energy distribution in frequency

$$\frac{dI}{d\omega} = \frac{\sqrt{3}e^2\gamma}{4\pi\varepsilon_0 c}\frac{\omega}{\omega_c}\int_{\frac{\omega}{\omega_c}}^{\infty} K_{\frac{5}{3}}\left(\frac{\omega}{\omega_c}\right) d\left(\frac{\omega}{\omega_c}\right) \tag{1.6}$$

and it can be written as

$$\frac{dI}{d\omega} = \frac{2e^2}{9\varepsilon_0 c}\gamma S\left(\frac{\omega}{\omega_c}\right) \tag{1.7}$$

where the form of the universal function of synchrotron radiation is defined by

$$S\left(\frac{\omega}{\omega_c}\right) = \frac{9\sqrt{3}}{8\pi}\frac{\omega}{\omega_c}\int_{\frac{\omega}{\omega_c}}^{\infty} K_{\frac{5}{3}}\left(\frac{\omega}{\omega_c}\right) d\left(\frac{\omega}{\omega_c}\right) \tag{1.8}$$

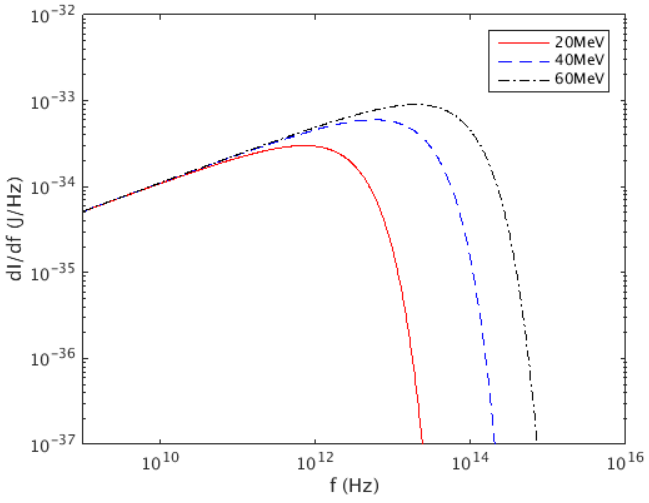


Figure 1.2: Frequency distribution of synchrotron radiation of an electron from a bending magnet with a bending radius $\rho = 1.72\ m$ at the energy of 20, 40 and 60 MeV.

The frequency distribution of the radiation emitted by a single electron is shown in Figure 1.2, for example, with an energy of 20, 40 and 60 MeV and bending radius of 1.72 m.

The spectral photon flux per second per unit angle per unit bandwidth can be expressed by

$$\frac{d\dot{N}_{ph}}{d\psi} = \frac{4}{9}\left(\frac{e^2}{4\pi\varepsilon_0\hbar c}\right)\frac{I_{beam}}{e}\frac{\Delta\omega}{\omega}S\left(\frac{\omega}{\omega_c}\right) \tag{1.9}$$

In a storage ring each electron will lose via synchrotron radiation the energy

$$U_0 = \frac{e^2\gamma^4}{3\varepsilon_0\rho}. \tag{1.10}$$

If we have a train of bunches, with average current I_b circulating in a storage ring, the total power lost via synchrotron radiation is given by

$$P = \frac{e\gamma^4}{3\varepsilon_0\rho}I_b. \tag{1.11}$$

1.3.2 Synchrotron radiation from insertion devices

In order to generate higher quality radiation, insertion devices (IDs) are installed in straight sections of modern synchrotron rings as main radiation generation components. The ID is a series of dipole bending magnets arranged with alternating polarity as shown in Figure 1.3.

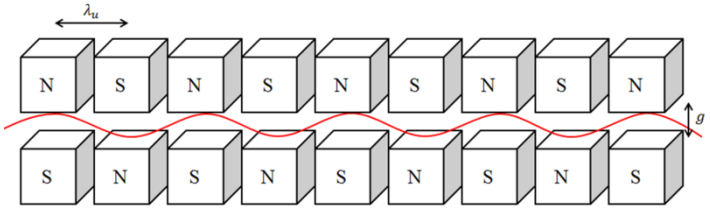


Figure 1.3: An example of insertion device with the gap width g and the period length λ_u.

The magnetic field of an ID depends on its gap between the magnet poles (g) and its period length (λ_u) and on the technology used. For example, the hybrid insertion device

made with Rare Earth Cobalt (REC) and steel has the peak magnetic field at the pole of the ID [33]

$$B_p = 3.33 \exp\left[-\frac{g}{\lambda_u}\left(5.47 - 1.8\frac{g}{\lambda_u}\right)\right]. \tag{1.12}$$

Assuming that the magnetic field has no horizontal component, using the coordinate system (x, y, s) where (s) is the position along the beam direction and (x, y) the coordinates in the transverse plane, the magnetic field components on vertical direction and beam direction are given by

$$\begin{aligned} B_y(y,s) &= B_0 \cosh(k_u y)\cos(k_u s) \\ B_s(y,s) &= B_0 \sinh(k_u y)\sin(k_u s\,) \end{aligned} \tag{1.13}$$

The peak of the magnetic field is related to the field at the magnet pole by

$$B_0 = \frac{B_p}{\cosh\left(\frac{\pi g}{\lambda_u}\right)} \tag{1.14}$$

where $k_u = \frac{2\pi}{\lambda_u}$. The equations of motion can be obtained from the Lorentz force $\vec{F} = e\vec{v} \times \vec{B}$ with the solutions

$$\begin{aligned} x(t) &= -\frac{K}{k_u \gamma}\cos\left(k_u \bar{\beta} c t\right) \\ s(t) &= \bar{\beta} c t + \frac{K^2}{8 k_u \gamma^2}\sin\left(2 k_u \bar{\beta} c t\right) \end{aligned} \tag{1.15}$$

with the average relative longitudinal velocity

$$\bar{\beta} = 1 - \frac{1}{2\gamma^2}\left(1 + \frac{\beta^2 K^2}{2}\right) \tag{1.16}$$

and strength parameter or undulator parameter

$$K = \frac{\lambda_u e B_0}{2\pi m_e c} \tag{1.17}$$

As seen from Equation (1.15), the ID forces the particle beam to travel in a horizontal sinusoidal path with the maximum horizontal deflection angle with respect to the s-axis as

$$\theta_{max} = |x'(s)|_{max} = \left|\frac{dx}{ds}\right|_{max} = \frac{K}{\gamma}. \tag{1.18}$$

The maximum deflection angle θ_{max} depends on the undulator parameter K. The IDs can be separated into two classes, undulators for $K < 1$ or wigglers for $K > 1$. In the undulator regime, $K \leq 1$, the angle θ_{max} is smaller than the radiation cone aperture: in this condition we can have a coherent interference from the radiation emitted by each pole of the undulator, resulting in a very sharp peak spectrum. In the wiggler regime, $K > 1$, the angle θ_{max} is larger than the opening angle of the radiation and the intensity adds up incoherently resulting in a broadband spectrum similar to the spectrum of bending magnet radiation.

In case of an undulator, the wavelength for which we have constructive interference between the poles, can be derived from the Lorentz transformation and the relativistic Doppler effect, and is given by

$$\lambda_r = \frac{\lambda_u}{2n\gamma^2}\left(1 + \frac{K^2}{2} + \gamma^2\theta^2\right) \tag{1.19}$$

where λ_u is an undulator period, n is the harmonic number and θ is the angle of observation with respect to s-axis in the laboratory frame. Equation (1.19) is also known as the resonance condition of the undulator radiation.

The energy radiated per unit frequency per unit solid angle from an undulator is expressed by

$$\frac{d^2I}{d\omega d\Omega} = \frac{e^2\gamma^2N^2}{4\pi\varepsilon_0 c} L\left(\frac{N\Delta\omega}{\omega_r}\right) F_N(K,\theta,\phi) \tag{1.20}$$

where N is the number of undulator periods, ω_r is the resonance frequency and $\Delta\omega = \omega - n\omega_r$. The line-shape for each harmonic is described by the function $L\left(\frac{N\Delta\omega}{\omega_r}\right)$ given by

$$L\left(\frac{N\Delta\omega}{\omega_r}\right) = \frac{\sin^2(N\pi\,\Delta\omega/\omega_r)}{N^2\sin^2(\pi\,\Delta\omega/\omega_r)} \tag{1.21}$$

and the angular harmonic distribution of the undulator radiation is represented by the function $F_N(K,\theta,\phi)$ defined as

$$F_N(K,\theta,\phi) = \frac{\omega^2}{4\pi^2\gamma^2}\left|\int_{-\lambda/2\beta c}^{\lambda/2\beta c}\left(\vec{n}\times\left(\vec{n}\times\vec{\beta}\right)\right)e^{i\omega(t-\vec{n}\cdot\vec{r}/c)}dt\right|^2. \tag{1.22}$$

Examples of both functions for a planar undulator are plotted in Figure 1.4.

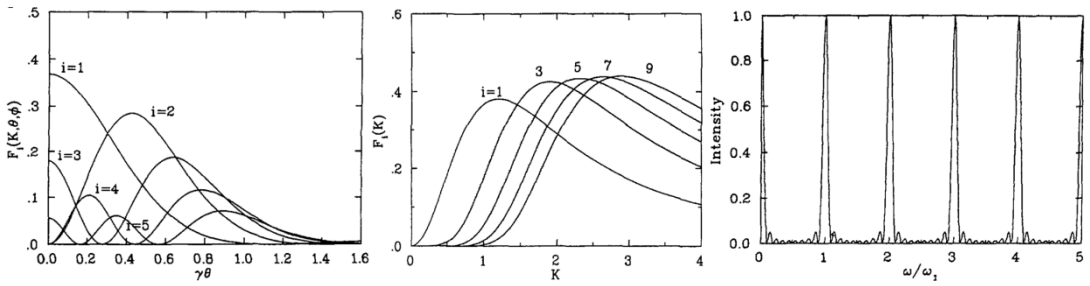


Figure 1.4: Distribution of radiation in the harmonics as a function of the horizontal angle (left), of the undulator parameter (middle) and line-shape spectrum of the planar undulator radiation (right) [34].

1.4 Coherent Synchrotron Radiation

In general, the power of the synchrotron radiation at wavelengths shorter than the bunch length depends linearly on the number of electrons in a bunch. In this case, each electron emits independently from each other and the radiation is the incoherent superposition of the synchrotron radiation emitted by each electron. This is known as incoherent synchrotron radiation (ISR). However, if the radiation wavelength is longer than

the bunch length, the electrons in the bunch will radiate coherently at that wavelength and the corresponding power is proportional to square of the number of the electrons in the bunch. This is known as coherent synchrotron radiation (CSR) and can be significantly more powerful than the ISR. The total power emitted at wavelength (λ) by a bunch with N_e electrons is given by

$$P(\lambda) = P_e(\lambda)[N_e + N_e(N_e - 1)f(\lambda)] \tag{1.23}$$

here $P_e(\lambda)$ is the power radiated by a single electron and the form factor $f(\lambda)$ is calculated from the Fourier transform of the longitudinal bunch distribution $\rho(z)$ as

$$f(\lambda) = \left| \int_{-\infty}^{\infty} \rho(z) e^{-i\frac{2\pi z}{\lambda}} dz \right|^2. \tag{1.24}$$

In the wavelength range where the form factor is close to 1, we have CSR and the corresponding power enhancement, while elsewhere the emission has the standard characteristics of ISR. CSR can be generated by two main methods: (1) squeezing the bunch longitudinally so that the bunch length is shorter than the expected wavelength, (2) modulating the longitudinal density of the bunch so that the electrons are separated into micro-bunches.

The spectrum of the CSR is extended to higher frequency when the bunch is shorter. The intensity of the radiation from a Gaussian bunch of bunch length σ_z at the frequency below [35]

$$f_b = \frac{c\sqrt{\ln N_e}}{2\pi\sigma_z} \tag{1.25}$$

is enhanced due to CSR as shown in Figure 1.5. Note that, in the real machines, the dimension of the beam pipe restricts the longest observable wavelength and therefore frequencies below the cut-off frequency of the beam pipe are strongly suppressed as shown in the grey area in Figure 1.5.

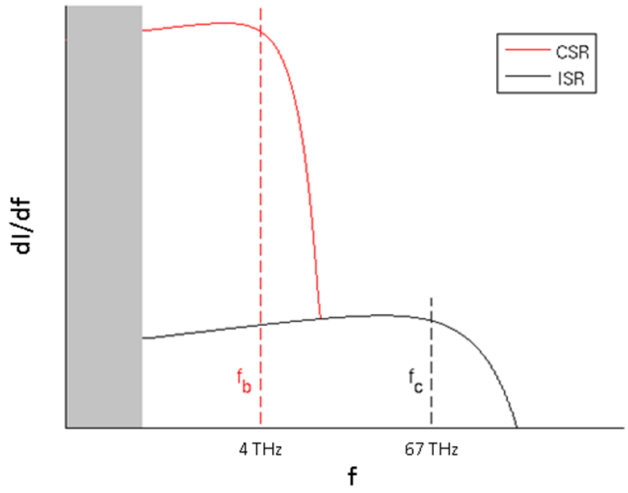


Figure 1.5: Frequency distribution of ISR (black solid line) and CSR (red solid line) emitted from a 500-pC bunch with rms bunch length of 200 fs (60 μm) at 60 MeV in a bending magnet of bending radius 1.72 m. The black dashed line and the red dashed line show the critical frequency and the frequency associated to the inverse bunch length Equation (1.25), respectively.

1.5 Free Electron Laser

Free electron lasers (FELs) are sources of high power tuneable radiation using a beam of electrons generated by an accelerator as gain medium. As the electrons travel down the undulator they emit synchrotron radiation along the undulator axis. Such radiation interacts again with the electrons producing an energy exchange between them. The electrons travel with a velocity smaller than the phase velocity of the radiation, hence they are continuously overtaken by the radiation wavefronts. However, a substantial energy exchange can still be achieved when the phase shift of the radiation field over the electron is equal to 2π as the electron has travelled undulator period. This resonance condition is shown in Figure 1.6.

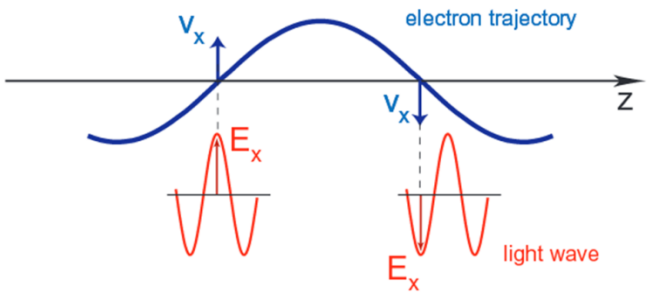


Figure 1.6: Phase condition to sustain energy transfer between electric field of synchrotron radiation and an electron [36].

As the electrons travel down the undulator, the energy modulation produced along the electron bunch is converted in density modulation which occurs at the resonant wavelength (1.19). This is the so-called FEL micro-bunching. The generation of a micro-bunching structure in the longitudinal profile of the beam enhances further the emission of radiation and instability develops, where the radiation grows exponentially as the micro-bunching develops. The electrons in a micro-bunch whose length is comparable with the radiation wavelength, emit coherently at the radiation wavelength in the forward direction, until saturation is reached. In this way the spontaneous radiation emitted in the undulator or an external seed at the resonance wavelength λ_r under the resonance condition (from Equation (1.19) with $\theta = 0$)

$$\lambda_r = \frac{\lambda_u}{2\gamma^2}\left(1 + \frac{K^2}{2}\right) \tag{1.26}$$

is continuously amplified to saturation.

The resonance wavelength is tuneable by either changing the beam energy or the undulator gap, i.e. changing the undulator parameter K. This tunability of the radiation wavelength is one of the greatest characteristic features of the FEL.

The FEL can operate according to two basic processes: FEL oscillator and FEL amplifier. The former uses an idea of optical resonator by locating two mirrors on both ends of the undulator. The radiation is reflected many times between the mirrors and gains more energy from the electron beam each time it passes through the undulator. Since currently-available mirrors cannot reflect wavelengths shorter than about 100 nm, this process is suitable for producing FEL in mm-wave range to UV range. On the other hand, to produce the shorter wavelength FEL down to the X-ray range, the FEL amplifier process is applied by using a long undulator with many periods instead of reflecting mirrors. This type of the FEL amplifier is referred to as self-amplification spontaneous emission (SASE).

1.5.1 Self-amplification spontaneous emission

The amplification of the radiation can be achieved within a single pass of the electron beam along the undulator. The process can be separated into three phases: start-up, exponential gain and saturation. Initially, the longitudinal distribution of the electron bunch is typically random and the current is referred to as shot-noise. In the first section of the undulator, spontaneous radiation emitted from the bunch with the shot-noise starts to interact on the electrons leading to energy transfer between electrons and radiation fields, and then micro-bunching is initiated. As the bunch traveling further along the undulator, the micro-bunching continues and the electrons in each micro-bunch radiate coherently. The radiation fields gain more and more energy, and hence the power of the radiation increases exponentially with the distance the beam travels along the undulator until the power reaches saturation where full micro-bunching is achieved.

1.5.2 The FEL parameterisation

In the simplest case, the SASE FEL process can be modelled by one-dimensional (1D) model [37] assuming that the beam has a uniform transverse spatial distribution with zero emittance and zero energy spread. The characteristics of the FEL radiation are

determined by several parameters. To begin with, the effective input shot-noise power of the electron beam of the beam energy E_0 with resonant wavelength λ_r is given by [38]

$$P_0 \approx \rho^2 c \frac{E_0}{\lambda_r} \tag{1.27}$$

here ρ is the Pierce parameter defined by

$$\rho = \frac{1}{2\gamma}\left(\frac{I}{I_A}\frac{\lambda_u^2 a_u^2 [JJ]^2}{4\pi^2 \sigma_x^2}\right)^{\frac{1}{3}} \tag{1.28}$$

where I is the beam current, $I_A \approx 17\,kA$ is the Alven current, a_u is the normalised undulator parameter in which $a_u = K_u/\sqrt{2}$ for a planar undulator and $a_u = K_u$ for a helical undulator, σ_x is the transverse beam size and $[JJ]$ is the Bessel function factor defined as

$$[JJ] = \left[J_0\left(\frac{\xi}{2}\right) - J_1\left(\frac{\xi}{2}\right)\right], \quad \xi = \frac{a_u^2}{1 + a_u^2}. \tag{1.29}$$

In the exponential gain phase, the radiation power with z grows as

$$P(z) = \frac{1}{9} P_0 e^{z/L_g} \tag{1.30}$$

where z is the longitudinal distance in the undulator, and L_g is the power gain length (i.e. the distance in the undulator where the radiation power rises e times of the initial power) given by

$$L_g = \frac{\lambda_u}{4\pi\sqrt{3}\rho}. \tag{1.31}$$

Typically, the saturation can be reached at the saturation length $L_{sat} \approx 20 L_g$. For the electron beam with power of $P_{beam} = E_0 I$, the saturation power is given by

$$P_{sat} \approx \rho P_{beam}. \tag{1.32}$$

Both Equation (1.31) and (1.32) indicate that the efficiency of the FEL process is determined by the Pierce parameter; large Pierce parameter correspond to short gain length and high saturation power. As a consequence the FEL needs an electron beam with high current, small beam size (low emittance) and low energy to reach saturation within a reasonable length of the undulator train.

It is important to notice that the radiation emitted by SASE usually consists of many temporal spikes along the bunch train and therefore has rather poor time coherence. The limit on the temporal coherence is set by the so-called cooperation length, which indicates the length along the bunch in which the electrons interact via the synchrotron radiation emitted in the undulator. The cooperation length is formally defined as the slippage length over one gain length as

$$L_{coop} = \frac{\lambda_r}{\lambda_u} L_g = \frac{\lambda_r}{4\pi\sqrt{3}\rho}. \tag{1.33}$$

The FEL pulse developing in the SASE mode is made of spikes with length given by Equation (1.33). In particular, if the bunch length is just matched to the length Equation (1.33) only one FEL spike is generated achieving full longitudinal coherence, otherwise the FEL pulse will contain a number of spikes given approximately by L_{bunch}/L_{coop}. For electron bunches shorter than Equation (1.33) the FEL process is hindered by slippage effects, the gain process is stopped because the bunch is too short and the radiation has slipped forward, and the FEL reaches an early saturation.

Equation (1.31) for the gain length is based in the 1D model for the FEL interaction, which considers only the evolution of the longitudinal phase space of the FEL in the ponderomotive potential and neglects any transverse effect. In more realistic cases, the full three-dimensional (3D) effect should be considered including the effects of the beam

emittance, energy spread and the diffraction of the radiation fields. A 3D model which takes into account these effects is needed for a more precise FEL study. A universal scaling function is proposed by M. Xie [38] to estimate 3D parameters from 1D parameters. The 3D Pierce parameter is given by

$$\rho_{3D} = \frac{\rho}{1+\Lambda} \tag{1.34}$$

and the gain length is then modified as

$$L_{g,3D} = L_g(1+\Lambda) \tag{1.35}$$

where Λ is the scaling function calculated from 19 fitting parameters associated with the electron's longitudinal velocity spread caused by emittance and by energy spread, and diffraction effect. The value of Λ is typically below 2. The 3D Pierce parameter is smaller and the gain length is larger than those in the 1D model. In these conditions the radiation field should have longer saturation length when considering effects of emittance, energy spread and diffraction, which degrade the electron beam quality. The analysis of the 3D dynamics requires more realistic simulations than just analytical calculations and hence numerical codes such as GENESIS [39] are normally used for the FEL study.

For producing high-power and high-coherence FELs, there are three requirements on the electron beam peak current (I_0), emittance (ε) and energy spread (σ_δ). For instance, the requirements for UV and X-ray FELs are typically as follows

$$I_0 \geq 1\ kA, \qquad \varepsilon \leq \frac{\lambda_r}{4\pi}, \qquad \sigma_\delta \leq \frac{\rho}{2}. \tag{1.36}$$

The goal of the accelerator design is to produce an electron beam with the adequate quality to drive the FEL as expressed by the conditions of Equation (1.36). Unfortunately, achieving high peak-current bunches in a linac is generally in contrast with achieving a smaller emittance and small energy spread: for example, the electron bunch needs to be

compress longitudinally to increase peak current but the bunch compression causes an emittance growth and an increase of higher energy spread due to CSR and other collective effects. Therefore, the optimisation of the FEL designs is coupled to the beam dynamics in the linac and ultimately demands for complex start-to-end simulations.

1.6 Compact THz radiation sources

Nowadays, more and more scientific experiments need high quality THz radiation. Although THz radiation is available in low-alpha operating modes in many storage rings such as ANKA [10]–[12], SPEAR3 [13][14] , SLS [15], BESSY [16], SOLEIL [17], Diamond [18][40] and ELETTRA [19] such operating modes are normally incompatible with the standard operation of the machine.

As we can infer from Equation (1.26), the operating of a THz FEL does not require exceedingly high electron beam energy therefore linac based THz sources could be installed in small scale laboratories using CSR radiation from bending magnets or THz FEL from undulators. A good example of such a compact THz source is the project FLUTE [27] which is a linac-based THz source established as a test facility to develop compact THz sources and also provide THz radiation for scientific experiments. FLUTE aims to generate short pulse coherent THz radiation with three main mechanisms: synchrotron radiation (SR), edge radiation (ER), and transition radiation (TR).

In this thesis, compact linac-based THz sources are designed to generate FEL with an undulator and CSR with a bending magnet. The corresponding layout are possible options to be considered for the project of the Accelerator Science Laboratory (ASL) that plans to install a compact THz radiation source based on an electron linac in the basement area of Denys Wilkinson Building in the University of Oxford.

1.7 Thesis Layout

This thesis presents the study carried out to analyse the generation of short pulse THz radiation from storage rings and from smaller-scale accelerators such as low-energy linacs, with a cursory analysis of the options for a LPWA. The aim is that of designing a compact accelerator-based THz source that fits in a small laboratory and offers opportunities for advanced accelerator research and to foster accelerator science education in the universities.

The structure of this thesis as follows. Chapter 2 discusses the short pulse THz radiation generated with the ultra-low alpha operating mode at Diamond Light Source presenting both experiment and simulation results. Chapter 3 presents the design of compact THz radiation source based on an RF linac. Chapter 4 discusses the investigation of a THz radiation source driven by a LPWA. The layout of a compact THz radiation source and the study of the radiation shielding for an accelerator based THz/IR radiation source in the ASL are presented in Chapter 5. Finally, conclusions and future work are discussed in Chapter 6.

Chapter 2

Generation of Short Pulse THz Radiation with Storage Rings

THz radiation can be generated in storage rings taking advantage of the broadband spectrum radiation emitted by the electrons in a dipole, as shown in Figure 1.2. The spectrum of the radiation emitted by each electron reported in Equation (1.7) is approximated to the low frequency expression for $\omega \ll \omega_c$

$$\frac{dI}{d\omega} = \frac{2e^2\gamma}{9\varepsilon_0 c} S\left(\frac{\omega}{\omega_c}\right) \approx \frac{2e^2\gamma}{9\varepsilon_0 c}\left(1.3333\left(\frac{\omega}{\omega_c}\right)^{1/3}\right) \tag{2.1}$$

The emission from the electrons in the bunch becomes coherent for the wavelength longer than the bunch length and is therefore significantly enhanced. The spectrum is reported in Equation (1.23) in Chapter 1 and is given by

$$P(\omega) = P_e(\omega)[N_e + N_e(N_e - 1)f(\omega)] \tag{2.2}$$

where the form factor $f(\omega)$ is the Fourier transform of the longitudinal bunch profile and gives the spectrum of temporal modulation due to the CSR. The effect of the vacuum chamber cut-off is explained in Chapter 1.

From Equation (2.2), it is clear that if we want to increase the radiation emitted in the THz, it is convenient to operate with short bunches in the storage ring by reducing the equilibrium bunch length, and extending the form factor to higher frequencies. These operating modes require special optics, called low alpha modes where alpha (or α_c) is the momentum compaction factor of the ring. As we will see, the natural or zero-current bunch

length is proportional to square root of the momentum compaction factor, therefore reducing alpha decreases the equilibrium bunch length of the circulating beam and CSR in the THz wavelengths can be generated. Low alpha optics are generated by a suitable matching of the optics function of the magnetic lattice to reach the quasi-isochronous condition, making all electrons travel through almost the same distance over the ring, regardless of their energy. A complication related to the operation of such optics is the fact that they are more susceptible to collective instabilities, and therefore the maximum current that can be stored is limited. The analysis of the beam dynamics is significantly more complicated when collective effects are included and it has to be ultimately demanded to particle tracking supported by an adequate modelisation of the machine impedance.

In this chapter, we discuss the relation between bunch length and alpha, the basic optics design for low alpha lattices, and how to increase the spectral range by reducing the bunch length to its ultimate limit for storage rings. The Diamond storage ring has operated in low alpha mode since 2009 [41] to deliver short X-ray pulse radiation and THz/far IR CSR for users. More recently, a new operating mode was tested at Diamond with the aim of pushing alpha to the lowest possible value that can be reached while maintaining good machine operating conditions (e.g. injection efficiency, beam lifetime, beam stability, etc.). Such machine configuration has been defined as “Ultra-low alpha mode” and has been trialled for the first time at Diamond in December 2015, with the aim of shortening the bunch length to expand the frequency range to higher THz frequencies. Tests with THz users have been also carried out to verify that the predicted extension of the THz frequency range is produced with the stability and the signal to noise ratio that enable the users to effectively exploit such source. Measurement techniques used to characterise THz CSR spectrum and electron bunch length are reviewed, with particular emphasis on the instrumentation available at the Diamond Light Source. A large part of the work has been

dedicated to single bunch dynamics simulations with various collective effects in order to compare the measurements in the ultra-low alpha mode at Diamond storage rings with the simulations. These results are discussed in detail.

2.1 Background of low alpha operating mode

We introduce here the relation between the bunch length and the momentum compaction factor, low alpha lattices, collective effects and impedance sources are discussed in the following paragraphs. The basic concepts of the beam dynamics in accelerators are reported in Appendix A.

2.1.1 Relation between natural bunch length and alpha in storage rings

In electron storage rings, the equilibrium values for the relative energy spread and the bunch length are the result of the competition between the process of radiation damping and radiation excitation due to the discretised nature of the emission of synchrotron radiation [42].

The natural rms bunch length defined as the bunch length at zero bunch-current is given by

$$\sigma_0 = \frac{c\alpha_c}{2\pi f_s}\sigma_E \tag{2.3}$$

where α_c is the momentum compaction factor, f_s is the synchrotron frequency and σ_E is the rms relative energy spread. The spread of momentum makes electrons in the same bunch circulate around the ring with different revolution time. The RF field in the cavity is sampled differently by electrons arriving at different time generating a finite electron bunch length dependent on the momentum spread. The synchrotron frequency can be calculated from the ring parameters as

$$f_s = f_{rev}\sqrt{\frac{|\alpha_c| h e V_{RF}\cos\phi_s}{2\pi E_0}} \tag{2.4}$$

here f_{rev} is the revolution frequency, h is the harmonic number, V_{RF} is the cavity peak voltage and E_0 is the nominal energy of the beam, ϕ_s is the synchronous phase. As a result, the natural bunch length can be written as

$$\sigma_0 = \frac{c\sigma_E}{f_{rev}}\sqrt{\frac{|\alpha_c| E_0}{2\pi h e V_{RF}\cos\phi_s}} \tag{2.5}$$

which shows clearly the bunch length dependence on the machine parameters. We can manipulate the bunch length by changing the RF voltage or the momentum compaction factor. The relative energy spread depends on the beam energy and the bending radius of dipoles and cannot be changed. If we want to reduce the bunch length we can increase the RF voltage although we are limited by the total voltage available. The simplest way of reducing the bunch length is therefore changing the momentum compaction factor.

The momentum compaction factor is defined as the relative change in the reference orbit length ΔL as a function of the relative energy deviation of the electron δ

$$\alpha_c = \frac{\Delta L/L_0}{\delta} \tag{2.6}$$

where L_0 is the path length of the reference orbit, i.e. the storage ring circumference. In order to modify the bunch length we must modify the storage ring lattice into the so-called low alpha lattice. This is achieved by setting the quadrupoles in the lattice to control the value of alpha as described in the following paragraph.

2.1.2 Low alpha lattice

The momentum compaction factor in Equation (2.6) can be expanded as a power series of the relative energy deviation as in

$$\alpha_c = \alpha_1 + \alpha_2\delta + O(\delta^2) \tag{2.7}$$

The first and second-order momentum compaction factors are expressed by

$$\alpha_1 = \frac{1}{L_0}\int_0^{L_0} \frac{\eta_1(s)}{\rho} ds \tag{2.8}$$

$$\alpha_2 = \frac{1}{L_0}\int \left[\frac{\eta_1'(s)^2}{2} + \frac{\eta_2(s)}{\rho}\right] ds \tag{2.9}$$

where η_1 and η_2 are the first and second-order dispersion expanded in terms of momentum deviation (δ) and η_1' is the derivative of the first-order dispersion with respect to the longitudinal coordinate.

In the first-order limit, the alpha depends on the value of the dispersion in the dipoles only, since $1/\rho$ i.e. the inverse of the bending radius is non zero. Hence, alpha can be reduced by minimising the integrated dispersion inside the dipoles by a suitable optimisation of the quadrupole strength. A first indication on the dependence of the momentum compaction factor on the machine parameters can be obtained by using a FODO cell in the so-called smooth approximation, whereby the first-order alpha is inversely proportional to the horizontal tune as $\alpha_1 \approx \frac{1}{\nu_x^2}$ and it can be manipulated by the change in a quadrupole field strength (Δk) [43] according to

$$\Delta\alpha_1 = -\frac{\Delta k}{L_0}\left(\eta_x^2 - \eta_y^2\right) \tag{2.10}$$

where η_x and η_y are the horizontal and vertical dispersion at the location of the quadrupole. So the first-order alpha can be reduced effectively by quadrupoles at the location of large dispersion.

In case of the second-order alpha shown in Equation (2.9), the integrated sextupole strength (S) affects the momentum compaction factor [44] as

$$\Delta\alpha_2 = -\frac{SL_0}{3}\left(\eta_x^3 - 3\eta_x\eta_y^2\right). \tag{2.11}$$

This relation shows that the second-order alpha can be controlled by sextupoles in the regions of high horizontal dispersion.

The precise manipulation of the momentum compaction factor and the matching of the corresponding optics function in the low alpha lattice is achieved using the matching codes like MAD-X [45] or Elegant [46], that allows setting the quadrupole families to reduce alpha and compute the lattice parameters. Several design strategies produce low alpha lattices based on the control of the dispersion function at the dipole as indicated by Equation (2.8). In one class of solution reduce α_c by reducing the dispersion function as much as possible at the dipoles. The second class of solutions reduces α_c by exploiting the change of sign of dispersion in the dipole. These approaches are schematically shown in Figure 2.1 where the dispersion for standard user mode and low alpha mode, for instance, with high and low emittance solutions are shown [47].

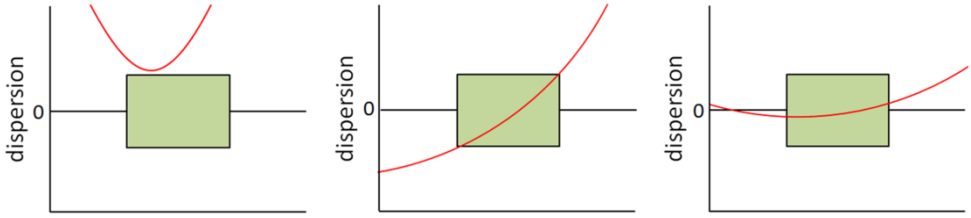


Figure 2.1: Dispersion function in a dipole for standard user mode (left), low alpha with high emittance (middle), and low alpha with low emittance (right) lattices.

2.1.3 Collective effects in storage rings

The momentum compaction factor can be positive or negative and, typically, storage rings operate with positive alpha in their normal users' operating mode. The two regimes have significant different behaviour when the effects of wakefields are considered

in the beam dynamics. In this paragraph we introduce the beam dynamics in presence of wakefields.

In electron storage rings, collective effects may induce beam instabilities limiting the performance of the storage rings, especially in dedicated operating mode like low-alpha. It is therefore important to understand their effect on the beam dynamics. In this paragraph we review the basic description of the wakefields that were used to quantify their effect in the Diamond storage ring.

Collective effects are generated by electromagnetic fields induced from the interaction between the charge particle beam and vacuum chambers around the ring, usually called wakefields. Since electrons circulate at almost the light velocity, the wakefields are left behind the traveling particle and can influence the trailing particles in the same bunch and on following bunches.

The wakefields introduce momentum change or transverse kick on trailing charged particles. The momentum kick due to the wakefields per unit charge is defined as the wake potential. The wakefields are also represented by wake functions which are defined as the wake potentials per unit charge. The wake function depends on the specific structures of the beam pipe along the accelerator and they are defined as function of the position of the trailing particle with respect to the leading particle. According to causality, the wake function is zero for positive z (head of the bunch), meaning that the wakefields can act only on the back of the particle. An example of wakefield is shown in Figure 2.2.

In the study of beam instabilities in storage rings, it is usually more convenient to operate in the frequency domain by using the concept of impedance. The wake function is defined in the spatial domain and can be transformed to the impedance in frequency domain by taking a Fourier transformation. The longitudinal impedance is given by

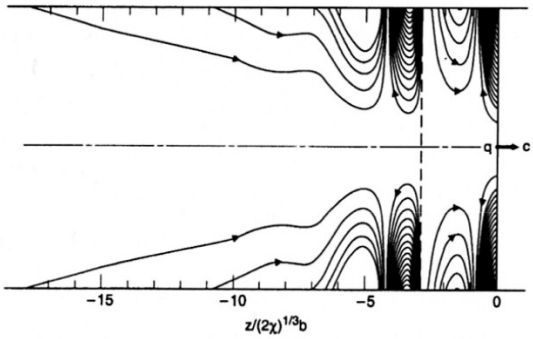


Figure 2.2: Wakefield represented by electric field lines produced by the charged particle q traveling at the speed of light [48].

$$Z_{\parallel}(\omega) = \int_{-\infty}^{+\infty} W_{\parallel}(z) e^{-i\omega z/c} \frac{dz}{c} \tag{2.12}$$

and the transverse impedance per unit length is

$$Z_{\perp} = i \int_{-\infty}^{+\infty} W_{\perp}(z) e^{-i\omega z/c} \frac{dz}{c} \tag{2.13}$$

where $W_{\parallel}$ and $W_{\perp}$ is the longitudinal and transverse wake functions respectively and z is the longitudinal coordinate with respect to the leading particle.

As a result of the interaction with the wakefields, the electron lose energy, as indicated by the longitudinal loss factor

$$\kappa_{\parallel} = \frac{1}{2\pi} \int_{-\infty}^{+\infty} Z_{\parallel}(\omega) |\Lambda(\omega)|^2 d\omega \tag{2.14}$$

where $\Lambda(\omega)$ is the Fourier transform of the normalised longitudinal bunch profile $\lambda(t)$ with the condition $\int \lambda(t) dt = 1$, or get kicked transversely, as indicated by the transverse kick factor

$$\kappa_{\perp} = \frac{1}{2\pi} \int_{-\infty}^{+\infty} Z_{\perp}(\omega) |\Lambda(\omega)|^2 d\omega. \tag{2.15}$$

The model of impedance can be built from a variety of impedance sources, for example purely inductive and resistive impedance, resistive wall and broad-band resonator, or it can be extracted from the simulation of wakefields generated by the vacuum pipe elements by fitting the impedance spectrum with a suitable number of resonators. Alternatively the parameters of the resonators can be extracted directly from the measurements of the bunch length and energy spread as a function of the bunch current.

2.1.4 Relevant longitudinal impedance sources

We discuss here the main sources of impedance in storage rings light sources. Their impact in the dynamics of low alpha lattice will be analysed in the following.

Resistive wall

The wakefields generated by resistivity of a vacuum chamber or beam pipe are known as resistive-wall (RW) wakefield. The model of the longitudinal RW impedance is formulated as [49][50]

$$Z_{\parallel}^{RW}(\omega) = \frac{L(1+i\omega)}{4\pi cb} Z_0 \omega \delta_s(\omega) G_0 \tag{2.16}$$

here L is the length of the vacuum chamber, b is the half chamber aperture, Z_0 is the impedance of free space, the skin depth

$$\delta_s(\omega) = \sqrt{\frac{2c}{\mu_r \sigma_c Z_0 |\omega|}}, \tag{2.17}$$

where μ_r and σ_c are the relative permeability and conductivity of the chamber material and the form factor

$$G_0(u_0) = \frac{\sinh u_0}{2\pi} \int_0^{2\pi} \frac{Q_0^2(v)}{\sqrt{\sinh^2 u_0 + \sin^2 v}} dv, \tag{2.18}$$

where Q_0 and u_0 are defined as

$$Q_0(v) = 1 + 2\sum_{m=1}^{\infty}(-1)^m \frac{\cos 2mv}{\cosh 2mu_0}, \tag{2.19}$$

$$u_0 = \cosh^{-1}\frac{1}{\sqrt{1-\left(\frac{b}{a}\right)^2}}. \tag{2.20}$$

The longitudinal loss factor per unit length for a Gaussian bunch is

$$\frac{\kappa_\parallel}{L} = \frac{\Gamma\left(\frac{3}{4}\right)c}{4\pi^2 b\sigma_z^{3/2}}\left(\frac{Z_0}{2\sigma_c}\right)^{1/2} \tag{2.21}$$

which has dependence on the inverse aperture $(1/b)$ and strongly on the bunch length $(\sigma_z^{-3/2})$ [51].

Broad-band resonator

The impedance of the vacuum chamber can also be modelled as a broad-band resonator (BBR), named also BBR impedance. The longitudinal BBR impedance is defined as

$$Z_\parallel^{BBR}(\omega) = \frac{R_s}{1 + iQ\left(\frac{\omega}{\omega_r} - \frac{\omega_r}{\omega}\right)} \tag{2.22}$$

where R_s is the longitudinal shunt impedance, $\omega_r = 2\pi f_r$ is the resonance frequency and Q is the quality factor of the equivalent resonator. The longitudinal BBR wake function is calculated by [48]

$$W_\parallel^{BBR}(z) = 2\alpha R_s e^{\frac{\alpha z}{c}}\left(\cos\frac{\bar{\omega}z}{c} + \frac{\alpha}{\bar{\omega}}\sin\frac{\bar{\omega}z}{c}\right) \tag{2.23}$$

where $\alpha = \frac{\omega_r}{2Q}$ and $\bar{\omega} = \sqrt{\omega_r^2 - \alpha^2}$.

CSR and shielding effect

The electromagnetic fields of the CSR generated from the storage ring also disturb the particle beam and induce the beam instability. The longitudinal CSR wake function in free space can be given by

$$W_{fs}^{CSR}(z) = -\frac{ReN_e}{\varepsilon_0}\int_{-\infty}^{\infty}\frac{d\lambda(z-z')}{dz}\frac{1}{(3R^2z')^{1/3}}\,dz' \tag{2.24}$$

where R is the bending radius, N_e is the number of electrons in a bunch and $\lambda(z)$ is the normalised longitudinal bunch profile with the condition $\int \lambda(z)dz = 1$. In the dipoles, the CSR wakefield is shielded by the vacuum chamber. Modelling the chamber as two infinite parallel plates separated by a gap $2h$, allows the longitudinal wake function with the shielding effect to be written as

$$W_{sh}^{CSR}(z) = \frac{ReN_e}{\varepsilon_0}\int_{-\infty}^{\infty}\frac{\lambda(z-z')}{4h^2}G_2\left[\frac{1}{2h}\left(\frac{R}{h}\right)^{1/2}z'\right]dz' \tag{2.25}$$

where G_2 is the scaled function defined as in [52]. Therefore, the longitudinal CSR wake function with shielding effect is determined by

$$W^{CSR}(z) = W_{fs}^{CSR}(z) + W_{sh}^{CSR}(z). \tag{2.26}$$

Multi-particle tracking simulations for the ultra-low alpha operating mode with the longitudinal impedance model consisting of RW, BBR and CSR with shielding are presented in following sections.

2.2 Simulations of beam dynamics in storage rings

The beam dynamics in a storage ring can be studied with numerical simulations of the electron motion in the ring lattice, with relevant collective effects by means of multi-particle tracking to investigate instabilities and performance of the storage ring. In the particular case of low alpha storage ring lattices, the dynamics is dominated by beam instabilities driven by short range wakefields. Therefore, the investigation of dynamics in

the low alpha storage ring with the simulation of a single bunch is generally sufficient. For this purpose, we use a code called “single bunch tracking code” or *sbtrack*.

2.2.1 Single bunch tracking code

In order to study the 6D phase space dynamics in storage rings with numerical simulations, we used the multi-particle tracking code *sbtrack* developed in SOLEIL and Diamond [53]. The *sbtrack* is a single bunch tracking code with the possibility to study collective effects modelled by a variety of impedance sources. Available sources in are RW, BBR, CSR, shielded CSR, purely inductive and resistive impedance. A distinctive feature of the version developed at Diamond is the possibility to compute the THz radiation received by a detector in a given bandwidth. In this way we can simulate the THz signal as a function of time on a turn-by-turn basis, as it would be measured at a realistic detector, usually a Schottky barrier diode (SBD) with a given bandwidth. The time pattern of the THz emission can be clearly analysed to define machine parameters with stable THz emission or with bursting THz emission. A nice pictorial way of representing the time pattern of the THz emission is given by the so-called spectrogram where the time pattern of the THz radiation is Fourier analysed and the Fourier amplitude is plotted as a function of the current in the bunch. Such plots provided a large wealth of information on the beam dynamics and can be used to guide the improvement the characteristics of the THz radiation.

The schematic of the simulations performed with *sbtrack* is graphically shown in Figure 2.3. The simulation procedure of *sbtrack* starts with creating the initial 6D particle distribution. The equations of motion can be solved in the so-called one turn map of the 6D motion (see Appendix A). The 6D one turn map is applied to the initial distribution to obtain the new 6D distribution for one turn. Impedance models are built from selected sources and used to compute wakefield kick. The kick is applied to the current particle

distribution and then the one turn map is applied again to get the new distribution. The tracking continues in turn-by-turn basis and the final parameter of the bunch distribution can be extracted at each turn.

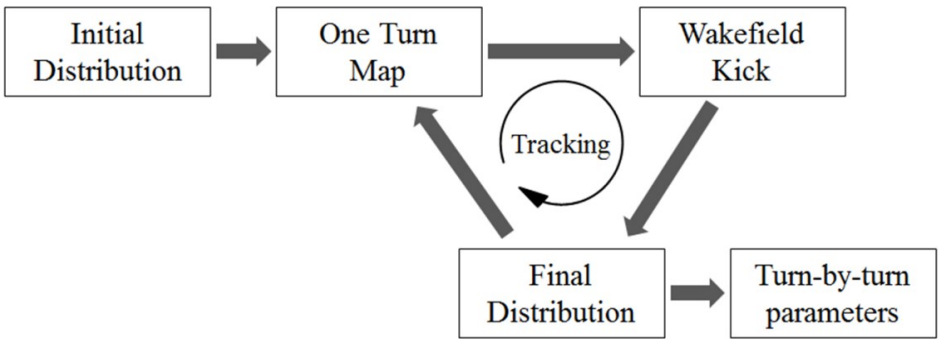


Figure 2.3: Diagram flow of the simulation of the single bunch dynamics with *sbtrack*. The turn-by-turn output include the 6D phase space, bunch profiles, and the THz signal received by a detector in a given bandwidth.

The one turn map from turn n to $n+1$ for the i^{th} electron in the storage ring, is given by [54]

$$\begin{pmatrix} u_i \\ u_i' \end{pmatrix}_{n+1} = M[Q_0(1+\xi_u\delta_n)] \cdot \begin{pmatrix} u_i \\ u_i' \end{pmatrix}_n \tag{2.27}$$

$$\delta_{n+1} = \delta_n + \frac{eV_{RF}}{E_0}\left[\sin\left(\phi_s - \frac{\omega_{RF}}{c}z_n\right) - \sin\phi_s\right] \tag{2.28}$$

$$z_{n+1} = z_n - \alpha_c L_0 \delta_{n+1} \tag{2.29}$$

here u is the transverse coordinate (x or y), δ is the relative energy deviation, z is the longitudinal coordinate, M is the transfer matrix for one turn which depends on the tune Q_0 and the relative chromaticity ξ_u, and L_0 is the storage ring circumference. In Equation (2.28) the longitudinal motion is driven by the RF potential only. The effects of radiation damping and quantum excitation are included to calculate the equilibrium beam parameters such as emittances, beam sizes, energy spread and bunch length by using the relation

$$u'_{n+1} = u'_{n+1} - \frac{2T_0}{\tau_u} u'_{n+1} + \sigma_{u'0} \sqrt{\frac{2T_0}{\tau_u}} R \tag{2.30}$$

$$\delta_{n+1} = \delta_{n+1} - \frac{2T_0}{\tau_s} \delta_{n+1} + 2\sigma_{\delta 0} \sqrt{\frac{T_0}{\tau_u}} R \tag{2.31}$$

where T_0 is the revolution time, τ_u and τ_s are the transverse and longitudinal damping time, $\sigma_{u'0}$ and $\sigma_{\delta 0}$ are standard deviation of beam divergence and relative energy spread of the nominal momentum electron and R is a random number between 0 and 1.

The wakefield kick is added as following

$$u'_{n+1} = u'_{n+1} - \frac{N_e r_0}{\gamma L_0} \int_{-\infty}^{z_i} \lambda(z') D_p(z') \cdot W_\perp(z - z') dz' \tag{2.32}$$

$$\delta_{n+1} = \delta_{n+1} - \frac{N_e r_0}{\gamma L_0} \int_{-\infty}^{z_i} \lambda(z') \cdot W_\parallel(z - z') dz' \tag{2.33}$$

here $r_0 = \frac{e^2}{m_0 c^2}$ is the classical radius of the particle and D_p is the electrical dipole moment of the particle distribution.

2.2.2 Tracking simulations of THz radiation

The *sbtrack* code was translated from C to MATLAB at Diamond including the option to run on an interactive machine or submit a number of jobs in parallel in a cluster. The simulation input includes machine parameters and simulation parameters like the number of macro-particles, turns and bins, and impedance sources and is specified in the *sbtrack* input file. A job submission script is used to specify a bunch current scanning range. Each job is for simulation at one value of the current. The *sbtrack* run produces three output files for each bunch current: the tracking output consists of 6D coordinates in phase space at each turn, beam parameters, bunch profile, form factor, the time signal for the THz emission received turn-by-turn at a detector within a given bandwidth.

The beam dynamics can be broadly summarised in the following: an initial distribution in the 6D phase space is given as input and, in absence of strong wakefields, it performs synchrotron oscillations with the frequency Equation (2.4) and evolves towards the equilibrium values according to the radiation damping time in the corresponding plane of motion. The main parameters for Diamond are reported in Table 2.1.

Table 2.1: Main parameter used in the simulation of the Diamond storage ring.

Parameter	Value
Momentum compaction factor (α)	-2×10^{-6} / -1×10^{-6}
RF voltage	3.4 MV
Beam energy	3 GeV
Chromaticity (ξ_x/ξ_y)	+1 / -0.8
Betatron tune (Q_x/Q_y)	29.389 / 8.285
Beta function (β_x/β_y)	10.65 m / 12.84 m
Alpha function (α_x/α_y)	-0.21 / 0.25
Coupling	0.008
Horizontal emittance (ε_x)	4.4 nm·rad
Natural bunch length	1.0 ps / 0.7 ps
Synchrotron frequency	303 Hz / 214 Hz
Longitudinal damping time	5.59 ms (2987 turns)

Tracking results after several damping times (about seven damping times) are considered in our analysis in order to damp any possible initial transient behaviour due to a mismatch in the initial distribution from the equilibrium one. Most of the simulations were done considering only the longitudinal plane, i.e. reducing the problem to 2D simulations. In this case bunches with 100k macro-particles provide usually sufficient accuracy to get indicative results on the behaviour of the bunch. They are normally checked with more extensive simulations involving up to 2M particles. For the case of Diamond the synchrotron tune is in the order of few hundreds turns depending on the specific machine

conditions, while the damping time is about 3000 turns (5.6 ms) in the longitudinal plane. The synchrotron period is typically more than 1000 turns for low alpha conditions. Therefore the tracking extends a total 30000 turns, from which we exclude the first 10000 that contains few damping times. The last 20000 turns are used for post-processing.

The radiation emitted by each electron on a turn-by-turn is computed according to the low frequency Equation (2.1) and the radiation emitted by the whole bunch is computed from the summation of the form factor within the relevant frequency range according to Equation (2.2). The spectrum of the total radiation emitted is then available on a turn-by-turn basis. The *sbtrack* code is the capable of integrating such spectrum over a given spectral bandwidth to produce a time signal which represents the power emitted by the whole bunch in the specified frequency range. The choice of the frequency range is usually matched to the bandwidth of the detector used. In this way, *sbtrack* can simulate directly the time signal, turn-by-turn, that is received by the detectors.

As an example of *sbtrack* simulations, results for nominal alpha and standard low alpha are presented here.

Nominal alpha mode

As an example of the capability of the code and as reference for further simulation we present the results of the single bunch dynamics simulation for the nominal operation of Diamond. A simulation based on machine parameters for a standard optics for Diamond in nominal alpha of 1.6×10^{-4} and RF voltage of 2.5 MV was done. The machine impedance model used in the model of nominal optics consists of RW with average horizontal half aperture $a = 40\,mm$ and vertical half aperture $b = 12\,mm$ for horizontal and vertical, single BBR with the shunt impedance $R_l = 0.5\,k\Omega$ and resonance frequency $f_l = 8.3\,GHz$

[55], corresponding to the cut off of the vacuum pipe in the arcs of the ring. This is without shielded CSR.

Results from the simulation can be analysed and plotted to show the 2D longitudinal phase space, radiated power in a specific frequency range, for instance 33-50 GHz, longitudinal bunch profile and form factor at specified bunch current as shown below.

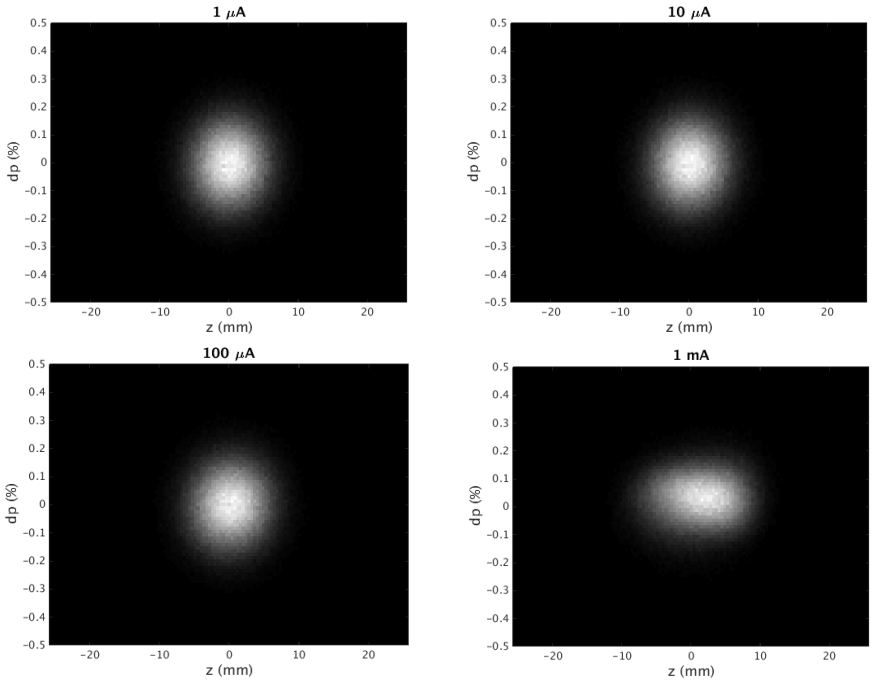


Figure 2.4: Longitudinal phase space of Diamond standard optics in nominal alpha mode at bunch current 1, 10, 100 μA and 1 mA.

The beam at nominal alpha is stable as can be seen from the shape of phase space at different bunch current in Figure 2.4 and the small fluctuation of the power in time in Figure 2.5 (left). The radiated power is calculated in an arbitrary unit from the summation of the form factor within a specific frequency band. The charge density distribution tilts to the head of the bunch ($z > 0$) at higher current as shown in Figure 2.6. The form factor plot in Figure 2.7 determines the spectral range of the coherent radiation from electrons at nominal alpha. The range covers wavenumber below $1\ cm^{-1}$ or ~30 GHz (at 10% of the

maximum value). However, this is below the cut-off frequency of the vacuum pipe in the dipoles which is estimated from [56]

$$f_{cutoff} = \frac{c}{2}\sqrt{\frac{\rho}{h^3}} \tag{2.34}$$

where h is the vacuum chamber height and ρ is the dipole bending radius to be about 165 GHz ($\sim 5.5\ cm^{-1}$) for the bending radius of 7.1 m and the vacuum chamber with the half aperture of 18 mm. In this condition the CSR is suppressed in a measurement at the storage ring.

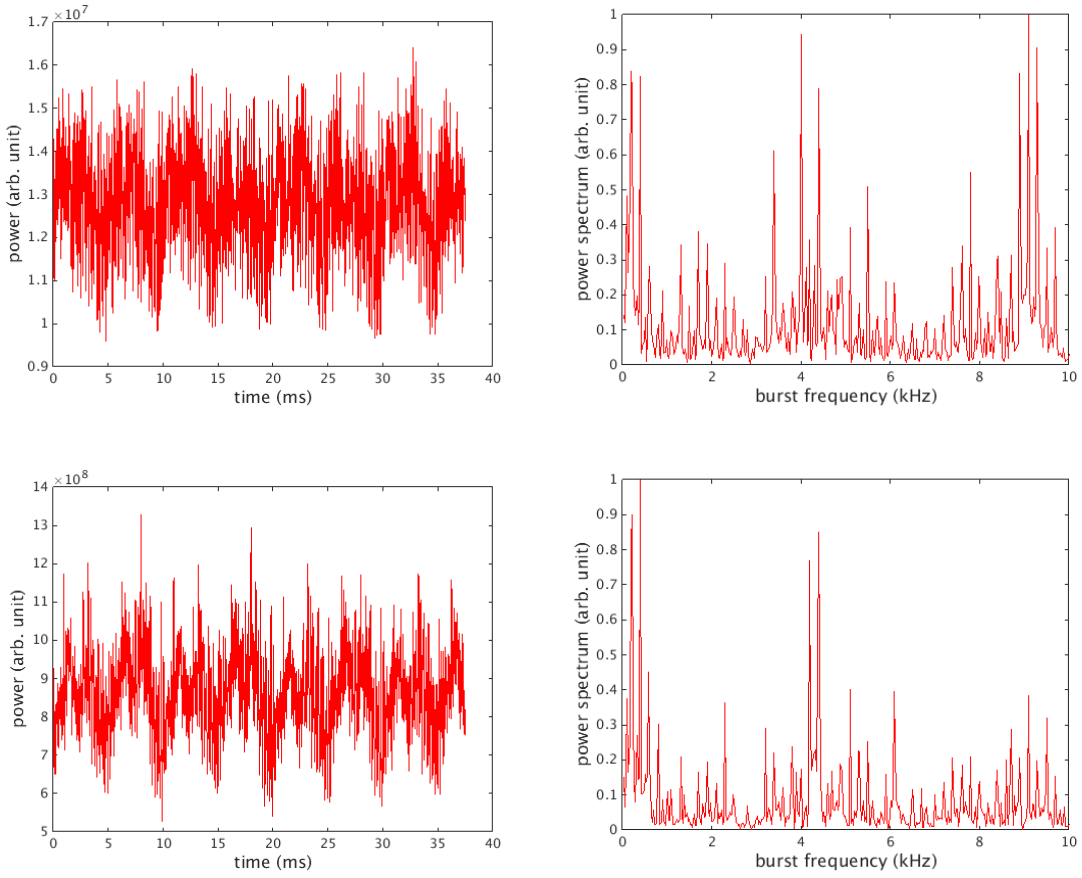


Figure 2.5: Radiated power in time domain (left) and in frequency domain (right) in the range of 33-50 GHz of an electron bunch in nominal alpha mode. The top plots refer to 10 μA the bottom plots refer to 100 μA.

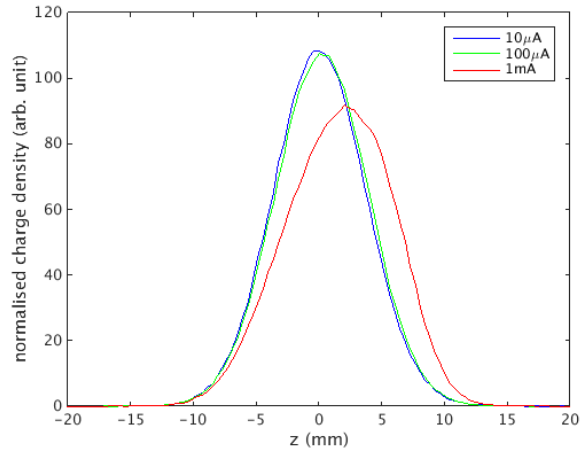


Figure 2.6: Longitudinal bunch profile in 30000th turn in nominal alpha mode at different bunch current.

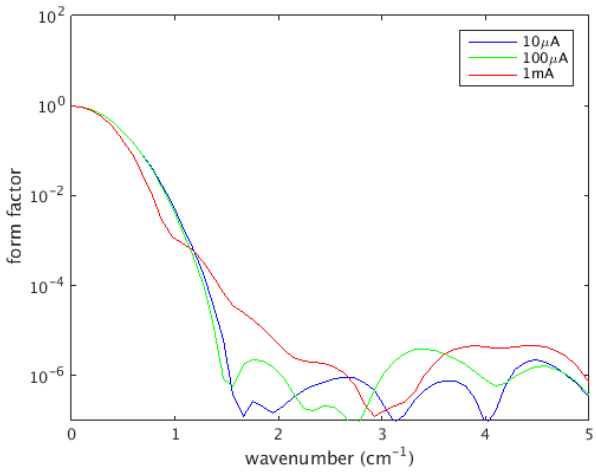


Figure 2.7: Form factor in 30000th turn given by Fourier transform of the profile at bunch current 10 μA, 100 μA and 1 mA operated in nominal alpha.

The mean and standard deviation of the 6D coordinates over the total number of macro-particles for all tracking turns are calculated in the main *sbtrack* code and recorded also in the output files. The rms bunch length for each bunch current can be obtained from the average of the rms longitudinal position of electrons in the bunch over analyse turns as shown in Figure 2.8.

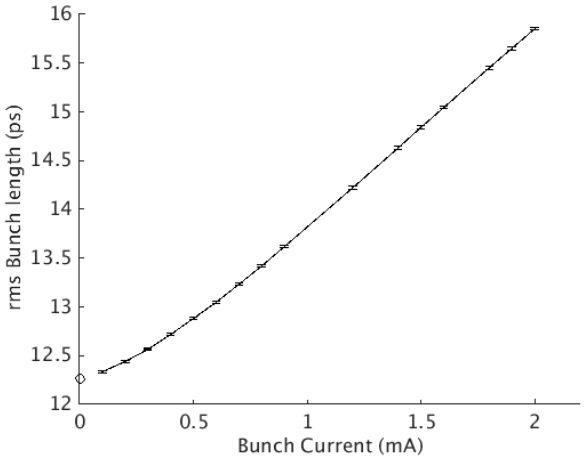


Figure 2.8: Bunch lengthening with bunch current in nominal alpha operation.

Standard low alpha mode

We investigate now the beam dynamics in the low alpha operating mode relative to lattices with $\alpha_c = \pm 1 \times 10^{-5}$. The value $\alpha_c = -1 \times 10^{-5}$ corresponds to the lattice normally used in low alpha operation. The simulations with positive alpha $\alpha_c = +1 \times 10^{-5}$ are reported to highlight the difference in the dynamics in the two cases.

The standard low alpha mode for Diamond storage ring is operated at $\alpha = -1 \times 10^{-5}$ with RF voltage of 3 MV. The impedance model used in the standard low alpha mode consists of RW with average horizontal half aperture $a = 40\ mm$ and vertical half aperture $b = 12\ mm$ for horizontal and vertical, single BBR with the shunt impedance $R_l = 0.5\ k\Omega$ and resonance frequency $f_l = 8.3\ GHz$, and shielded CSR. The phase space in Figure 2.9 shows that the longitudinal phase space is blown out at high bunch current, as clearly seen at 1 mA. This implies that the beam dynamics is more sensitive to the bunch current than in case of nominal alpha since the phase space in nominal alpha is completely stable at the same current (Figure 2.4). The dynamics in the phase space at bunch current of 100 μA is illustrated in detail in Figure 2.10. The phase space leans towards the tail ($z < 0$) and rotates clockwise.

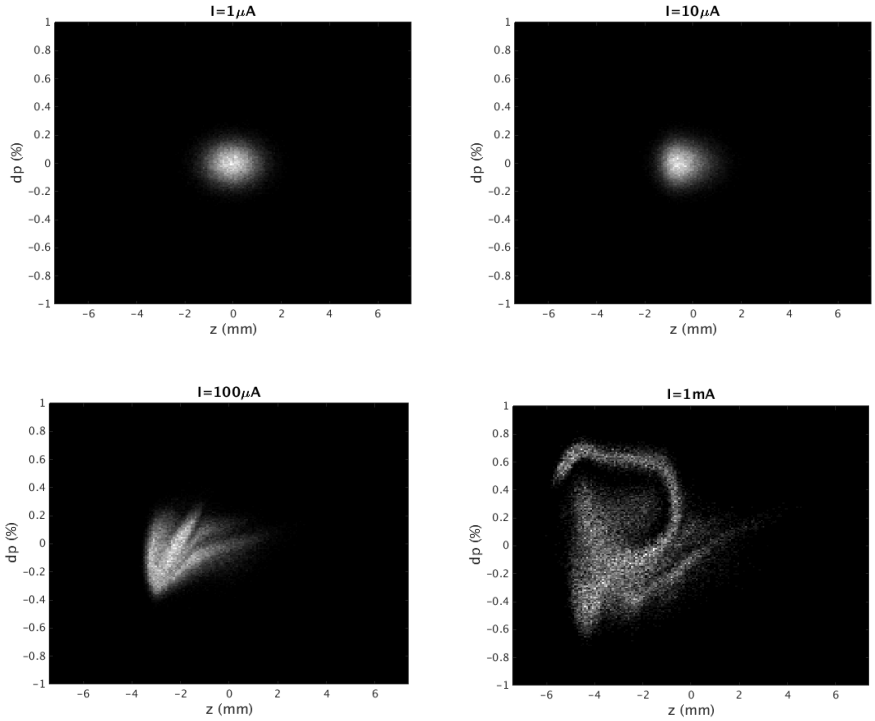


Figure 2.9: Longitudinal phase space in standard low alpha mode at bunch current 1, 10, 100 μA and 1 mA, after 30000 turns.

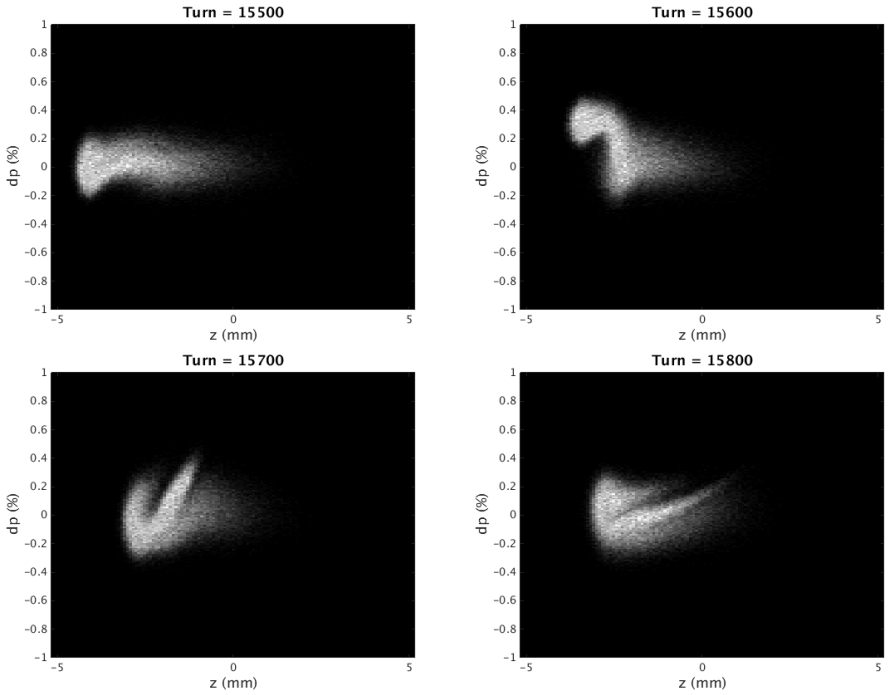


Figure 2.10: Longitudinal phase space of $\alpha = -1 \times 10^{-5}$ and RF voltage of 3 MV at 100 μA. The phase space rotates clockwise.

In Figure 2.11, we report the time signal of the CSR power and its Fourier transform: we found that the CSR is radiated at a specific frequency around 1.5 kHz at 10 μA and about 1.2 and 2 kHz at 100 μA which are not present in the case of nominal alpha (Figure 2.5). This is a sign of bursting occurring at high current which will be discussed later.

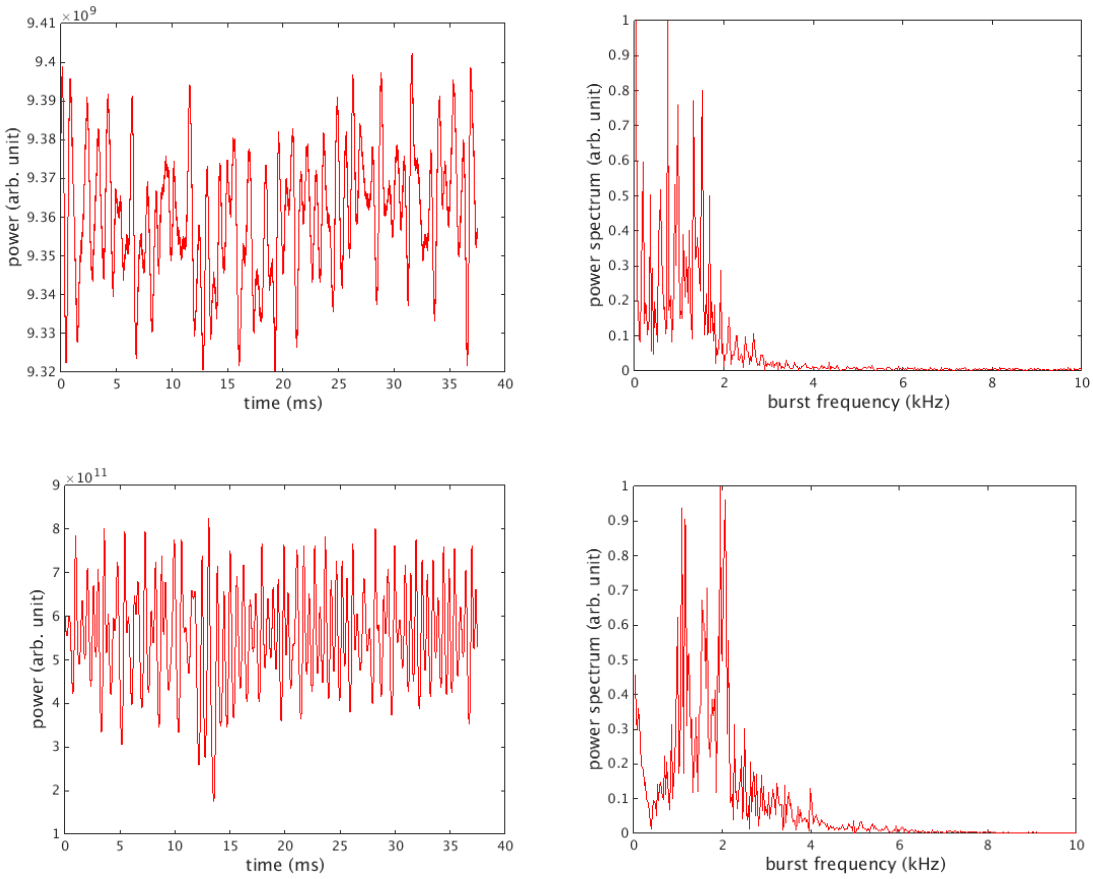


Figure 2.11: Radiated power in time domain (left) and in frequency domain (right) in the range of 33-50 GHz of an electron bunch in standard low alpha mode. The top plots refer to 10 μA the bottom plots refer to 100 μA.

Since the wakefields are strong at the back of the bunch, the bunch profile is not a Gaussian distribution and tilts to the tail of the bunch ($z < 0$) as seen in Figure 2.12. The form factors at 10 μA and 100 μA are shown in Figure 2.13 which demonstrates that, by operating in low alpha mode, the spectral range is pushed to higher wavenumber or

frequency than the spectral range radiated in nominal alpha (compared with Figure 2.7). The bunch is shortened at low current below 10 μA and is then lengthened at higher current as shown in Figure 2.14 following the behaviour in negative alpha.

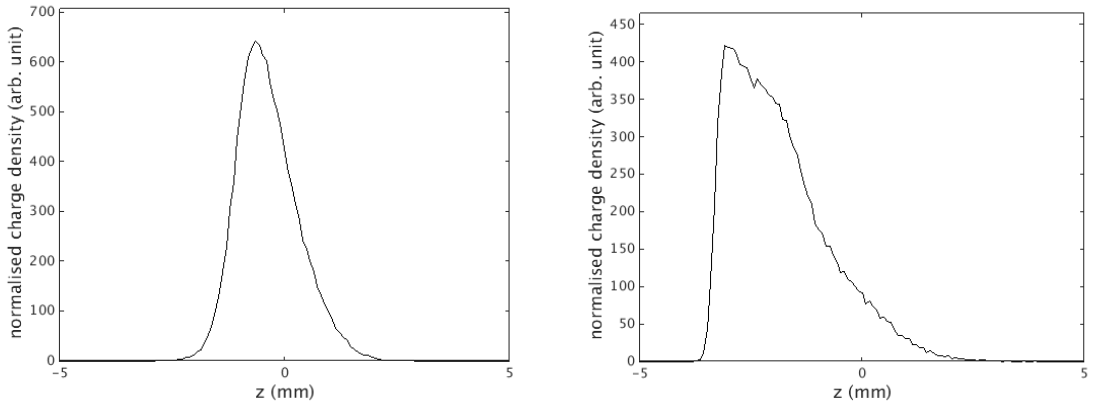


Figure 2.12: Longitudinal bunch profile of a bunch in standard low alpha mode after 30000 turns at 10 μA (left) and at 100 μA (right).

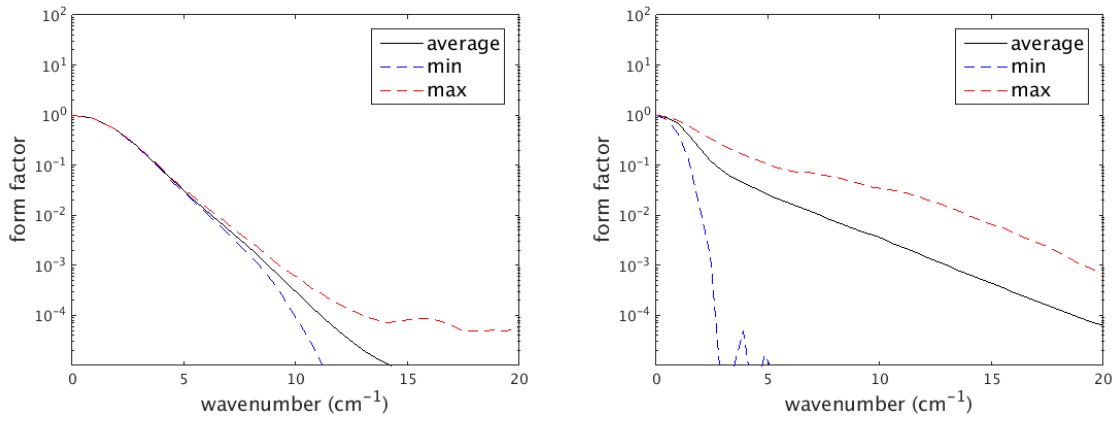


Figure 2.13: Form factor given by Fourier transform of the profile at bunch current 10 μA (left) and 100 μA (right) operated in standard low alpha mode.

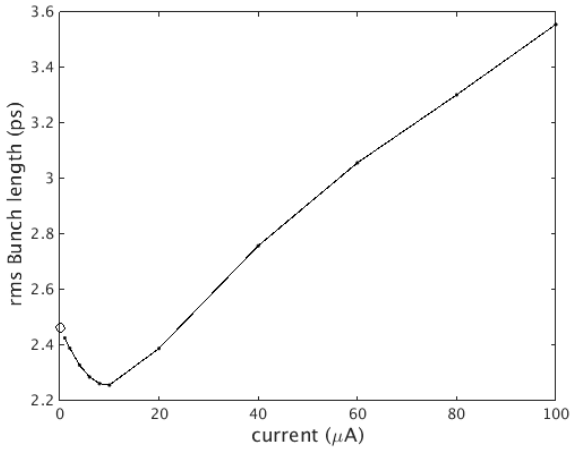


Figure 2.14: Bunch lengthening in standard low alpha mode. Compare with Figure 2.8 for the bunch lengthening curve for nominal operating parameters.

The characteristics of the radiation produced by short electron bunches circulating in a storage ring operating in standard low alpha depend strongly on the beam current. The CSR from short bunches can be separated into two modes: steady state and bursting mode. In steady state, the wakefields interact with the electron bunch but a new stable distribution is reached. As a result, the form factor in Equation (1.24) determined by the bunch distribution is changed in a way that the frequency range of CSR is pushed to higher frequency. The bunch continues radiating steady CSR until the current exceeds a threshold known as bursting instability threshold. At currents higher than the bursting threshold, the combined effects of the wakefields drive a longitudinal bunch density modulation and induce micro-bunching instability. This initiates the bursting radiation. The bunch which emits CSR heavily becomes unstable. It then starts to lose it charge and the energy spread increases rapidly.

From the *sbtrack* output we obtain a wealth of information on the beam dynamics and the emission of THz radiation on a turn by turn basis. The time signal of the THz power is used to build the so-called spectrograms in the following way. First we collect the time pattern of the emission over a number of turns (usually from turn 10000 to turn

30000). And we collect one signal for each single bunch current. Then we perform the Fourier transform of each of these signals. The time swept is a single turn ($\Delta t = 1.87\ \mu s$ at Diamond) therefore the maximum frequency available in these spectra will be $\Delta\nu \sim 1/\Delta t = 533\ kHz$. We then consider the amplitude of the Fourier transform of the THz power signal and we build a colour plot of the amplitude of the FFT as a function of the current. This is called spectrogram. The simulated spectrogram can then be compared with the measured ones built from the time signal of the THz power measured at the detectors. Examples of simulated spectrograms are given in Figure 2.15 and following figures, while the measured spectrograms are given in Figure 2.34 and following figures.

As an example, the spectrogram in Figure 2.15 has frequency on the horizontal axis, bunch current on the vertical axis and the amplitude of the Fourier transform shown in colour. The spectrogram can be plotted taking the time signal of the THz radiation detected in a specific bandwidth. The SBD detectors available at Diamond cover eight different bandwidths given in Table 2.2. Figure 2.15 shows the spectrograms for standard low alpha mode in these eight bandwidths. The first bursting pattern appears at 50 μA at bursting frequency 1.2 kHz and shifts to 2 kHz at 100 μA in all bandwidths. The patterns at harmonic of the frequency 1.2 kHz with the threshold current also 50 μA are present especially in the bandwidth 140-220 GHz and 220-330 GHz.

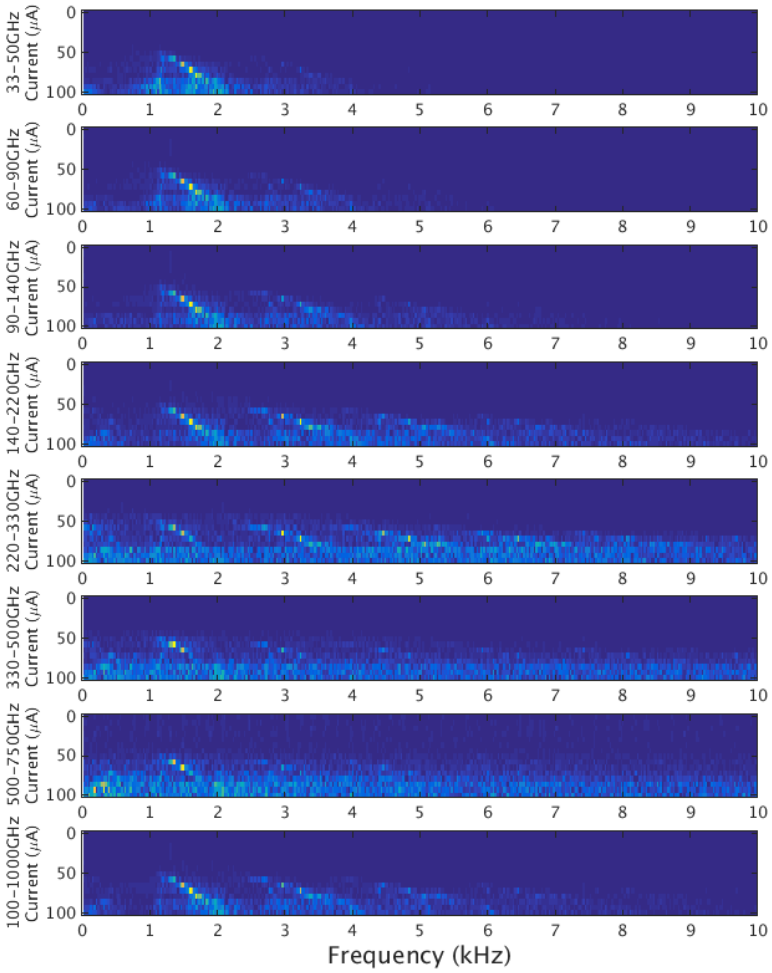


Figure 2.15: Simulated spectrogram from standard low alpha mode in eight bandwidths of SBDs available at Diamond.

Table 2.2: SBD detectable frequency range.

Detector number	Frequency range
1	33-50 GHz
2	60-90 GHz
3	90-140 GHz
4	140-220 GHz
5	220-330 GHz
6	330-500 GHz
7	500-750 GHz
8	100-1000 GHz

It is important to highlight that if the motion is stable, the emission pattern in time will also be stable and the spectrogram will be relatively simple. However, in presence of

instabilities of bursts, the time emission is increasingly chaotic and the spectrogram will display a complex frequency structure. In particular, it is interesting to note that sudden transition from regular pattern of emission to chaotic patterns occur for tiny changes in the bunch current at the bursting threshold.

Positive low alpha mode

We now present the result of the simulations for positive low alpha mode operating in $\alpha = +1 \times 10^{-5}$ with RF voltage of 3 MV. The impedance model used is the same as the standard low alpha mode consisting of RW with average horizontal half aperture $a = 40\ mm$ and vertical half aperture $b = 12\ mm$ for horizontal and vertical, single BBR with the shunt impedance $R_l = 0.5\ k\Omega$ and resonance frequency $f_l = 8.3\ GHz$, and shielded CSR.

Similar to the standard low alpha (with negative alpha), the phase space blown out at bunch current below 100 μA as shown in Figure 2.16 but the phase space develops patterns similar to legs in the case with positive alpha. The dynamics of the phase space at current of 100 μA in Figure 2.17 shows that a leg is formed at the back of the bunch with negative momentum deviation and it is lengthened when the whole phase space rotates anticlockwise to the front. The leg then disappears when momentum spread becomes positive.

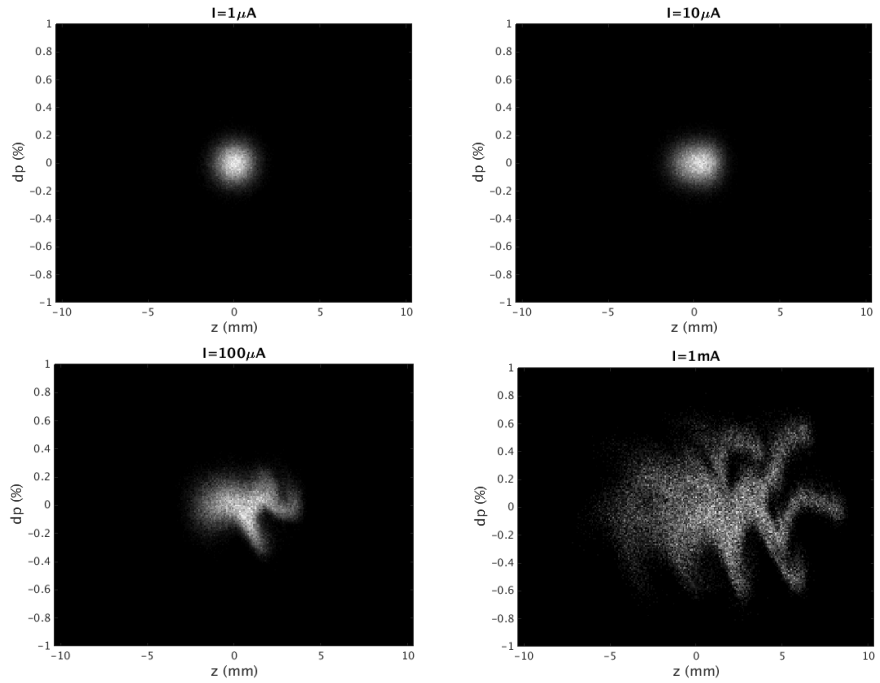


Figure 2.16: Longitudinal phase space in positive low alpha mode at bunch current 1, 10, 100 μA and 1 mA after 30000 turns.

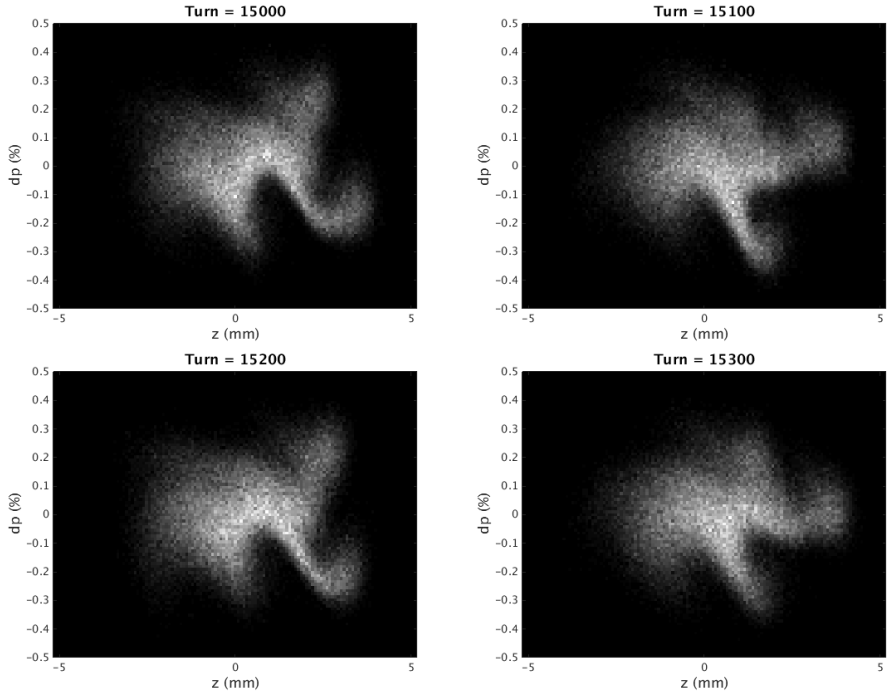


Figure 2.17: Longitudinal phase space of $\alpha = +1 \times 10^{-5}$ and RF voltage of 3 MV at 100 μA. The phase space rotates anticlockwise.

The CSR power time signal in Figure 2.18 shows the bursting frequency below 1.5 kHz at 10 µA and about 2 kHz at 100 µA. It is clearly seen in Figure 2.19 that the bunch moves towards the head of the bunch for positive alpha. The form factor given in Figure 2.20 in positive low alpha covers a narrower frequency band compared with the (negative) standard low alpha (Figure 2.13) but it still broader than the form factor in nominal alpha (Figure 2.7). The bunch lengthening curve in Figure 2.21 clearly shows longer bunch length than the curve in standard low alpha (Figure 2.14).

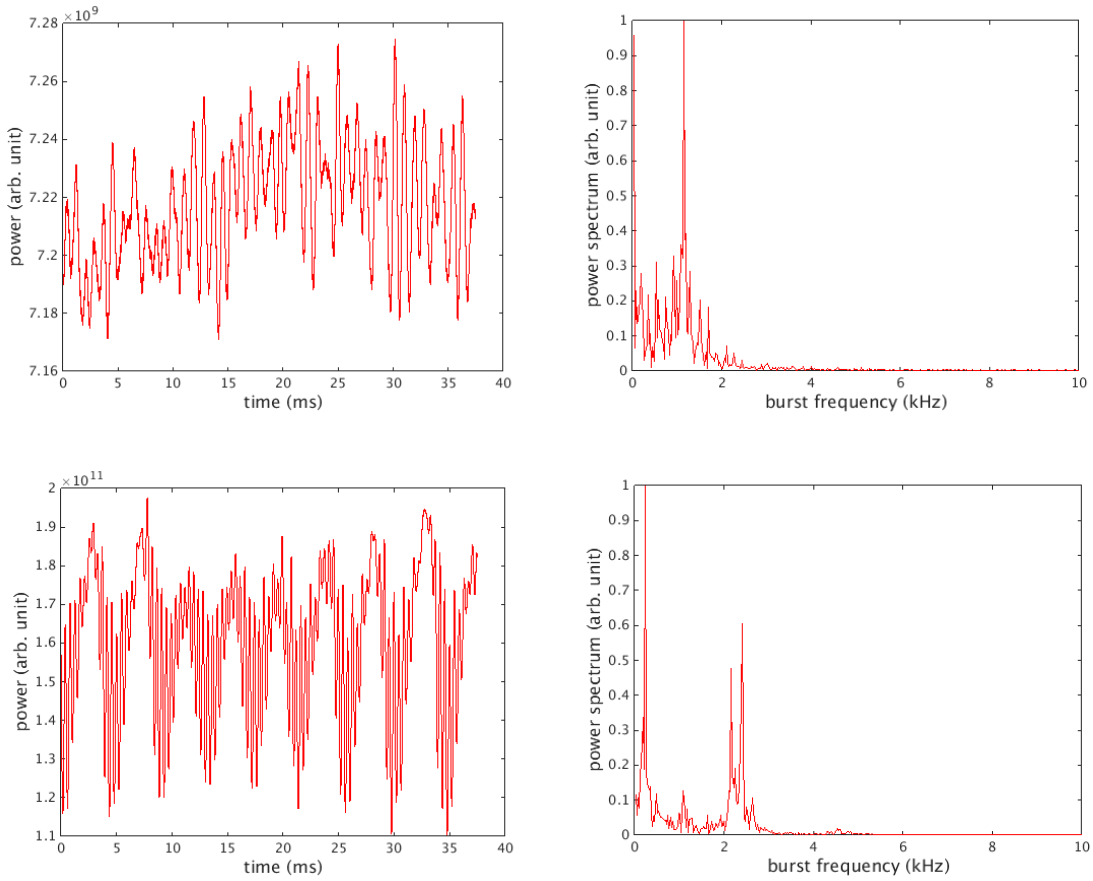


Figure 2.18: Radiated power in time domain (left) and in frequency domain (right) in the range of 33-50 GHz of an electron bunch in positive low alpha mode. Top plots refer to 10 µA and bottom plots refer to 100 µA.

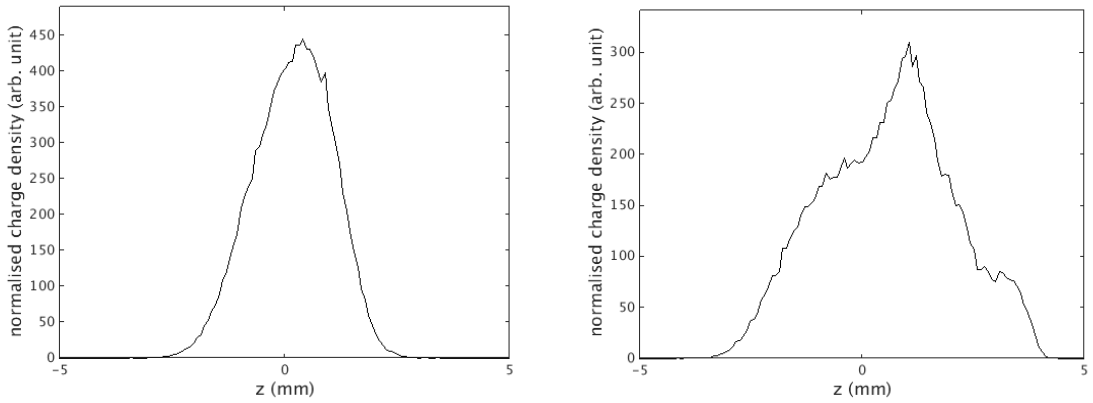


Figure 2.19: Longitudinal bunch profile in positive low alpha mode after 30000 turns at 10 μA (left) and at 100 μA (right).

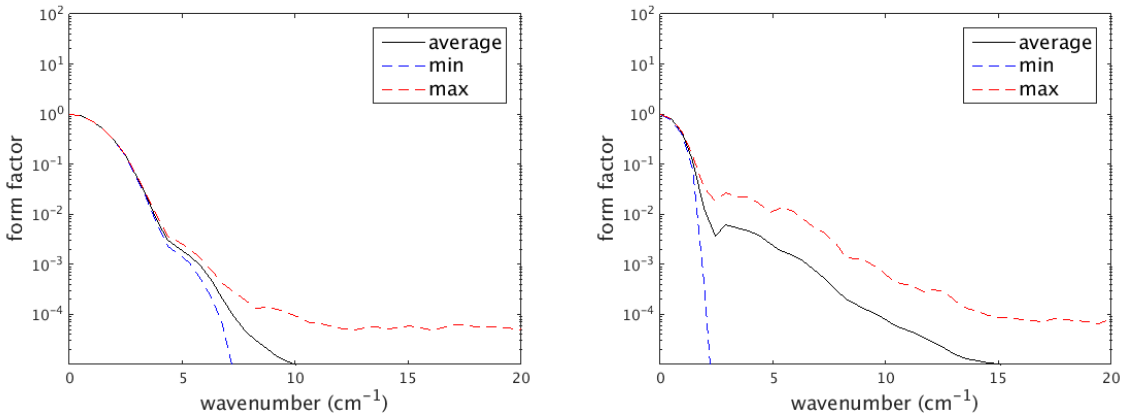


Figure 2.20: Form factor given by Fourier transform of the profile operated in positive low alpha mode. Left plot refers to 10 μA and right plot refers to 100 μA.

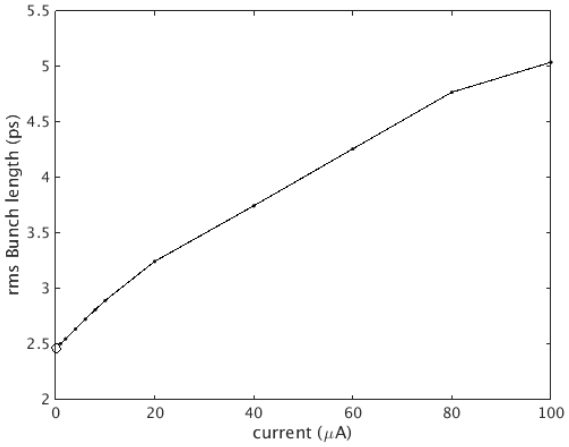


Figure 2.21: Bunch lengthening in positive low alpha mode. Compare with Figure 2.14 for the bunch lengthening curve for standard low alpha mode.

The bursting patterns can be seen in the spectrogram in Figure 2.22 except the bandwidth 500-750 GHz, where the bursting pattern seem to be washed out, probably because no substructures with that wavelengths develops within the bunch. The bursting threshold current is 60 µA and the first bursting pattern starts at bursting frequency 1.8 kHz and shift to 2.2 kHz at bunch current 100 µA. Higher frequency patterns at harmonic frequency of 1.8 kHz can be seen also.

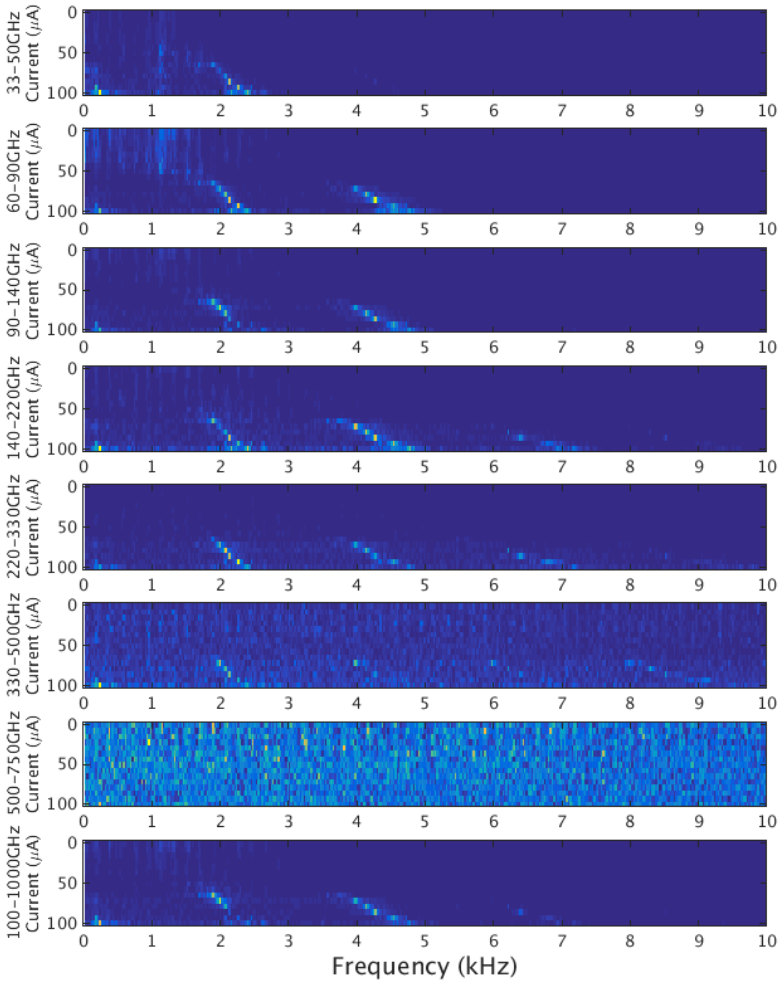


Figure 2.22: Simulated spectrogram from positive low alpha mode in eight bandwidths of SBDs available at Diamond.

From these simulations it is clear that reducing the momentum compaction factor increases the production of coherent THz radiation either via shortening the bunch or by

creating micro-bunch structures, mostly seen in positive alpha. Stable radiation is emitted in low alpha to sub-mm wavelengths.

2.3 Simulations of THz CSR generated in ultra-low alpha mode in Diamond storage ring

Under the users' requests of extending the frequency range of the emission to higher frequency (corresponding to wavelengths in the order of few hundreds of μm) we have investigate the option of further reducing the bunch length. Although operating the storage ring with shorter bunches reduces the maximum bunch current due to the instabilities developing in standard low alpha (50 μA) and of positive low alpha (60 μA), it was noted that the THz/IR beamline at Diamond beam still uses attenuators to reduce the power by factor of 30-40 in the standard low alpha mode [57]. This observation enabled the idea of attempting to reduce the bunch length even further at the expense of a further reduction of the beam current. We therefore proposed to operate the Diamond storage ring in the so called "ultra-low alpha mode" in order to reduce the bunch length below the values used in the low alpha mode. In this dedicated mode, the ultra-short bunch length can be achieved by both using higher RF voltage and pushing forward the tuning of the lattice as explained in previous sections.

In this section, we discuss the tracking simulations using the code *sbtrack* to investigate and evaluate the beam dynamics and performance of the proposed ultra-low alpha operating mode at two alpha values: (1) -2×10^{-6} and (2) -1×10^{-6} which is 5 and 10 times, respectively, lower than the low alpha mode (according to the low-alpha, low-emittance lattice presented in [58]). The expected natural bunch lengths are $\sigma_\tau = 1\ ps$ and $\sigma_\tau = 0.7\ ps$, respectively as given in Table 2.1. The proposed machine parameters are given in Table 2.3. It is expected that in such a mode significantly shorter electron bunches

are created. Comparisons between the simulations and measurements will be presented in the following section.

Table 2.3: Machine parameters for ultra-low alpha operating mode at Diamond storage ring.

Parameter	Value
Momentum compaction factor (α)	-2×10^{-6} / -1×10^{-6}
RF voltage	3.4 MV
Synchrotron frequency	303 Hz / 214 Hz
Maximum bunch current	14.4 μA / 9.5 μA
The number of bunches	800
Chromaticity (ξ_x/ξ_y)	+1 / -0.8
Betatron tune (Q_x/Q_y)	29.389 / 8.285

The model used for the longitudinal impedance used in the simulations is a combination of BBR, resistive wall and CSR with shielding. The impedance was used as fit parameters to match the bunch length measurement results. From our results, the best fit parameters of the impedance models are presented as following.

The BBR impedance is modelled as a combination of two single broad-band ($Q = 1$) resonators. One is a low-frequency resonator with the shunt impedance $R_l = 0.5\ k\Omega$ and the resonance frequency $f_l = 8.3\ GHz$ for the model for normal operating mode [55]. The second is a high-frequency resonator with the shunt impedance $R_l = 90\ k\Omega$ and the resonance frequency $f_l = 100\ GHz$. While the low frequency BBR component is well justified as it is close to the cut-off frequency of the vacuum pipe, the high frequency component at 100 GHz is not easily ascribable to any particle structure in the pipe. The best conjecture to explain its presence is that it is close to the cut-off frequency of the vacuum pipe in the dipole sections, as discussed for Equation (2.34).

The resistive-wall impedance is used with average half aperture $a = 40\,mm$ and $b = 12\,mm$ for horizontal and vertical size of the stainless steel vacuum chamber. These correspond to the actual average values of the aperture in the Diamond pipe.

The bunch profile and bending radius of 7.1 m are used to calculate the CSR wakefield. The shielding effect of the dipole vessel with the half aperture of 18 mm is also considered and included in the CSR model. It is important to observe that while the choice of the BBR parameters is the result of a fit on bunch lengthening curves, the expression for the resistive wall and the CSR do not have any fit parameter.

2.3.1 Bunch lengthening

Our impedance model gives the current-dependent bunch length for two alpha cases as shown in Figure 2.23.

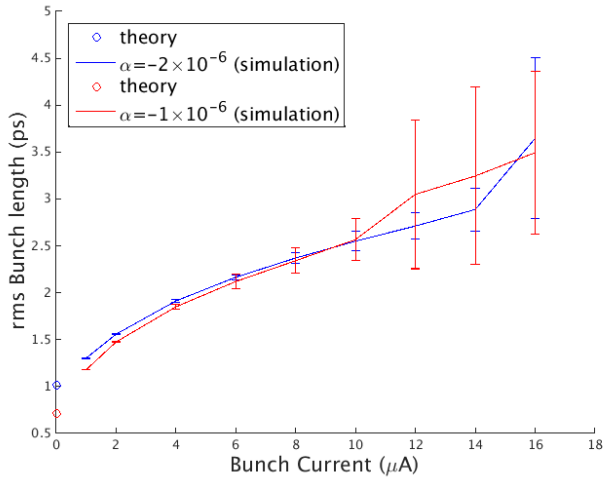


Figure 2.23: Simulated rms bunch length as a function of the single bunch current for $\alpha = -2 \times 10^{-6}$ (blue) and $\alpha = -1 \times 10^{-6}$ (red). The circles are the theoretical values for the zero current bunch length. This can be compared with the simulated rms bunch length for low alpha mode shown in Figure 2.14 (valid for negative alpha).

The theoretical bunch length is the natural bunch length at zero current for each case and the error bars are standard deviation of bunch length. The bunch length for $\alpha = -1 \times$

10^{-6} is shorter than the bunch length for $\alpha = -2 \times 10^{-6}$ at low current, but as the current increase the collective effects wash out this difference and the bunch length converge quite rapidly at about 2 μA. Notice that the rms bunch length is always large than 0.5 ps, hence the associated bunch spectrum extends to frequencies up to ~2 THz.

2.3.2 Spectrogram

The simulated spectrograms of CSR in eight specific frequency bandwidth of Table 2.2 are illustrated in Figure 2.24 and 2.25 for both alpha values.

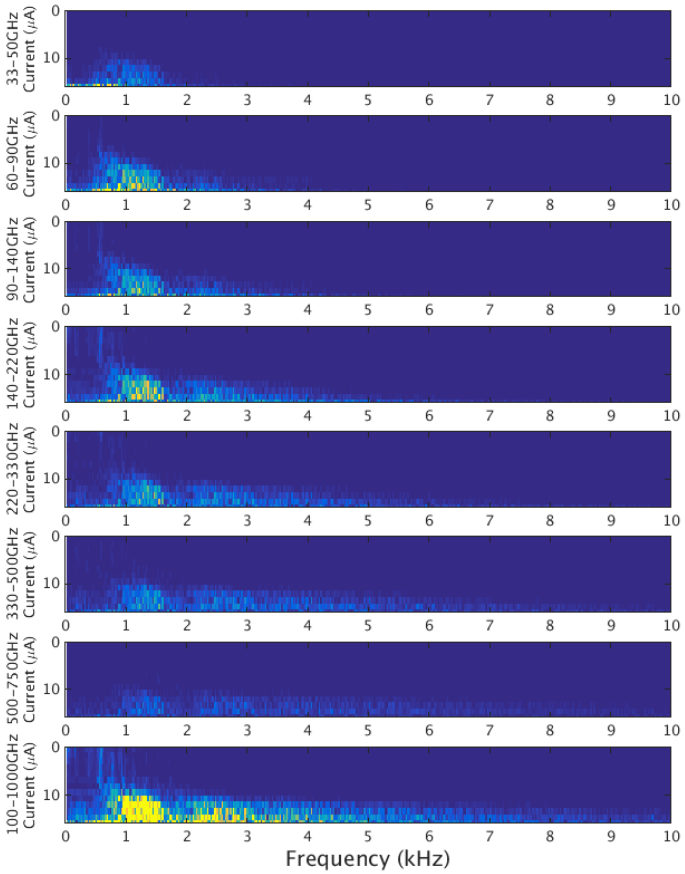


Figure 2.24: Simulated spectrogram for $\alpha = -2 \times 10^{-6}$ in the specific ranges of the SBD detectors.

From the result of $\alpha = -2 \times 10^{-6}$ in Figure 2.24, the spectrogram pattern highlighting the onset of bursting CSR begins to appear at ~8 μA. The CSR bursts at

frequency of 1 kHz and shifts to higher frequency with increasing current. The bursting structure covers a broad frequency.

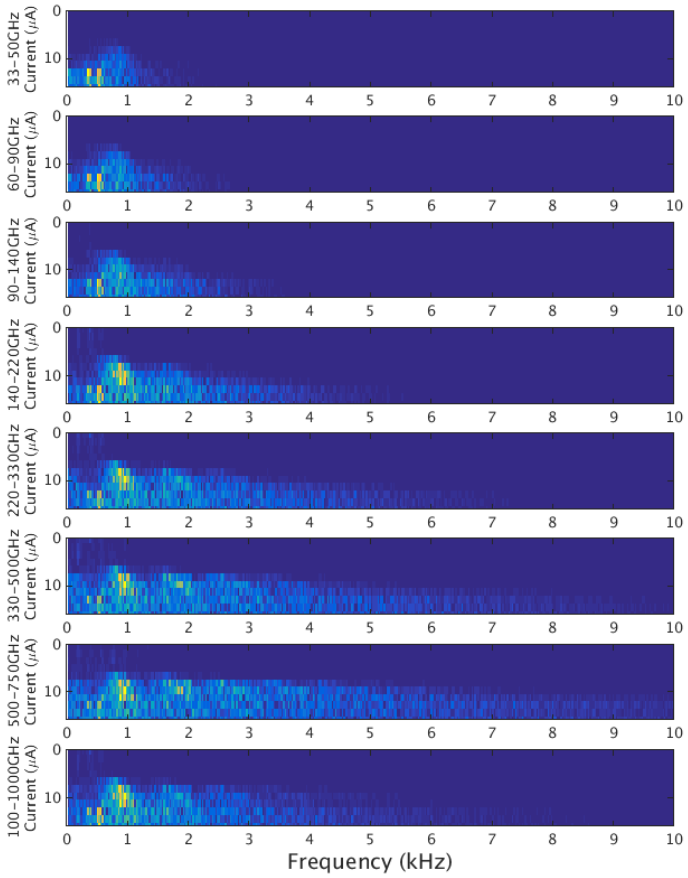


Figure 2.25: Simulated spectrogram for $\alpha = -1 \times 10^{-6}$ in the specific ranges of the SBD detectors.

In the case of $\alpha = -1 \times 10^{-6}$ in Figure 2.25, the bursting CSR structures also start to appear at ~8 μA with the frequency of the bursting just below 1 kHz but covering narrower frequency range than the high alpha case.

2.3.3 CSR spectrum

The frequency range of the CSR emitted can be determined from the form factor of the simulated longitudinal bunch profile. The form factors at 10 μA for $\alpha = -2 \times 10^{-6}$ and $\alpha = -1 \times 10^{-6}$ are shown in Figure 2.26 and 2.27 respectively. Clearly, the spectral

range of the lower alpha case extends to higher wavenumber, as compared to the form factor obtained in standard low alpha (see Figure 2.13).

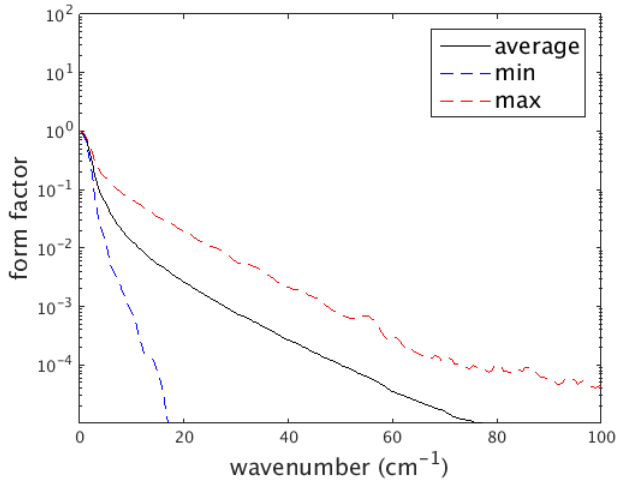


Figure 2.26: Form factor of the simulated bunch for $\alpha = -2 \times 10^{-6}$ at 10 μA.

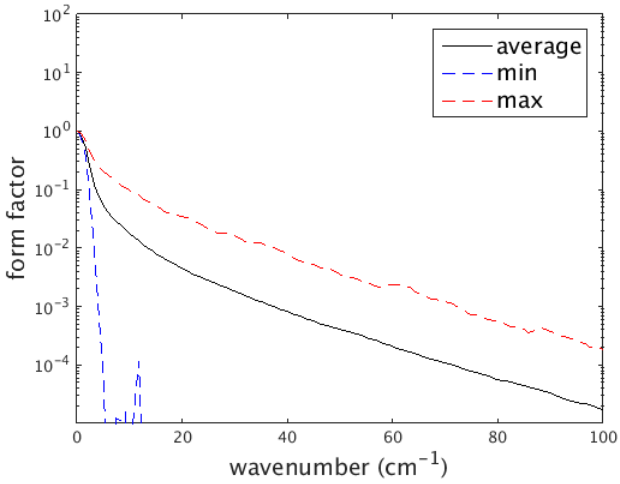


Figure 2.27: Form factor of the simulated bunch for $\alpha = -1 \times 10^{-6}$ at 10 μA.

2.3.4 Longitudinal phase space

The longitudinal phase space at 10 μA for $\alpha = -2 \times 10^{-6}$ and $\alpha = -1 \times 10^{-6}$ is shown in Figure 2.28 and 2.29, respectively, in steps of 100 turns. In both cases the movement of the phase space distribution is a clockwise rotation. However, the bunch

develops a larger momentum spread in the lower alpha case as shorter bunch length has more charge density and the beam dynamics in phase space is more complicated.

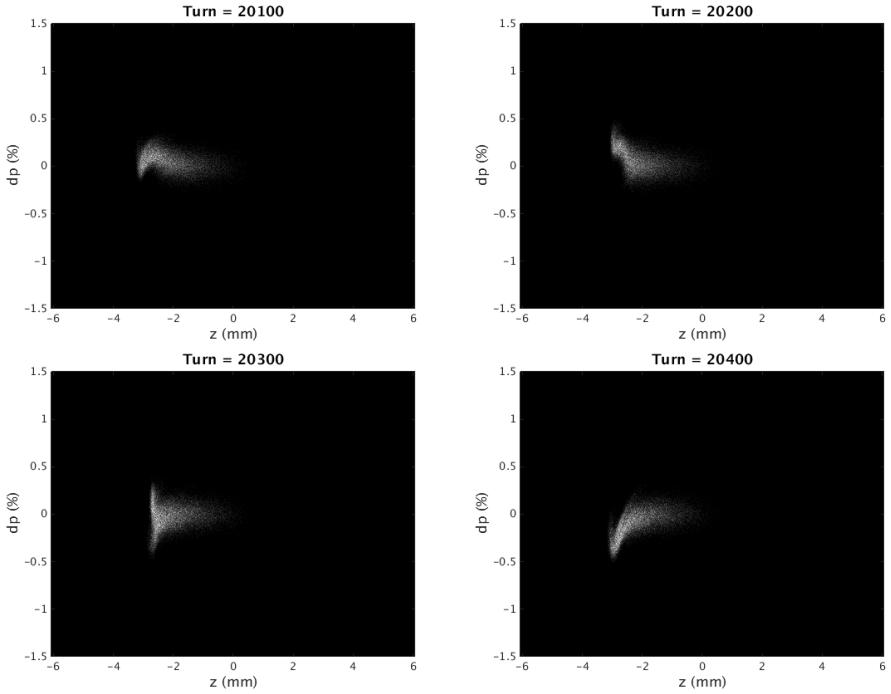


Figure 2.28: Longitudinal phase space for a case with $\alpha = -2 \times 10^{-6}$ at 10 μA.

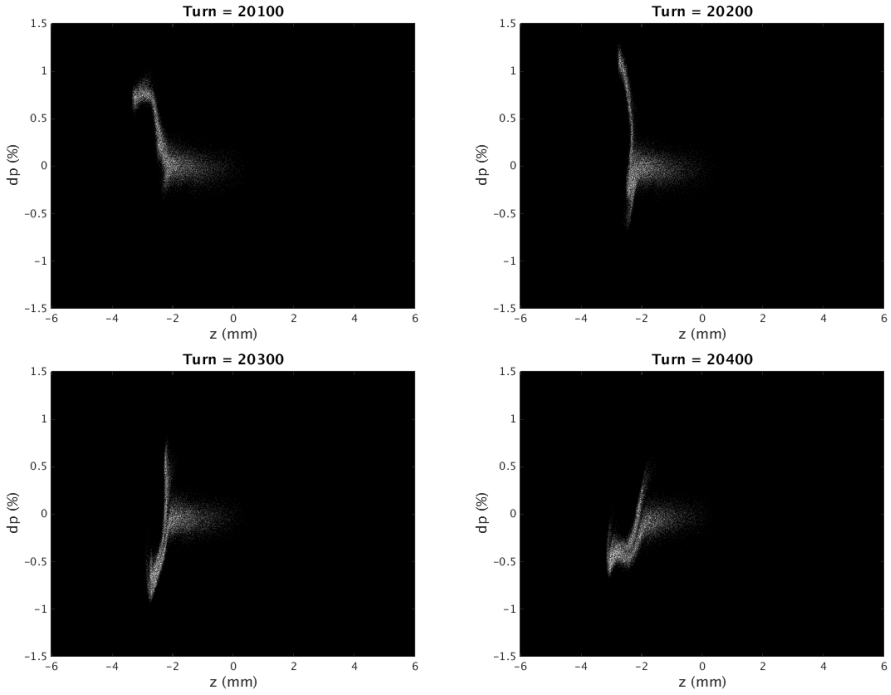


Figure 2.29: Longitudinal phase space for a case with $\alpha = -1 \times 10^{-6}$ at 10 μA.

The simulation results give important information on the beam dynamics and the emission of THz radiation that can be verified in the experimental tests of the ultra-low alpha mode of operation on the Diamond storage ring.

2.4 Measurements of THz CSR generated in ultra-low alpha mode

Experimental tests of the ultra-low alpha mode were conducted to understand the machine performance and the characteristics of the CSR by means of the FTIR interferometer at beamline B22 [3] and with the set of SBD detectors described in Table 2.2, simultaneously.

In this section, we review the measurement techniques used for monitoring THz CSR and experimental results of ultra-low alpha.

2.4.1 Measurement techniques for diagnostics of CSR in Diamond storage ring

Momentum compaction factor measurement

At Diamond, the momentum compaction factor of the lattice is indirectly determined by measuring synchrotron frequency using Equation (2.4). The phase of RF cavities is modulated to excite synchrotron oscillations which can be measured with a beam position monitor (BPM) at a location with high transverse dispersion. The synchrotron frequency can be extracted from the Fourier transform of the horizontal displacement recorded by the BPM. The momentum compaction factor is then evaluated by the relation given by Equation (2.4).

Spectrum measurement with Schottky barrier diodes

Schottky Barrier Diodes (SBDs) are used to measure the emission of THz radiation. SBD is a semiconductor diode well-known from its low forward voltage drop, picosecond response time and excellent room-temperature sensitivity for detecting radiation in mm-

wavelength range. SBDs are suitable for detecting THz radiation because they are very sensitive to mm-waves, and can be operated at room temperature [59]. The fast response of the SBDs allows turn-by-turn and bunch-by-bunch detection of CSR in THz range. Each SBD has specific operating frequency band depending on size of horn antenna that couples the radiation onto the detector. Several SBDs are used simultaneously to cover broader bandwidth to detect turn-by-turn radiation as shown in Figure 2.30.

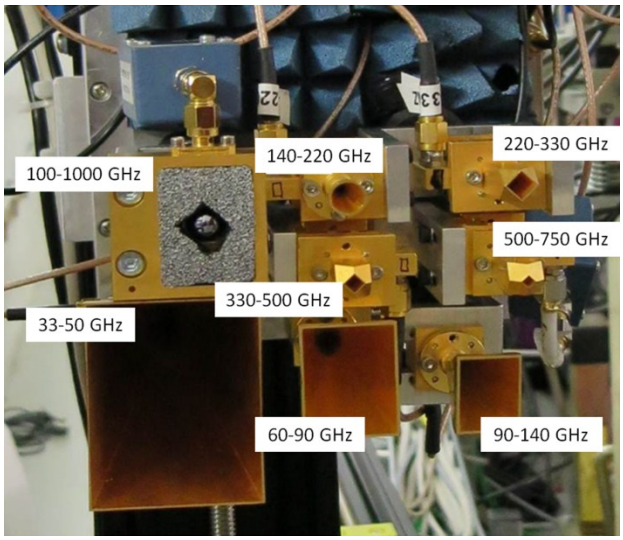


Figure 2.30: Arrangement of array of SBDs [60].

The THz pulses detected turn-by-turn are post-processed by Fast Fourier Transform (FFT) to build the spectrograms.

Spectrum measurements with Fourier Transform Infrared interferometer

Fourier Transform InfraRed (FTIR) interferometer is normally used to investigate absorption properties of samples in the infrared spectrum. It is basically a Michaelson interferometer as shown in Figure 2.31. IR radiation of synchrotron radiation from the storage ring is transferred through a beamline to the interferometer at an experiment end station. In the interferometer, the IR light is split by a beam splitter into two ways: half of the light is reflected to a stationary mirror and the other half is refracted to a moving mirror.

The light in both directions is reflected by a stationary and a moving mirror. The reflected light is recombined at the beam splitter and reflected onto a sample placed on the other arm in the interferometer. The sample absorbs some spectrum of the light and the remaining is then passing through to a detector. The optical path difference between reflected light from two mirrors is changed by the movement of the moving mirror with an adjustable scanning velocity. The interference pattern at the detector can be plotted as a function of the optical path difference. This is known as the interferogram. The interferogram is converted by Fourier transformation to the spectrum. Since the acquisition time of an interferogram requires up to 1 minute, depending on the mirror scan velocity, it is clear that the FTIR does not deliver turn-by-turn spectral information but spectra averaged over certain number of electron bunches and revolutions. However the FTIR is the instrument mostly used in THz/IR beamline to carry out the experiment in absorption or transmission spectroscopy, therefore the quality of the THz source has to be judged eventually by the FTIR analysis as will be done the next paragraph.

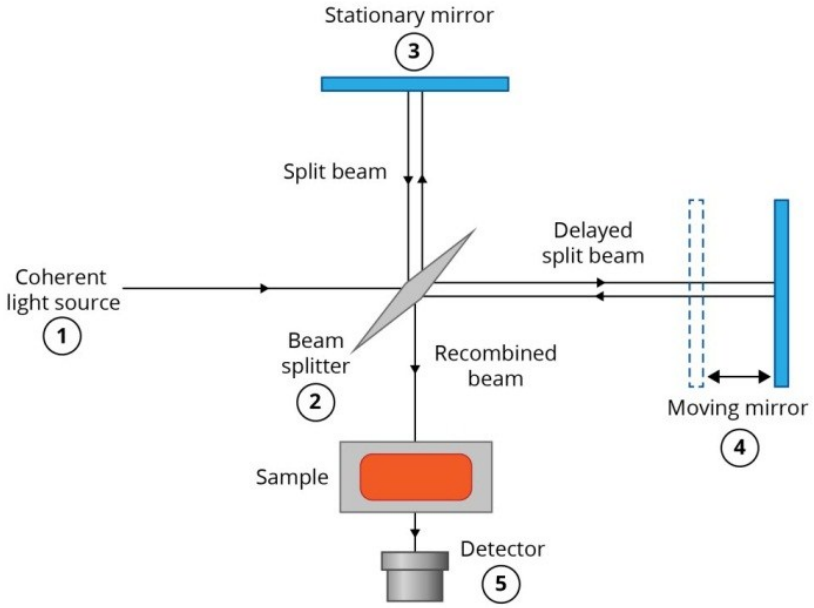


Figure 2.31: The schematic of Michaelson interferometer for FTIR interferometer [61].

Bunch length measurement with streak camera

Bunch length and longitudinal profile of the electron bunch are measured by a streak camera (SC) [62]. The SC is a time-resolved detector which enables bunch profile measurement by detecting the profile of the synchrotron radiation pulse emitted by the bunch. The components and basic schematic of the conventional SC is shown in Figure 2.32. The radiation generated by the electron bunch is a replica of the longitudinal profile of the bunch. In this way the bunch profile can be reconstructed from the time profile of the radiation. The synchrotron radiation first hits a photocathode where photons are converted into electrons inside the SC. The electrons are deflected in horizontal and vertical directions by parallel deflectors. Suitable time varying voltages are applied to the two electrodes, so that the electrons generated at the photocathode can be streaked, i.e. separated in angle and therefore in position at a downstream phosphor screen. The image on the phosphor screed is finally detected by a CCD camera. The voltage applied are usually two time varying harmonic signals with different frequencies providing a scan over two time ranges: a fast scan gives information in the ps time range and a slow time scale provides information in the μs time range. Commercially available SCs have a minimum resolution of about 1 ps, which is comparable to the bunch length that we want to measure. For this reason, a careful subtraction of the point spread function (PSF) is usually implemented in the post-processing of the images acquired during our experiments, in order to increase the accuracy of the measurements. The deconvolved image is fitted with a Gaussian and then the rms bunch length can be obtained in units of pixels which can be calibrated into time units like ps.

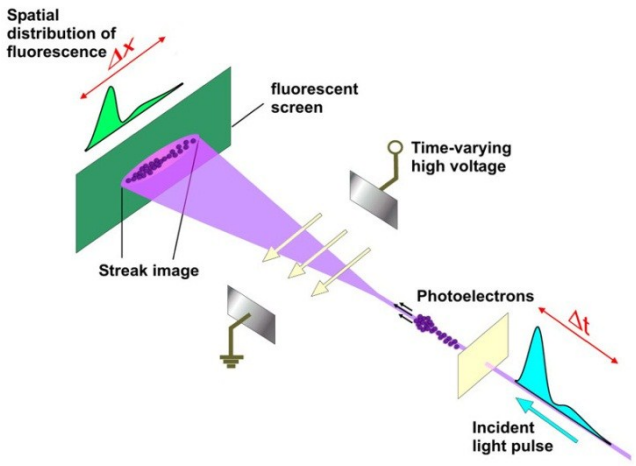


Figure 2.32: Basic configuration of the conventional streak camera [63].

2.4.2 Measurements of CSR generated from ultra-low alpha mode in Diamond storage ring

In December 2015, the ultra-low alpha mode was tested in the Diamond storage ring. The optics was tuned to deliver lattices with alpha values of -2×10^{-6} and -1×10^{-6} with machines parameters as listed in Table 2.2. Data were collected as a function of current with a streak camera for bunch length measurements and SBDs with different bandwidths for a partial assessment of the spectral distribution of the radiation emitted. In addition, data were taken from the Fourier transform infrared (FTIR) interferometer on the MIRIAM (Multimode InfraRed Imaging And Micro-spectroscopy) beamline B22 without any sample to measure spectrum of the coherent radiation from a pyroelectric detector.

Bunch length measurements with streak camera

A dual sweep streak camera from Optronis GmbH is used to measure the longitudinal profiles of electron bunches in picosecond scale. Images of time structure of synchrotron radiation are recorded directly by the streak camera. The images from the streak cameras are deconvolved with the PSF of 1.6 ps and 2D Gaussian fits are performed to get the bunch profile to evaluate the rms bunch length. Figure 2.33 shows the rms bunch

length as a function of the current stored in one bunch, from measurements with two values of alpha.

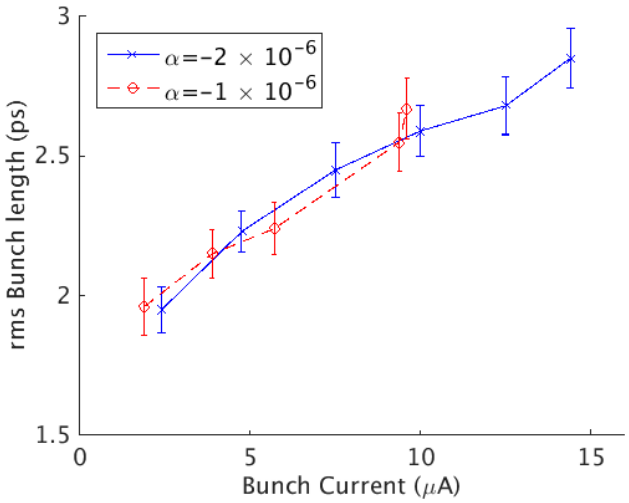


Figure 2.33: Measured rms bunch length of $\alpha = -2 \times 10^{-6}$ (blue, solid) and $\alpha = -1 \times 10^{-6}$ (red, dashed) from the streak camera.

It is evident that the difference in bunch length is not large; despite a factor √2 in bunch length should be expected according to Equation (2.5). It is plausible however that the contribution from the bunch lengthening with current has already washed out the difference between the two values and the bunch length is dominated by collective effects, in agreement with the simulation of Figure 2.23.

Spectrum measurements with Schottky barrier diodes

In order to detect radiation in a broad range, an array of eight SBDs is installed at the beamline B06 of Diamond storage ring. Each of the diodes covers specific frequency range as reported in Table 2.1. A total spectral range covering the frequency 33-1000 GHz can be measured. The time signals are detected by the diodes and the signals in the time domain are transformed into the frequency domain by Discrete Fourier Transform.

The spectrograms corresponding to $\alpha = -2 \times 10^{-6}$ and $\alpha = -1 \times 10^{-6}$ for different stored currents are shown in Figure 2.34 and 2.35, respectively.

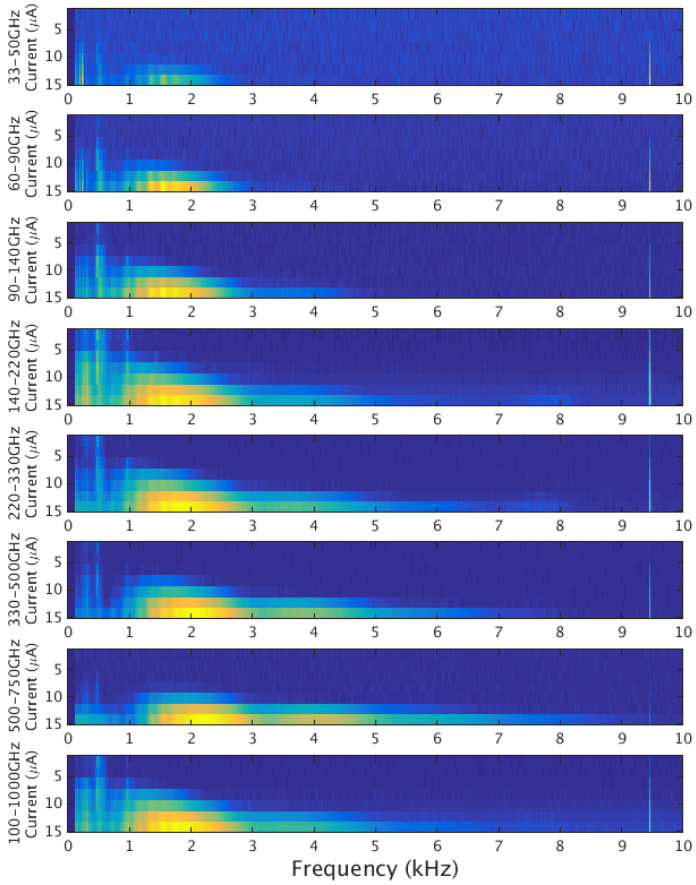


Figure 2.34: CSR spectrograms for $\alpha = -2 \times 10^{-6}$ measured with 8 SBD channels.

For $\alpha = -2 \times 10^{-6}$, the threshold current between steady state and bursting is ~8 μA and a broad bursting structure appears at ~1.5 kHz and then shifts to ~2 kHz with increasing bunch current. For $\alpha = -1 \times 10^{-6}$, the threshold current is ~6 μA and the bursting structure shifts from 1 kHz to ~1.5 kHz with higher bunch current. The bursting structures in both cases are rather broad. However, the frequency resolution of the measurement is relatively high as shown by the line close to 9.5 kHz, which is due to electronic noise in the measurements. The blurriness of the spectrograms can be consequences of multi-bunch fill pattern. In fact, the measurements were taken with 800 bunches and fluctuations of the arrival time or transverse position at the detector array of

the radiation emitted by each bunch possibly smear the spectrogram patterns. The spectrograms in Figure 2.34 and 2.35 should be compared with the corresponding spectrogram obtained with the *sbtrack* simulations in Figure 2.24 and 2.25, respectively. It is clear that only a qualitative agreement can extracted from these figure. We observe however that both spectrograms reveal a THz emission pattern with a broad excitation of frequencies above 1 kHz, extending up to 4 kHz as the current increases.

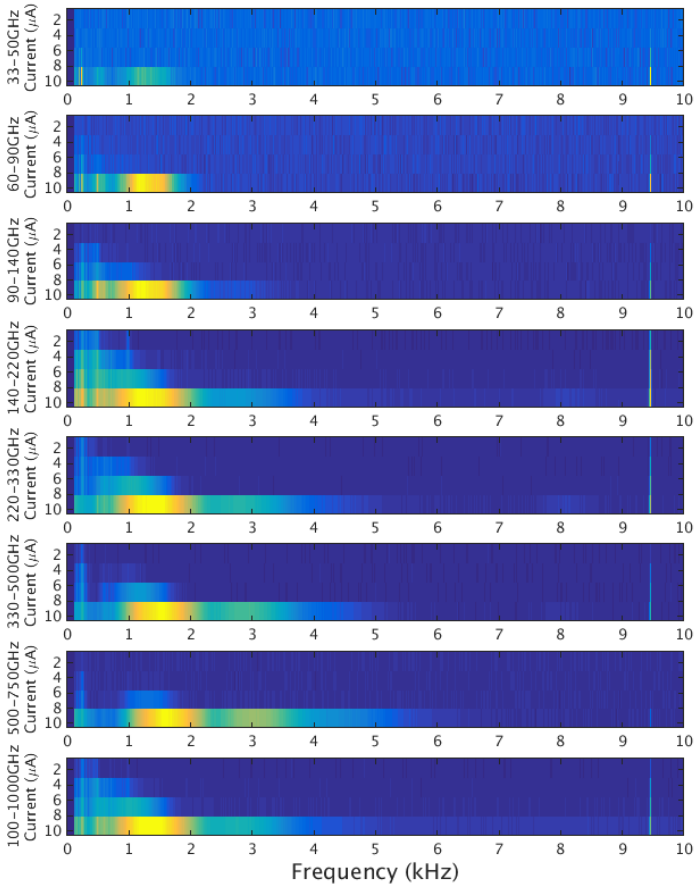


Figure 2.35: CSR spectrograms for $\alpha = -1 \times 10^{-6}$ measured with 8 SBD channels.

Spectrum measurements with FTIR interferometer

The FTIR interferometer on the MIRIAM beamline B22 was used at the same time during the ultra-low alpha experiments to investigate the spectrum of the synchrotron radiation from the short bunches. As we said, the acquisition time of one spectrum depends on the settings of the FTIR interferometer but usually covers many revolutions of the

electron bunches. Therefore, spectra measured with the FTIR are an average of radiation from many bunches.

The FTIR interferometer is a Bruker Vertex 80 V under vacuum used with resolution of 1 cm^{-1} and a 6-μm Mylar far-IR beam splitter with scanning velocity of 10 kHz in all experiments. The experiments were done in 100% transmission condition to detect directly characteristics of the CSR. Signals from the ISR are suppressed to the system noise floor by a broad spectrum attenuator. Data in form of FTIR interferograms were taken by a room temperature pyroelectric DLaTGS detector and processed with the software OPUS. The interferograms are transformed from spatial domain (length of the interferometer arms) into wavenumber domain. Each of two consecutive scans was taken within 50 seconds. Results are shown in Figure 2.36 and 2.37 for $\alpha = -2 \times 10^{-6}$ and -1×10^{-6}, respectively.

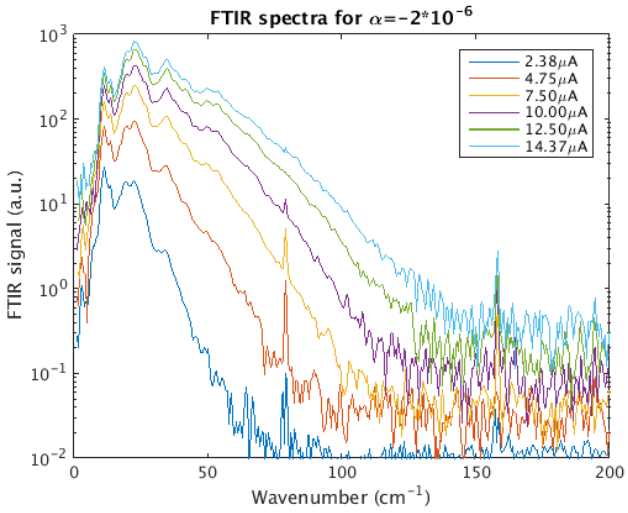


Figure 2.36: Spectra for $\alpha = -2 \times 10^{-6}$ measured with FTIR interferometer at different bunch current.

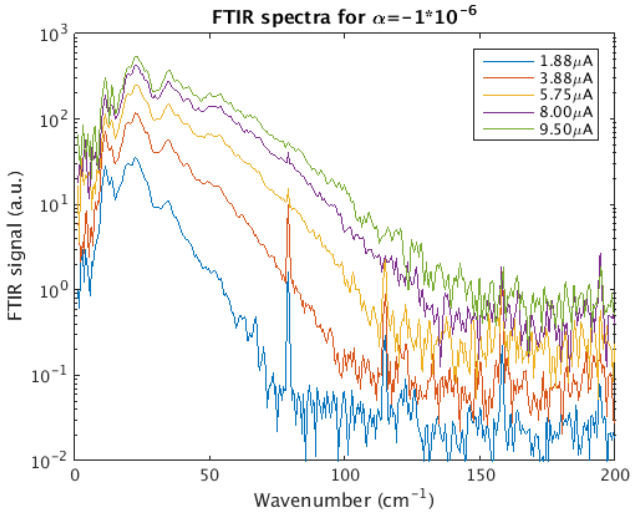


Figure 2.37: Spectra for $\alpha = -1 \times 10^{-6}$ measured with FTIR interferometer at different bunch current.

From the spectra we clearly see that the radiation emission is suppressed at low wavenumber (i.e. long wavelength, or low frequency). This is a result of shielding effect of the vacuum chamber which limits the observable wavelength below the shielding cut-off wavelength given as $\lambda_{cutoff} = 2\sqrt{\frac{h^3}{\rho}}$ from Equation (2.34). At B22, the chamber height is 32 mm and the bending radius is 7.1 m which give $\lambda_{cutoff} = 4.3\, mm$ or the wavenumber of 2.33 cm^{-1}. The drops of signals at wavenumber ~15 and ~30 cm^{-1} are potentially due to destructive interference of some internal reflections in the final windows of the beamline that acts as a Fabry-Perot interferometer. The peaks of noise also appear at harmonics of 80 cm^{-1}.

The threshold current is approximately 8 and 6 μA for $\alpha = -2 \times 10^{-6}$ and -1×10^{-6}, respectively. At these bunch current, 10% of the peak signal extends to cover wavenumber below 54 cm^{-1} for $\alpha = -2 \times 10^{-6}$ and 67 cm^{-1} for $\alpha = -1 \times 10^{-6}$. This shows that the limit frequency range of CSR emitted from short electron bunches in ultra-low alpha mode is pushed to about 1.6-2.0 THz.

The spectra obtained from two consecutive scans are used to evaluate signal-to-noise ratio (SNR). The rms signal-to-noise ratio (SNR) is the ratio of mean to standard deviation in each specific spectral range in 100% transmission lines. The 100% transmission lines, shown in Figure 2.38, are obtained by dividing two consecutive spectra from the FTIR measurements. In the frequency region where this line is close to 1 and less noisy, the source is highly reproducible and therefore has a good SNR, meaning that the source can be used effectively in these spectral regions.

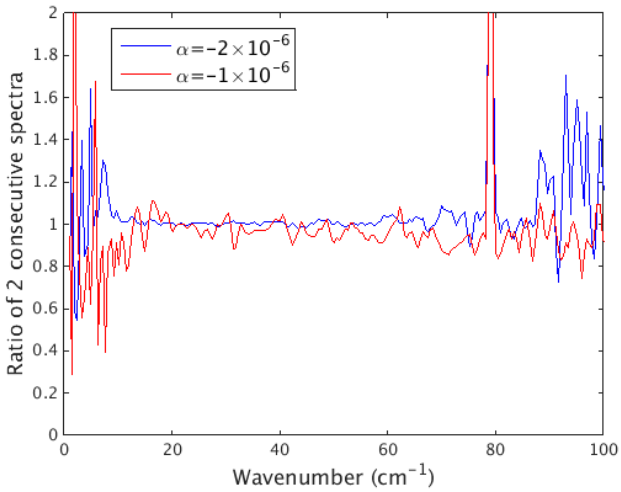


Figure 2.38: The 100% transmission lines for the ultra-low alpha experiments given by the ratio between two consecutive spectra for giving a measure of the SNR of the CSR source.

A quantitative measurement used to compare the spectral quality of a source is the SNR averaged over a given bandwidth. Table 2.4 reports these figures comparing the ultra-low alpha operating mode with the standard low alpha. The SNR data is the highest in the spectral range corresponding to the CSR-dominate range. However, the SNR of the ultra-low alpha modes is below the standard low alpha mode ($\alpha = -1 \times 10^{-5}$ and 400+1 filling pattern).

Table 2.4: FTIR signal-to-noise (SNR) ratios with sampling velocity 10 kHz.

Operating mode	rms SNR		
	10-40 cm^{-1}	40-80 cm^{-1}	10-80 cm^{-1}
Standard low alpha	210	7	8
$\alpha = -2 \times 10^{-6}$ (7.50 μA)	141	5	6
$\alpha = -1 \times 10^{-6}$ (5.75 μA)	16	3	3

2.5 Summary of comparisons of THz ultra-low alpha operating mode at Diamond storage ring

In this section, we compare the simulations performed with *sbtrack* with the experimental results in the ultra-low alpha mode in terms of bunch lengthening curves, spectrograms and spectra from FTIR.

2.5.1 Bunch lengthening

The machine parameters used in the simulation are reported in Table 2.3. The impedance model is the same reported in the previous paragraph and is based on shielded CSR, two BBR models (8.3 GHz and 100 GHz) and resistive wall. Comparisons of current-dependent bunch length obtained from the simulations and the measurements are shown in Figure 2.39 and 2.40. The bunch length from the simulations agrees with measurement at higher bunch current in both cases of alpha.

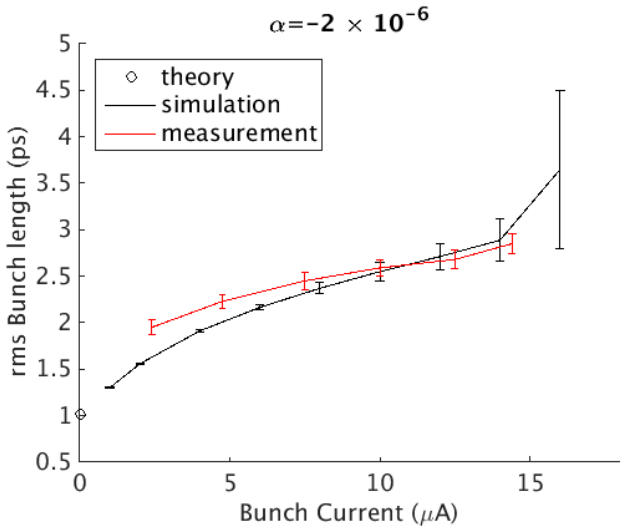


Figure 2.39: Comparison of rms bunch length between simulation and measurement for $\alpha = -2 \times 10^{-6}$.

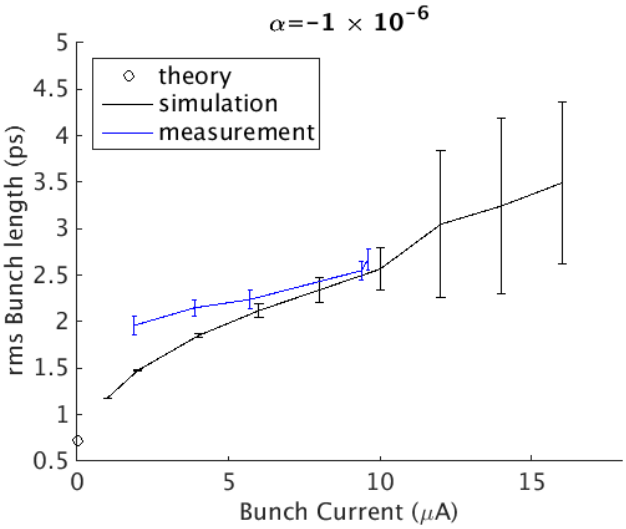


Figure 2.40: Comparison of rms bunch length between simulation and measurement for $\alpha = -1 \times 10^{-6}$.

Since the streak camera has limited resolution to measure bunch length especially at low bunch current, it is possible that the camera overestimate the bunch length at low current resulting in a clear mismatch of theoretical bunch length at zero current. The error bars of the simulations are large at high current because the bunch profile is more distorted by the wakefield which is stronger with the bunch current.

2.5.2 Spectrogram

For $\alpha = -2 \times 10^{-6}$, the simulated spectrogram in Figure 2.24 is in good qualitative agreement with the measured spectrograms in Figure 2.34. The bursting CSR begins at ~8 μA in both cases. The bursting structure covers a broad frequency but the whole bursting structure is at 0.5 kHz lower than the measurements.

For $\alpha = -1 \times 10^{-6}$, the agreement in the spectrogram between the simulations (Figure 2.25) and the measurements (Figure 2.35) is less clear. The bursting CSR begins at ~8 μA in the simulation, whereas it is at ~6 μA in the measurement. The simulated bursting structure covers narrower frequency range than the measured results. However, the second peak is visible in the measured spectrogram (Figure 2.35), especially in the bandwidth 500-750 GHz. This shows that the measurements consistent with the simulations.

A plausible explanation could be that the *sbtrack* simulations are done based on single bunch model, whilst the measurements were taken from 800 bunches filling pattern. This is a plausible source of sharper bursting peak in the simulations.

2.5.3 FTIR spectrum

The spectrum of the coherent THz radiation is obtained from the form factor of the simulations. Figure 2.41 and 2.42 show comparisons of spectra in both alpha values and the spectra measured with the FTIR interferometer. The FTIR taken data with arbitrary unit so the simulated spectra are scaled down to fit noise level at high wavenumber.

Good qualitative agreement was found in the form factors, especially for the case of $\alpha = -1 \times 10^{-6}$ the data fit very well from the wavenumber of 40 cm^{-1}.

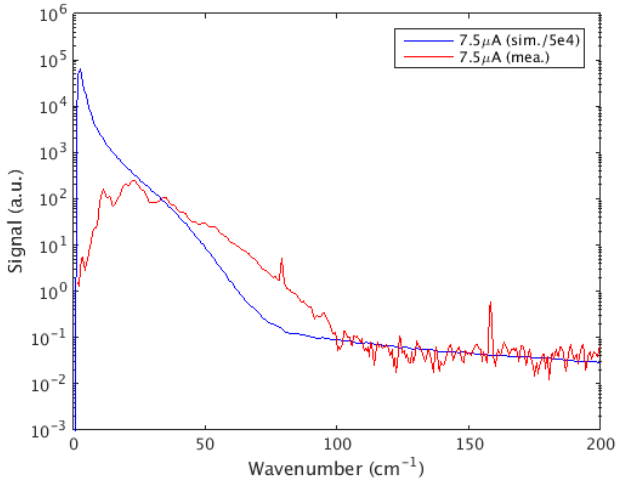


Figure 2.41: Comparison between measured and simulated spectra for $\alpha = -2 \times 10^{-6}$ at 7.5 μA.

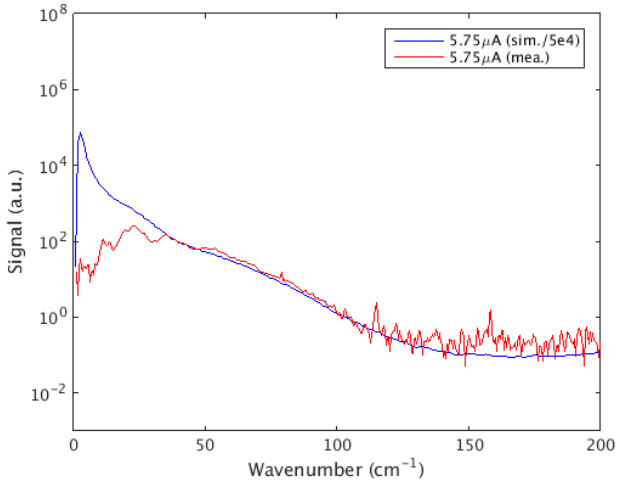


Figure 2.42: Comparison between measured and simulated spectra for $\alpha = -1 \times 10^{-6}$ at 5.75 μA.

2.6 Summary

Short pulses of high intensity THz radiation can be generated in storage rings in special dedicated operating mode with low negative momentum compaction factor. This operating mode shortens the equilibrium bunch length in the storage ring thereby broadening the spectral range of CSR into THz.

A major problem of the low-alpha lattices is the sensitivity to collective instabilities which force a substantial reduction of the stored current. It is therefore important to study the beam dynamics using realistic wakefields, including CSR and the best available model for the vacuum pipe impedance. The code *sbtrack* was used to perform particle tracking of a single bunch with the impedance models of resistive wall, BBR and CSR with shielding to investigate beam dynamics in the ultra-low alpha operating mode.

In view of extending the capabilities of Diamond as a source of THz radiation a new operating mode was proposed by exploring an ultimate reduction of the momentum compaction factor that can be tolerated for machine operation. Experiments of ultra-low alpha mode were conducted at Diamond storage ring. The bunch length was measured with a streak camera and turn-by-turn spectral data of CSR were taken with SBDs with different bandwidths. FTIR interferometer on the beamline B22 was also used simultaneously to measure average spectral distributions of the CSR. The CSR frequency range can be pushed to cover higher frequency from far IR to THz range but the SNR need to be improved further in order to make the ultra-low alpha mode suitable for direct use in spectroscopy.

The simulations and the measurements are in reasonably good agreements in terms of bunch lengthening, threshold current, bursting structures in the SBD spectrograms and FTIR spectra.

Chapter 3

THz Radiation and Short Pulses with an RF Linac

Electron RF linacs have the potential of producing high quality electron beams with short bunches and small beam emittance which can be used for driving short pulse radiation sources. When an electron beam generated by a linac is sent through a bending magnet or through an undulator it emits synchrotron radiation according to the principles and the characteristics described in Chapter 1. In normal conditions the radiation pulse length corresponds to the electron bunch length, therefore an obvious way of generating short radiation pulses is that of shortening the electron bunch length as much as feasible. Magnetic bunch compression is commonly used in linacs to shorten the electron bunch length to produce short pulse radiation but also to emit coherent radiation at wavelength longer than the bunch length. In this way it is clear that short-pulses high power THz radiation can be generated with the RF linacs.

Coherent THz radiation generated by electrons from RF linac in a bending magnet generates a broadband spectrum and can be manipulated to cover THz spectral range by reducing the electron bunch length. Another method to produce short pulses of high power THz radiation is to drive FEL in an undulator with short electron bunches. The FEL provides high power radiation at a specific resonance frequency Equation (1.26) related to the beam energy and the undulator parameter.

In this chapter we focussed on design of a linac-based compact THz source based on CSR from bending magnets and SASE FEL from undulators as they are the simplest

processes that can guarantee high pulse power and short time durations. The choice of the main parameters and the emphasis of the study are on the possible installation of such sources in the Accelerator Science Laboratory (ASL) under discussion in Oxford, further described in Chapter 5. This is of course a template for the installation of similar machines in any small to medium scale laboratory.

The RF linac considered is driven by a photoinjector gun, S-band cavities for acceleration and a magnetic bunch compression system. The beam dynamics is studied and optimised by means of start-to-end simulations done with state-of-the-art numerical codes describing the beam dynamics in presence of collective effects such a space charge at low energy, wakefields and coherent synchrotron radiation. The emission of radiation from the electron bunch as CSR from bending magnets and as FEL radiation from the undulators is evaluated. Both configurations (bending radiator and FEL) are based on the same linac design: photoinjector, S-band cavity and bunch compressor, with minimal hardware changes. The CSR source uses the last bending magnet as radiator and the radiation was estimated with analytical equations, whilst the SASE FEL source was simulated with the 3D numerical code GENESIS.

3.1 RF linac driven THz radiation source

In order to generate radiation in THz frequency range with a compact linac-based source in the ASL, the first analysis should address the energy required for the electron beam. The synchrotron radiation is broadband and THz emission will rely on the coherent enhancement associated to the short bunch length. In the FEL instead the energy of the electron is dictated by Equation (1.26). Assuming standard permanent magnet undulator technology ($\lambda_u = 35\ mm, K = 2.06$), we conclude that an energy of below 100 MeV would be perfectly sufficient to reach THz and FIR radiation wavelengths. An example of

such a compact linac-based THz source is a project called FLUTE [27] driven by a 41 MeV linac. The layout is shown in Figure 3.1 and fits in a total length of 15 m.

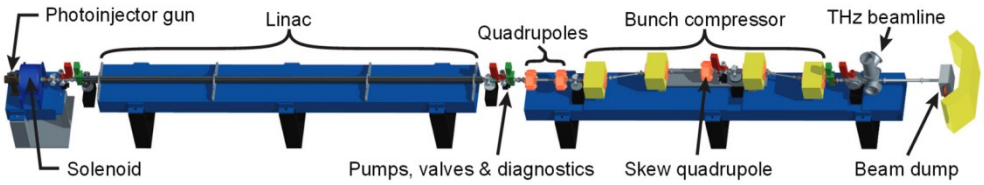


Figure 3.1: Schematic layout of a linac based THz source (FLUTE) [27].

Typically, a linac-based radiation source consists of three main components: (1) a photoinjector including photocathode RF gun for generating an electron beam, (2) an RF linac for accelerating the beam to the target beam energy, and (3) a radiation generator which can be either a dipole bending magnet or an undulator for producing radiation from electron beams. The electron beams generated from a photoinjector are naturally very short, with the bunch duration ranging from few tens of ps down to few ps. This allows the generation of short-pulse radiation necessary for advanced experimental techniques such as pump-probe measurement. In order to further shorten the electron bunch, a bunch compressor is included after the RF linac and prior to the radiation generator for controlling the electron bunch length.

To optimise the design of the linac-based radiation source and examine its potential as a THz source, we performed a series of start-to-end simulation splitting the linac in different portions, consisting of

- electron beam generation in a photoinjector,
- beam acceleration in a linac,
- bunch compression in a magnetic chicane, and
- generation of radiation from a bending magnet or an undulator.

The start-to-end simulation requires multiple numerical codes for investigating the beam dynamics because each region of the source is dominated by different physical effects. For instance, the beam dynamics in the photoinjector at low beam energy is dominated by space charge effects while these effects become progressively weaker as the energy increases: this part is simulated with the code ASTRA [64]. On the other hand, the effects related to the CSR are relevant only in the last part of the linac in the bunch compressor: this part is simulated with the code Elegant [46]. The emission of radiation in the undulator is simulated with the code GENESIS [39]. Figure 3.2 shows how the start-to-end simulation has been split in different codes for different components of the machine.

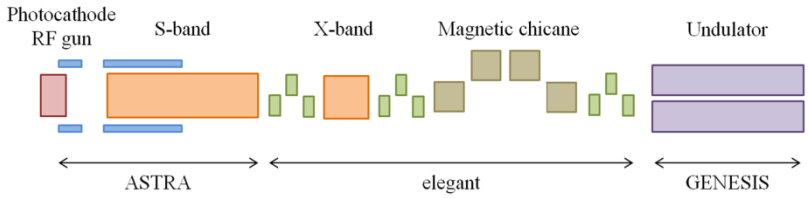


Figure 3.2: Layout of a compact linac-based THz source with three simulation regions. Simulation in each region is performed with the indicated numerical codes. Blue and green components are solenoids and quadrupole triplets, respectively.

Details and specific physics in each region are discussed further in the following sections.

3.2 Accelerator physics in linac-based sources

3.2.1 Beam generation

Electron beam generation in our design occurs in the first region consisting of photoinjector and RF booster linac, called beam injector. The electrons are produced from the photoelectric effect of an intense laser pulse hitting the cathode and accelerated in a RF

field. Since electrons are accelerated from rest in this region, dynamics of electrons at low energy dominates by space charge effects.

Space charge effects

Space charge forces are generated directly by the charge distribution of electrons in the bunch through Coulomb interactions. These direct space charge forces mainly affect transverse beam dynamics leading to beam instabilities generating strong distortions in the transverse phase space distribution and increasing the rms beam emittance. The main variables which characterise the transverse beam dynamics are the rms envelope $\sigma = \sqrt{\langle x^2 \rangle}$ and transverse normalised rms emittance. At the cathode source the minimum emittance that can be generated by a photoinjector is given by the so-called thermal emittance [65]

$$\varepsilon_{n,th}^2 = \frac{\langle x^2 \rangle \langle p_x^2 \rangle}{(m_0 c)^2} = \frac{\gamma k_B T \sigma_0^2}{m_0 c^2}, \tag{3.1}$$

The theory of space charge dominated beam has been substantially developed in the last two decades to treat the beam dynamics in split photoinjectors [66]. While in general space charge forces can generate emittance growth, for some particular bunch distribution the space charge forces are linear and their effect on the emittance growth can be compensated using solenoids. This is the principle of the so-called "emittance compensation" mode, that has been used as a guideline for the optimisation of many photoinjectors in the past [67] and that we are going to describe. The rms envelope equation for an axisymmetric beam evolves in the linac structures as [65]

$$\sigma'' + \frac{\gamma'}{\gamma}\sigma' + k_{ext}^2 \sigma = \frac{\hat{I}}{2 I_A \gamma^3 \sigma} + \frac{\varepsilon_{n,th}^2}{\gamma^2 \sigma^3} \tag{3.2}$$

where $\hat{I}$ is the peak current and I_A is the Alfven current (~17 kA), and $\gamma' = eE_{acc}/mc^2$, in which E_{acc} is the accelerating field. The first term is the change in the envelope slope, the second term describes the envelope oscillation damping due to acceleration, the third term

accounts for the linear external focus forces with the strength k_{ext}, the fourth term describes the defocussing space charge effects, and the fifth term associates with the internal pressure due to the emittance.

From the rms envelope in Equation (3.2), there are two beam propagation regimes: space charge dominated and emittance dominated. The regime of the beam dynamics is determined by the ratio between the space charge term and the emittance term which is defined as the laminarity parameter

$$\rho = \frac{\hat{I}}{2I_A\gamma}\frac{\sigma^2}{\varepsilon_n^2}. \tag{3.3}$$

When $\rho \ll 1$, the emittance pressure dominates and the space charge effects are negligible. When $\rho \gg 1$, the beam is space charge dominated and electrons evolves with a laminar flow. In this regime, correlated emittance growth normally occurs but it can be controlled conveniently with proper beam matching conditions (described below). As charges are concentrated at centre slice more than head and tail slices, the radial space charge at the centre slice is stronger and therefore the transverse momentum or divergence at the centre slice is higher than at the head and tail. A multi-slice approach is used to describe the beam dynamics. Naming the bunch longitudinal coordinate ζ, the bunch can be represented by a train of longitudinal slices of the envelope $\sigma_s(z,\zeta)$. Equation (3.2) can still describe the evolution of each slice by using slice parameters $(\gamma_s, \gamma_s', k_{sc,s} = k_{sc}g(\zeta))$. From the solutions of the envelope equation in each slice, the correlated normalised rms emittance is defined as

$$\varepsilon_{n,rms,cor} = \langle\gamma\rangle\sqrt{\left(\langle\sigma_s^2\rangle\langle\sigma_s'^2\rangle - \langle\sigma_s\sigma_s'\rangle^2\right)}. \tag{3.4}$$

This correlated emittance and the thermal emittance in Equation (3.1) treated as the uncorrelated emittance are used to determine the total normalised rms emittance by

$$\varepsilon_{n,rms} = \sqrt{\left(\varepsilon_{n,th}^2 + \varepsilon_{n,rms,cor}^2\right)}. \quad (3.5)$$

The correlated emittance is increased mainly due to the mismatch of the longitudinal bunch slices. The longitudinal slices need to be matched with the external focussing from a component like a solenoid.

Under the emittance compensation, the oscillations of the emittance induced by linear space charge effects are damped by aligning the orientation of the transverse phase space ellipses (each ellipse represents the phase space of each bunch slice) to be matched in the phase space. The concept is further explained in Figure 3.3. The electron bunch emitted from the cathode has small thermal emittance as shown in Figure 3.3 (top left). When it travels in between the cathode to the solenoid, the space charge takes action by rotating the transverse phase space anticlockwise as shown in Figure 3.3 (top middle). Due to the higher charge density at the centre slice than at head and tail, the radial space charge at the centre slice is stronger which makes the beam divergence at centre higher than the divergence at head and tail. When the electron bunch arrives at the solenoid, the solenoid field focusses the beam resulting in the clockwise phase space rotation in Figure 3.3 (top right). After the bunch passing the solenoid, the space charge force dominates again and can rotate the phase space anticlockwise as shown in Figure 3.3 (bottom left).

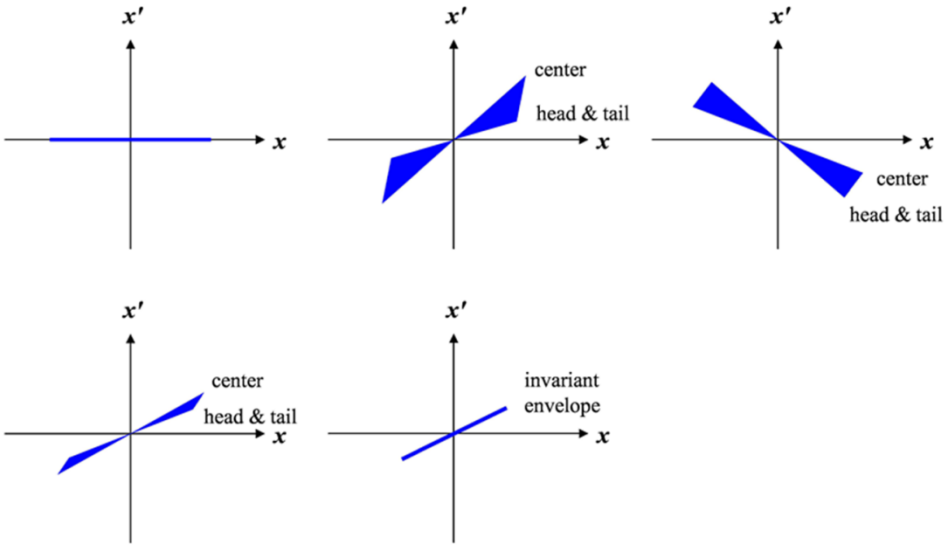


Figure 3.3: Emittance compensation scheme [68]. (Top left) Initial transverse phase space at the cathode has small thermal emittance, (top middle) the phase space rotates anticlockwise due to space charge force at the region between the cathode and the solenoid, (top right) the solenoid provides the focussing field which rotates the phase space clockwise, (bottom left) after drifting from the solenoid the space charge force re-acts and forces the phase space rotating anticlockwise again, and (bottom middle) phase space ellipses are aligned around the invariant envelop at the end of the booster linac.

This matching condition is known as invariant envelope condition. The phase space aligned following the invariant envelope is illustrated in Figure 3.3 (bottom middle). To achieve this, a solenoid is placed next to the electron gun for focussing and control the position of a beam waist. The RF booster linac is placed at the position of the beam waist [69] and accelerating gradient of the booster need to satisfy the condition [70]

$$\gamma' = \frac{2}{\sigma_w}\sqrt{\frac{\hat{I}}{2I_A\gamma}} \tag{3.6}$$

where σ_w is the beam size at the beam waist. Since the emittance oscillations are not damped in drift space, the beam needs to be accelerated at its first emittance minimum in

order to avoid the emittance oscillation turning into the irreversible thermal-like emittance growth by nonlinearities. As the acceleration proceeds further in the linac, the emittance oscillations are damped and the geometric emittance is further reduced due to the adiabatic damping with energy increase.

3.2.2 Bunch compression

The electron bunch length from the photoinjector depends on the charge extracted by the laser pulse, and it is therefore defined by the laser pulse length and by the possible lengthening due to space charge. In the case of RF linac-based sources the charge required to drive a powerful radiation source is in the order of few hundreds pC, and in such cases the bunch length cannot be shorter than several ps due to space charge emittance blow up and bunch lengthening. In order to generate high peak power short pulse THz radiation by dipole radiation or FEL it would be beneficial to investigate the possibility of longitudinal bunch compression in our designs.

The bunch compression can be accomplished with a magnetic compression system. Such system provides shorter (longer) path length for higher (lower) energy electrons. The most commonly used bunch compressor is a magnetic chicane consisting of a set of dipole magnets. The simplest chicane requires four dipoles arranged in C shape as known as C-type or 4-bend magnetic chicane with the schematic shown in Figure 3.4.

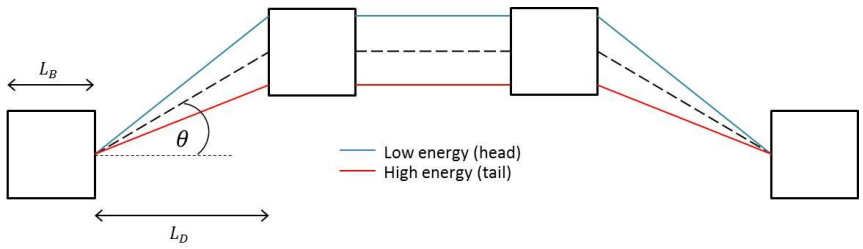


Figure 3.4: 4-bend magnetic chicane for longitudinal bunch compression.

The longitudinal coordinate (z) of an electron with respect to the bunch centre after passing the bunch compressor is a function of the relative energy deviation (δ) expressed by

$$z_f(\delta) = z_i + R_{56}\delta + T_{566}\delta^2 + U_{5666}\delta^3 + \cdots \tag{3.7}$$

where z_i is the initial coordinate and R, T, and U are the first, the second and the third order transfer matrices of the compressor. Note that R_{56} is the first-order momentum compaction factor which is equivalent to α_c or alpha in storage rings. The value of R_{56} depends on the specific configuration of the compressor. The value of R_{56} of the 4-bend chicane is

$$R_{56} = -\left[4L_B\left(\frac{sin\theta}{\theta} - cos\theta\right) + 2L_D\theta sin\theta\right] \tag{3.8}$$

or in the limit of $\theta \ll 1$,

$$R_{56} \approx -2\theta^2\left(L_D + \frac{2}{3}L_B\right). \tag{3.9}$$

The nonlinear term can be estimated with the first-order term as $T_{566} \approx -\frac{3}{2}R_{56}$ and $U_{5666} \approx 2R_{56}$.

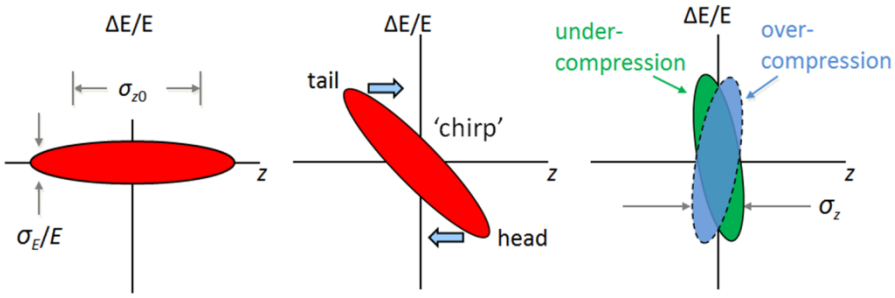


Figure 3.5: Schematic of bunch compression. (Left) the initial longitudinal phase space before acceleration by the RF cavity, (middle) the phase space after going through the RF cavity with off-crest phase introducing the energy chirp, (right) the phase space after the bunch compressor shown in under-compression and over-compression schemes.

In order for the compression to happen the incoming bunch must have a correlation between its energy and the longitudinal position as shown in Figure 3.5.

After the RF cavity, the energy deviation of any electron is also a function of the longitudinal position given by

$$\delta(z) = \delta_i \frac{E_i}{E_f} + h_1 z + h_2 z^2 + O(z^3) \tag{3.10}$$

where δ_i is the uncorrelated relative energy deviation given by the beam emission at the cathode, E_i and E_f are the energy before and after RF acceleration, and h_1 and h_2 are the first and second order longitudinal energy correlation, also called "energy chirp", introduced by the RF accelerating field when the RF linac is operated with off-crest RF phase ($\phi_{RF} \neq 0$). The energy chirp is given by

$$h_1 = \frac{2\pi e V_0}{\lambda E_f} \sin \phi_{RF} \tag{3.11}$$

$$h_2 = \frac{2\pi^2 e V_0}{\lambda^2 E_f} \cos \phi_{RF} \tag{3.12}$$

here V_0 is the on-crest RF voltage, λ is the RF wavelength and ϕ_{RF} is the RF phase.

To first order, the final longitudinal coordinate can be expressed from Equation (3.7) and (3.10) as

$$z_f = \frac{E_i}{E_f} R_{56} \delta_i + (1 + h_1 R_{56}) z_i \tag{3.13}$$

The final rms bunch length at the end of the compression system can be expressed as a function of the initial rms bunch length of σ_{z_i}, initial uncorrelated rms energy spread of σ_E as

$$\sigma_{z_f} = \sqrt{\frac{E_i^2}{E_f^2} R_{56}^2 \sigma_E^2 + (1 + h_1 R_{56})^2 \sigma_{z_i}^2}\,. \tag{3.14}$$

From Equation (3.14), if the chirp is created to fulfil the condition $1 + h_1 R_{56} = 0$, the bunch length achieves full compression at the end of the chicane. In the case $1 + h_1 R_{56} > 0$, we have under-compression, while $1 + h_1 R_{56} < 0$ we have over-compression. In this way, the acceleration with off-crest phase in the RF linac makes the head of the bunch has lower energy than the tail. As the bunch traverses across the magnetic bunch compressor, the tail follows the shorter path length and the electrons at the tail can catch up with the ones at the head. As a result, the bunch length is shortened at the end of the compression system.

In the second-order approximation, the final longitudinal coordinate is given by

$$z_f = \frac{E_i}{E_f} R_{56} \delta_i + (1 + h_1 R_{56}) z_i + (R_{56} h_2 + T_{566} h_1^2) z_i^2 \tag{3.15}$$

which shows that the bunch length can be further minimised by having the energy chirp satisfies another condition of $R_{56} h_2 + T_{566} h_1^2 = 0$. This second-order term can be compensated by a harmonic cavity located in between the RF linac and the bunch compressor, and set at the decelerating phase (i.e. $\phi_n = \pi$) with the harmonic RF voltage (V_n) of

$$eV_n \approx \frac{E_f \left[1 - \frac{\lambda^2}{2\pi^2} \frac{T_{566}}{R_{566}^3} \left(1 - \frac{\sigma_{z_f}}{\sigma_{z_i}}\right)^2\right] - E_i}{n^2 - 1} \tag{3.16}$$

where E_f is now the beam energy after passing the harmonic cavity and the harmonic number is $n = \lambda/\lambda_n$. The role of the harmonic cavity is to linearise the longitudinal phase space to avoid charges to be concentrated in a sharp temporal spike that will enhance the CSR effects leading to blowout of the transverse emittance.

Emittance growth from coherent synchrotron radiation

When the electrons pass through each dipole in the bunch compressor, they generate synchrotron radiation. Photons emitted by the electrons at the bunch tail can catch up with the electrons at the head and the electromagnetic fields of the photons then interacts with the head resulting in transverse emittance growth, especially in the horizontal plane. Eventually, the beam quality can be detrimentally affected thereby reducing the intensity of the coherent radiation at the end of the linac. If the bunch is still long as in the first and the second dipoles, synchrotron radiation will be incoherent and hence have small effect on the beam. However, as the bunch is shorter in the third dipole and is finally shortest in the last dipole, the electrons in the bunch emit CSR. The strong fields of the CSR induced significant increase in the transverse emittance [71].

The rms relative energy spread due to CSR kick in a dipole magnet of length L_B and bending radius ρ is given by [72]

$$\sigma_{\delta,CSR} = 0.2459 \frac{r_e Q L_B}{e\gamma \rho^{2/3} \sigma_z^{4/3}} \tag{3.17}$$

clearly displaying that the CSR effects depend on the bunch length as $\sigma_z^{-4/3}$. We also see that the critical location for the effect of CSR is at the fourth bending magnet where the bunch length is the shortest. In the single-kick approximation in a short magnet, the rms projected emittance in the bending plane (horizontal) after the CSR kick is [73]

$$\varepsilon \approx \varepsilon_0 \sqrt{1 + \frac{H}{\varepsilon_0} \sigma_{\delta,CSR}^2}. \tag{3.18}$$

where ε_0 is the initial rms horizontal emittance before the kick, the *H*-function is defined by $H = \gamma\eta^2 + 2\alpha\eta\eta' + \beta\eta'^2$ where α, β and γ are Twiss parameters and η' is the derivative of dispersion function with respect to the longitudinal coordinate. Assuming that beam

waist ($\alpha = 0$) is at the entrance of the 4th dipole where $\eta = 0$ and small bending angle $\eta' \approx \theta$, the CSR induced emittance growth is expressed by

$$\Delta\varepsilon \approx \frac{\beta\theta^2\sigma_{\delta,CSR}^2}{2}. \tag{3.19}$$

This relation emphasises that the emittance growth can be strongly reduced by minimising the beta function at the fourth bending magnet. This is a condition on the linear optics that will be enforced in the design of the bunch compressor.

3.2.3 Radiation generation

The last region of our THz source design is the region for evaluation of radiation generation. As discussed in Chapter 1, the radiation from the linac-based THz source can be generated mainly from dipole bending magnet and undulator. Synchrotron radiation with broad spectrum can be obtained from the bending radiation, while FEL from the undulator provides much narrower spectrum. Both were studied and will be presented later in the following sections to investigate potentials of the THz source for operating with both radiation generation methods.

3.3 Start-to-End Simulations

The designs of the THz radiation source were done with start-to-end simulation which is split into three main regions as shown previously in Figure 3.2. The linac hardware was designed in order to be compatible with two operating modes: one driving the THz source from CSR in the last dipole of the bunch compressor and one to drive a SASE FEL from an undulator.

3.3.1 THz FEL

The layout of this design follows Figure 3.2. The start-to-end simulations were done in three regions with three different numerical codes. Simulated results for each region are presented as following.

Beam generation simulations

The initial part of the RF linac is the RF photocathode gun where the dynamics is strongly dominated by space charge. A state-of-the-art code used to consider these effect is ASTRA [64]. The main components of this region are a photoinjector which is a 1.6-cell type RF gun based on the SLAC/BNL design [74] with expected repetition rate up to 100 Hz and a booster linac which is an 86-cell travelling wave RF cavity. Both are operated at S-band (2.856 GHz) frequency. Two solenoids are used for controlling transverse beam size. One is located at the photoinjector (solenoid 1) for controlling the position of beam waist and the other is at the booster linac (solenoid 2) for focussing the beam along the booster linac. The layout of this region is illustrated in Figure 3.6.

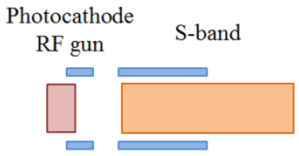


Figure 3.6: Components in the injector simulation region. Solenoids are illustrated in blue.

An initial electron bunch is assumed to be generated by a laser pulse at a photocathode RF gun and particle tracking was done with ASTRA from the gun to the end of a booster linac. The laser beam distribution at the cathode is chosen to be a uniform (flat-top) distribution in time domain as it can reduce the emittance growth due to space charge better than the Gaussian distribution laser pulse at the cathode [75][76]. Laser and beam parameters at the cathode are listed in Table 3.1. Phase space and distribution in transverse

and longitudinal plane at the cathode are shown in Figure 3.7 and 3.8, respectively. A long laser pulse gives small emittance but low peak current which results in low radiation power, while short laser pulse can generate high peak current but large emittance leading to low brightness. We used the laser pulse length of 6 ps as a good compromise for a 500 pC bunch in terms of emittance preservation and peak current.

Table 3.1: Laser beam parameters at the cathode of the photoinjector for THz FEL design.

Parameter	Value
Laser pulse length	6.0 ps (flat-top)
Rise/fall time	0.8 ps
Longitudinal energy distribution	Isotropic
Energy distribution width	1.1 eV
Transverse momentum distribution	Radial uniform
Transverse rms laser beam size	0.3 mm
Bunch charge	500 pC

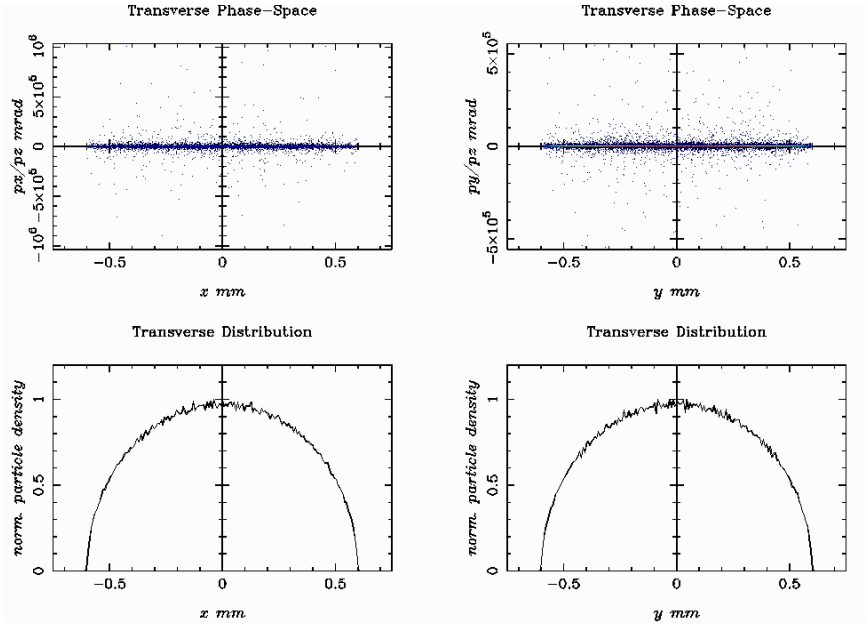


Figure 3.7: Transverse phase space (top) and distribution (bottom) at the cathode.

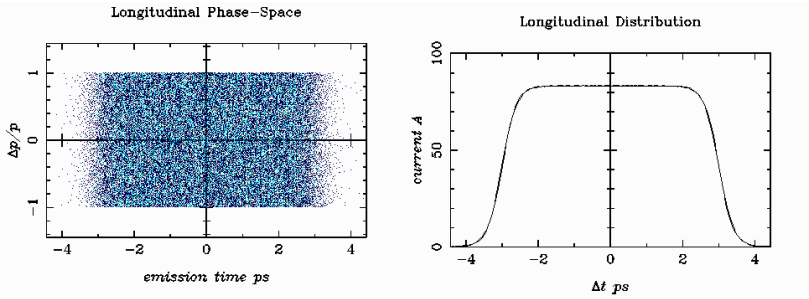


Figure 3.8: Longitudinal phase space (left) and distribution (right) at the cathode

The first optimisation for the beam generation region is to locate the beam waist within 1.5 m from the cathode in order to maintain a compact design feasible to fit in the limited space for the ASL project while maintaining good electron beam qualities. The parameters used in the optimisation are phase of the RF gun, the maximum magnetic field and position of solenoid 1 to achieve a minimum beam transverse beam size within 1.5 m. From the exploration of the machine parameters with ASTRA, we found the beam waist at 1.435 m with the parameters shown in Table 3.2.

Table 3.2: Parameters for locating a beam waist at 1.435 m from the cathode.

Parameter	Value
Maximum longitudinal electric field of RF gun	120.2 MV/m
Phase of electric field of RF gun	-3.939°
Maximum magnetic field of solenoid 1	0.2797 T
Position of solenoid 1	0.1890 m

The entrance of the booster linac is placed at the beam waist position for the emittance compensation process. The booster is used to accelerate the beam off-crest for creating the energy chirp in the longitudinal bunch distribution which is essential for the bunch compression in the following part of simulations. The optimisation was done for getting low normalised beam emittance at the end of the booster linac by scanning phase of

the booster linac, maximum magnetic field and position of solenoid 2. Table 3.3 shows parameters from this optimisation.

Table 3.3: Optimised parameters of booster linac and solenoid 2 for THz FEL design.

Parameter	Value
Maximum longitudinal electric field of booster linac	7 MV/m
Phase of the electric field of booster linac	-27.22°
Maximum magnetic field of solenoid 2	-0.1338 T
Position of solenoid 2	1.986 m
Beam energy at the end of booster linac	19.76 MeV
Normalised emittance at the end of booster linac	0.98 μm·rad
Beam size at the end of booster linac	0.51 mm
rms energy spread	1.04 %

The accelerating gradient used, 7 MV/m, is much lower than the accelerating gradient from Equation (3.6) which predicts about 70 MV/m. We used this parameter for maintaining the final beam energy below 20 MeV, so that the FEL resonance wavelength is in THz range. For instance, the beam energy for producing radiation at the resonance frequency of 5 THz (60 μm) with an undulator of the undulator parameter $K \approx 2$ and the undulator period $\lambda_u = 3.5\,cm$ is about 15 MeV. The relation between FEL resonance wavelength λ_r and relativistic factor γ for different undulator parameters is shown in Figure 3.9. Despite the choice of a lower accelerating gradient the final emittance is still below 1 μm·rad.

The normalised transverse emittance and the beam size along the injector region are shown in Figure 3.10. The effects of space charge, however, are not negligible when operating with beam energy below 100 MeV. The space charge effects limit the achievable emittance after the emittance compensation in the booster linac. This appears as an increase

of the emittance after 1.5 m following by a damping of the emittance in the linac shown in Figure 3.10 (left).

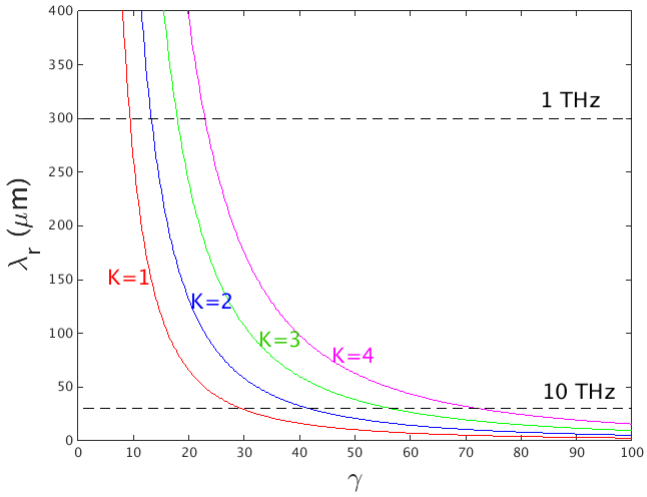


Figure 3.9: Dependence of FEL resonance wavelength λ_r on relativistic factor γ at different undulator parameter K.

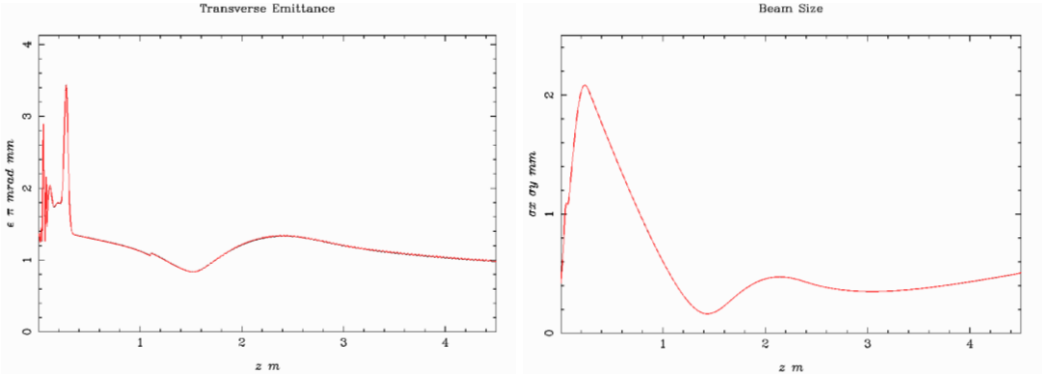


Figure 3.10: Normalised transverse emittance (left) and transverse beam size (right) along the injector region.

The transverse phase spaces plots in Figure 3.11 and the slice ellipses in Figure 3.12 show that the bunch slices are not perfectly aligned and a transverse halo is still present, increasing the transverse emittance. The projected normalised emittance is about 1 μm·rad, but the slice emittance shown in Figure 3.12 is below 0.7 μm·rad on a substantial part of the beam longitudinal profile. It is clear that smaller emittance could be achieve by reducing

the charge the value achieved is already sufficient to remain under the diffraction limit for THz radiation ($\varepsilon < \lambda/4\pi$).

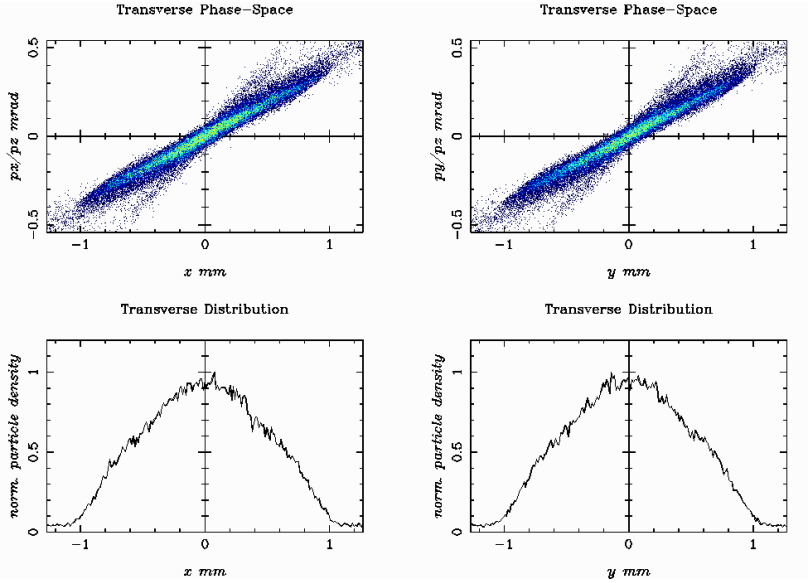


Figure 3.11: Horizontal (left) and vertical (right) phase space (top) and distribution (bottom) at the end of the booster linac.

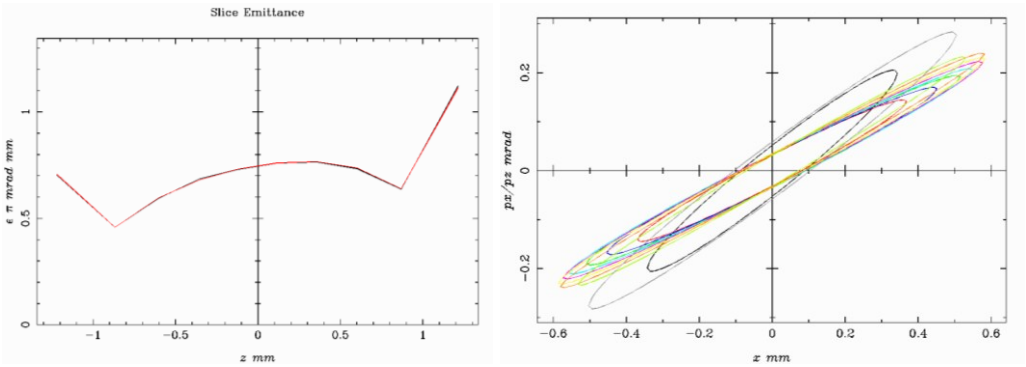


Figure 3.12: Slice emittance of slices along the bunch (left) and slice ellipses in horizontal phase space (right) at the end of the booster linac. Each ellipse represents each slice in which black and grey ellipses are of the slices at the tail and head respectively.

The energy chirp from operating the booster off-crest is shown in Figure 3.13. It is clear such that the head of the bunch ($\Delta t > 0$) has lower energy than the tail of the bunch ($\Delta t < 0$).

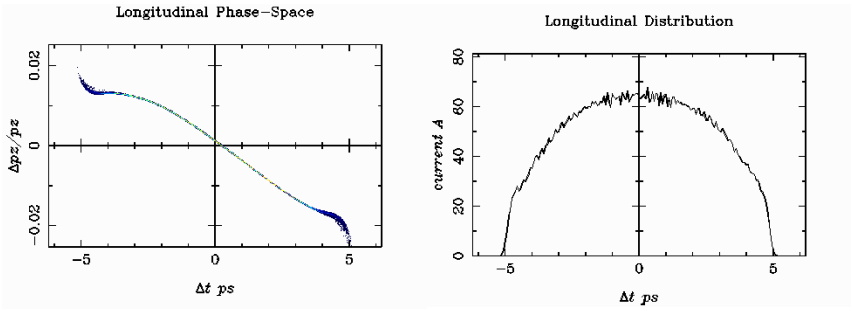


Figure 3.13: Longitudinal phase space (left) and distribution (right) at the end of the booster linac.

Bunch compression simulations

A magnetic chicane and an X-band harmonic cavity operating at 11.424 GHz are used to compress the bunch length. The optimisations of these components was done investigating their effect on the beam dynamics with the multiple-particle tracking with Elegant [46]. The 6D phase space data from the previous injector simulations with ASTRA was modified into Self-Describing Data Sets (SDDS) format and imported to perform the bunch compression simulations with Elegant. The layout of simulations with Elegant is displayed in Figure 3.14.

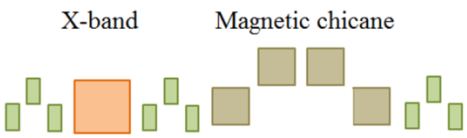


Figure 3.14: Bunch compression region has X-band harmonic cavity, magnetic chicane, and three quadrupole triplets (displayed in green).

The main targets of the optimisation are the control of the maximum value of the beta functions along the line and the minimisation of the horizontal beta function close to the fourth bending magnet of the chicane to reduce the emittance growth due to the CSR effects. Three sets of quadrupole triplets are located at the beginning of the X-band cavity, between the X-band cavity and the chicane, and at the end of the chicane for controlling the

transverse beam optics. The X-band amplitude and phase is tuned to linearise the longitudinal phase space distribution, removing the RF curvature generated by the S-band RF cavity. The accelerating field of the X-band cavity and bending angle of the chicane were scanned to shorten the bunch length and increase the peak bunch current while still maintaining an acceptable transverse emittance at the end of the compressor. The final parameters of the X-band cavity and the chicane are listed in Table 3.4.

Table 3.4: Parameters of X-band harmonic cavity and 4-bend magnetic chicane for THz FEL design.

Parameter	Value
X-band harmonic cavity	
Operating frequency	11.424 GHz
Cavity length	0.59976 m
Phase	-180°
Longitudinal electric field	4 MV/m
4-bend magnetic chicane	
Dipole magnet length	0.3 m
Distance between 1st and 2nd dipole magnets	0.5 m
Distance between 2nd and 3rd dipole magnets	0.5 m
Bending angle	12°
Quadrupole triplet 1	
Length	0.1,0.2,0.1 m
Strength	-9.8846, 10.3600, -11.4058 m^{-2}
Quadrupole triplet 2	
Length	0.1,0.2,0.1 m
Strength	0.1803, -2.8399, 8.3026 m^{-2}
Quadrupole triplet 3	
Length	0.1,0.2,0.1 m
Strength	-7.1356, 7.0450, 1.0361 m^{-2}

The transverse beam optics in this region of the layout is shown in Figure 3.15. The horizontal beta function is minimised and has the waist at the location of the last bending magnet as expected. The beam parameters in this simulation region are listed in Table 3.5. The bunch compression using the X-band cavity and the 4-bend chicane reduces the bunch length by a factor of 2.5 to 0.7 ps (0.21 mm) as shown in Figure 3.16, whereas the peak current is increased to 0.5 kA (Figure 3.17). The corresponding longitudinal phase space along the compression process is shown in Figure 3.18. On the other hand, the horizontal emittance growth of about 4 times presents in the horizontal phase space as illustrated in Figure 3.19.

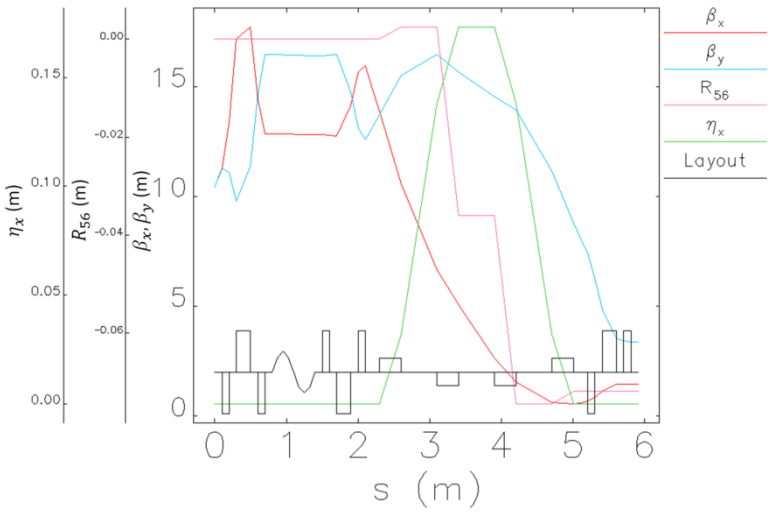


Figure 3.15: Optics functions along the bunch compression region including harmonic cavity and magnetic chicane.

Table 3.5: Initial and final beam parameters in the bunch compression region for THz FEL design.

Parameter	Before X-band	After chicane
rms bunch length	1.8 ps	0.7 ps
Peak current	80 A	0.5 kA
Normalised horizontal emittance	0.98 μm·rad	6.6 μm·rad
Normalised vertical emittance	0.98 μm·rad	0.97 μm·rad
Beam energy	19.76 MeV	17.65 MeV

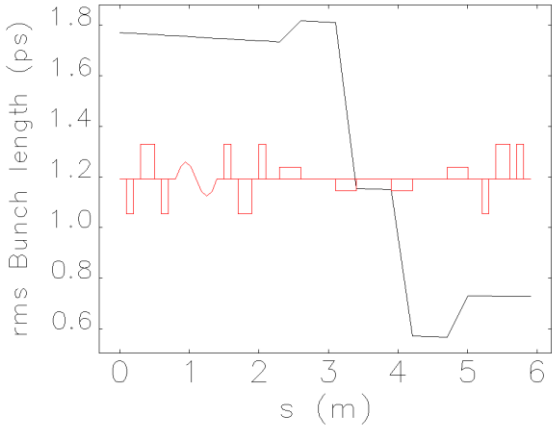


Figure 3.16: rms bunch length in the bunch compression region.

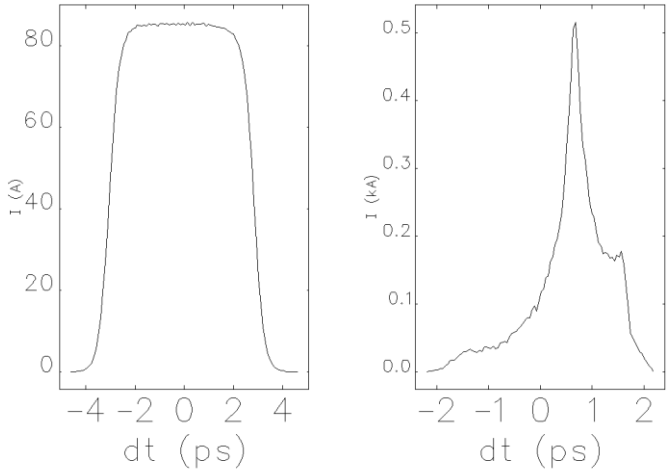


Figure 3.17: Longitudinal distribution of bunch current at the photoinjector (left) and after compression (right).

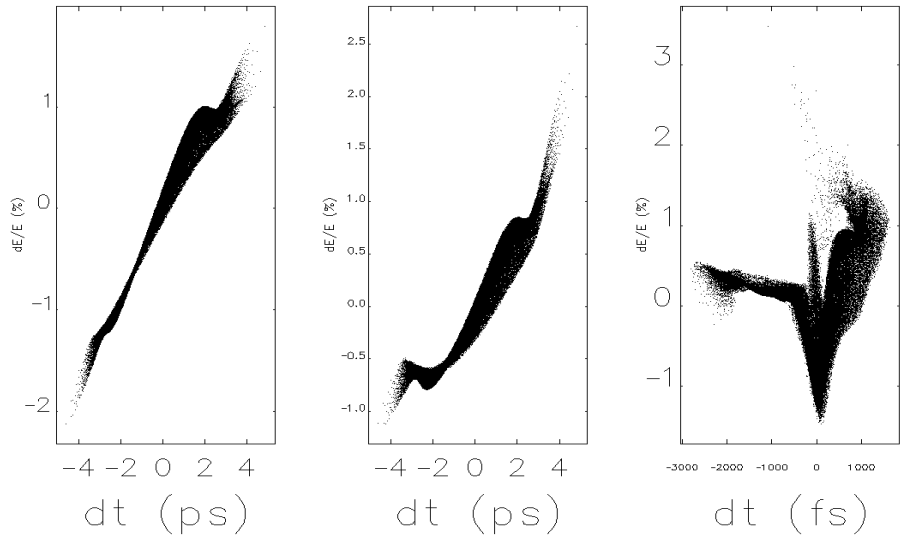


Figure 3.18: Longitudinal phase space at the beginning of the bunch compression region (left), after passing the X-band cavity (middle) and at the end of the region (right).

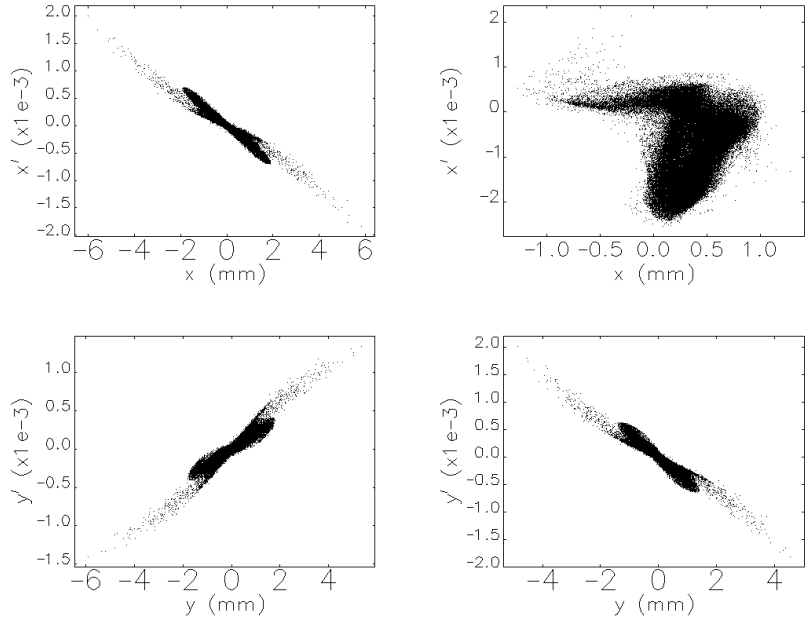


Figure 3.19: Horizontal (top) and vertical (bottom) phase space before (left) and after (right) bunch compression.

The 6D particle distribution from Elegant was converted into a suitable format to be used as input distribution for the GENESIS simulations to estimate the THz FEL generated from the compressed bunch.

Radiation generation simulations

We study here the THz FEL radiation emitted by the beam simulated with Elegant in the undulator. Our analysis focuses on the SASE FEL mode to generate THz radiation with GENESIS.

We used a planar undulator with period of 3.5 cm and gap of 1.2 cm corresponding to a resonance wavelength of 46.5 μm or the frequency of 6.4 THz. The main parameters of the GENESIS simulation are given in Table 3.6.

Table 3.6: Parameters for the THz FEL design in GENESIS simulations.

Parameter	Value
Undulator period (λ_u)	3.5 cm
Undulator gap (g)	1.2 cm
Undulator parameter (K)	2.06
Beam energy	17.5 MeV
Resonance wavelength (λ_r)	46.45 μm

The peak power along the undulator length in Figure 3.20 gives a saturation length of ~4 m. The beam current profile at the beginning of the undulator and the power profile at the undulator length of 4.7 m are displayed in Figure 3.21. At this undulator length, the FEL peak power is 1.49 MW, the rms FEL photon pulse duration is 2.07 ps with the pulse energy of 7.26 μJ and the spectrum (Figure 3.22) peaks at about the resonance wavelength of 46.45 μm or frequency of ~6.5 THz.

In this case, the Pierce parameter is about 0.01, the cooperation length $L_{coop} = 0.21\ mm$ or 0.71 ps. The FEL pulse is about 3 times of the cooperation length.

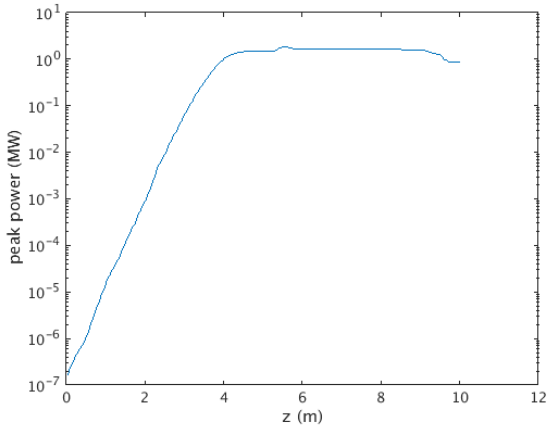


Figure 3.20: Peak power radiated from the 500-pC bunch along the undulator length.

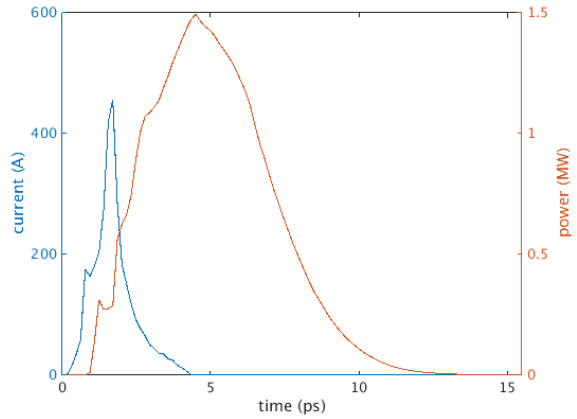


Figure 3.21: The initial bunch profile (blue) and the power profile at 4.7 m (orange).

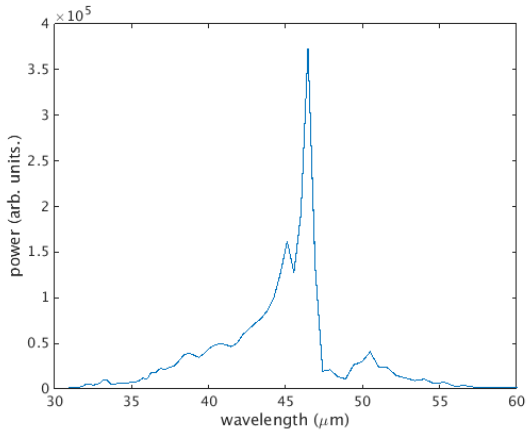


Figure 3.22: FEL spectrum at the undulator length of 4.7 m.

The FEL power with peak power over 1 MW and sharp spectrum in THz frequency range are generated from a planar undulator of length shorter than 5 m. The total length of the THz FEL source is 15.5 m (4.5 m for beam generation, 6 m for bunch compression and 5 m of undulator length) and would fit in a small-medium size laboratory like the one for the ASL project in Oxford.

3.3.2 THz CSR source

In view of reducing even further the footprint of the facility we have investigated the performance of a smaller size THz source, based on the generation of ultra-short bunches using a bending magnet as radiator and exploiting the coherent THz emission as described in Chapter 1. In particular, we have investigated the THz CSR emitted in the last dipole of the bunch compressor chicane as a possible radiation source.

The layout consists of two regions – beam generation and bunch compression as shown in Figure 3.23. It is similar to Figure 3.2, without the undulator at the end. Some effort has been made to maintain the two layouts as similar as possible from a hardware point of view. Although the final design requires slightly different positioning of the solenoids, it is believed that further optimisation could eventually produce promising results with exactly the same layout.

The optimisation process for this second operating mode of the injector linac follows a strategy similar to the one used for the THz FEL and present in the last paragraph. The start-to-end simulations were performed from the photocathode to the chicane, but in this case the radiation from the simulated electron bunch was estimated with the analytical model. The final energy, 50 MeV, is chosen to be larger than for the FEL (18 MeV) since we do not have the constraint of satisfying the FEL resonance condition in the THz region, while the critical energy of the radiation of the dipole should allow a good coverage of the

THz bandwidth (see Figure 1.2). The critical frequency of 36 THz can be obtained using the chicane magnet of the magnetic field strength 0.09 T with the bending radius of 1.85 m. Furthermore operating with higher energy and faster acceleration generally reduces the impact of space charge. Results of the simulations for this THz CSR design are discussed in details in this section.

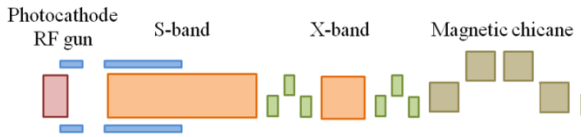


Figure 3.23: Layout of the THz CSR source. The last chicane dipole is used as a radiator. Blue and green components are solenoids and quadrupole triplets, respectively.

Beam generation simulations

The components in the injector are the same as in the previous layout (Figure 3.6). As in the previous case, a flat-top longitudinal laser profile is used to generate the electron bunch at the cathode in order to reduce the space charge effects in the RF gun. The laser parameters are listed in Table 3.7 and the transverse and longitudinal distributions are shown in Figure 3.24 and 3.25. A slightly shorter laser rise time has been used to improve the beam dynamics with space charge.

Table 3.7: Laser beam parameters at the cathode of the photoinjector for THz CSR source design.

Parameter	Value
Laser pulse length	6.0 ps (flat-top)
Rise/fall time	0.1 ps
Longitudinal energy distribution	Isotropic
Energy distribution width	1.1 eV
Transverse momentum distribution	Radial uniform
Transverse rms laser beam size	0.5 mm
Bunch charge	500 pC

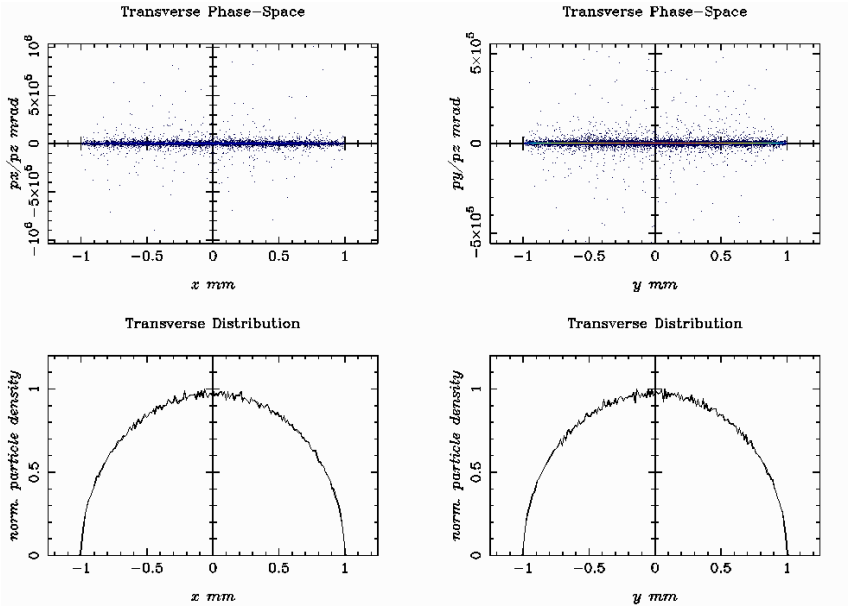


Figure 3.24: Transverse phase space (top) and distribution (bottom) at the cathode.

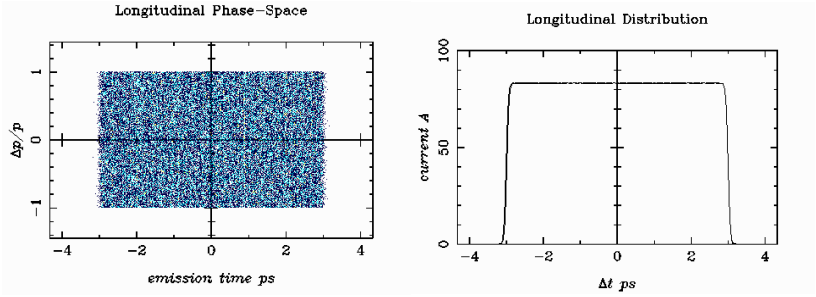


Figure 3.25: Longitudinal phase space (left) and distribution (right) at the cathode.

The optimised phase of the RF gun, maximum magnetic field and position of solenoid 1 are shown in Table 3.8. The beam waist is at 1.327 m from the cathode.

Table 3.8: Parameters for locating a beam waist at 1.327 m from the cathode.

Parameter	Value
Maximum longitudinal electric field of RF gun	120.2 MV/m
Phase of the electric field of RF gun	-4.05°
Maximum magnetic field of solenoid 1	0.2758 T
Position of solenoid 1	0.1907 m

The booster linac is placed at the waist position with parameters listed in Table 3.9 for compensating the emittance. For this design, the accelerating field of the booster is chosen to be higher than the FEL case as the final beam energy is not limited to the resonance wavelength in order to generate THz radiation. The accelerating gradient used, 25 MV/m, is still below the optimal value obtained from the theoretical analysis of the emittance compensation (Equation (3.6) predicts about 46 MV/m). The aim of having the higher energy beam is to achieve smaller emittance in the beam generation region.

Table 3.9: Optimised parameters of booster linac and solenoid 2 for THz CSR source design.

Parameter	Value
Maximum longitudinal electric field of booster linac	25.46 MV/m
Phase of the electric field of booster linac	-30°
Maximum magnetic field of solenoid 2	-0.1397 T
Position of solenoid 2	2.258 m
Beam energy at the end of booster linac	55.28 MeV
Normalised emittance at the end of booster linac	0.76 μm·rad
Beam size at the end of booster linac	0.35 mm
rms energy spread	1.55 %

Figure 3.26 shows the normalised transverse emittance and beam size along the injector region.

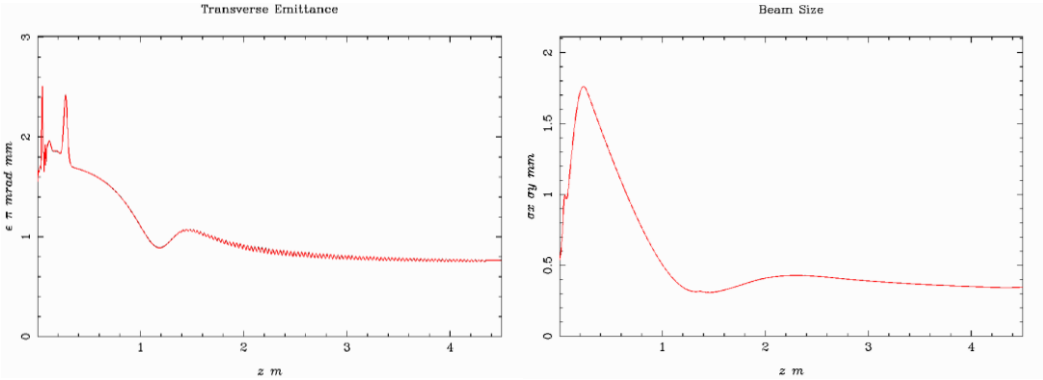


Figure 3.26: Normalised transverse emittance (left) and transverse beam size (right) along the injector region.

The transverse phase spaces and slice emittance are shown in Figure 3.27 and 3.28, respectively. The slice emittance along the bunch and the correct alignment of the phase space ellipses produce the lowest possible projected emittance for this design. The use of short rise time in the longitudinal laser profile helps to alleviate the effect of the space charge forces at both ends of the bunch.

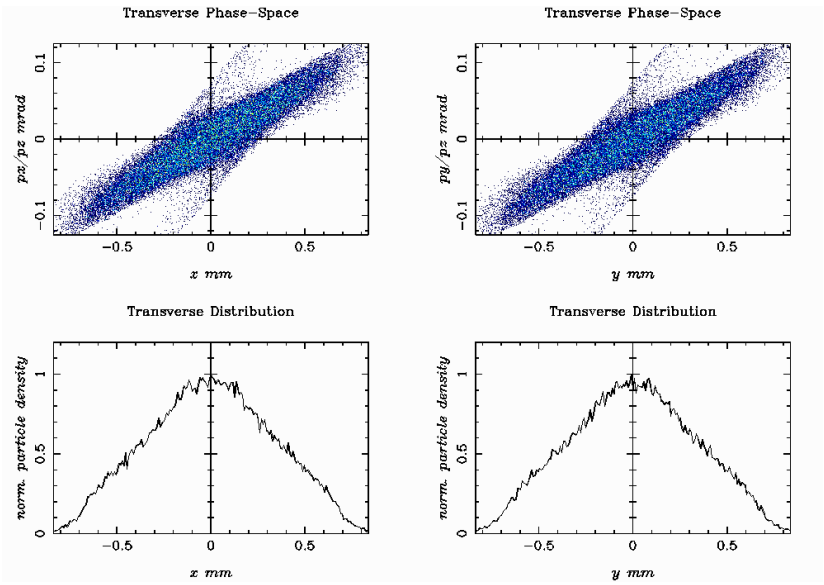


Figure 3.27: Horizontal (left) and vertical (right) phase space (top) and distribution (bottom) at the end of the booster linac.

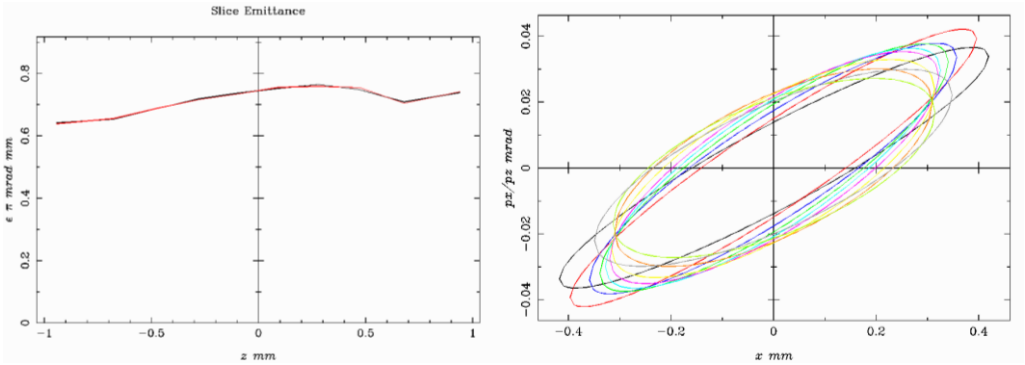


Figure 3.28: Slice emittance of slices along the bunch (left) and slice ellipses in horizontal phase space (right) at the end of the booster linac. Each ellipse represents a bunch slice and black and grey ellipses are of the slices at the tail and head of the bunch respectively.

The energy chirp can be seen in Figure 3.29. Again, the head of the bunch is at $\Delta t > 0$ and the tail is at $\Delta t < 0$ in ASTRA.

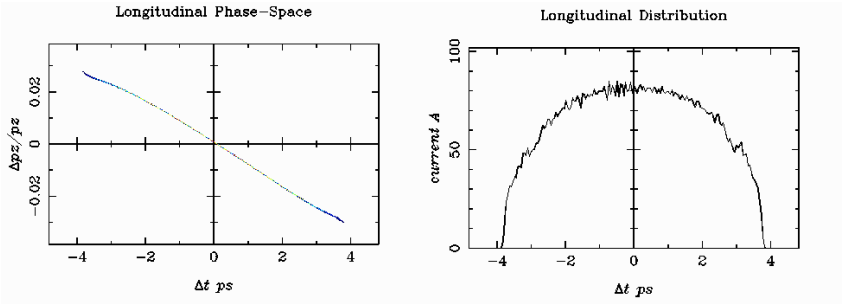


Figure 3.29: Longitudinal phase space (left) and distribution (right) at the end of the booster linac.

Bunch compression simulations

The 6D phase space distribution from ASTRA is used in tracking simulations with Elegant through the same bunch compressor for the FEL design in Figure 3.14.

Optimisations were done by scanning the bending angle of the chicane dipoles to get short electron bunch with high peak current and low emittance. Parameters of the optimised design are given in Table 3.10.

Table 3.10: Parameters of X-band harmonic cavity and 4-bend magnetic chicane for THz CSR source design.

Parameter	Value
X-band harmonic cavity	
Operating frequency	11.424 GHz
Cavity length	0.59976 m
Phase	-180°
Longitudinal electric field	4 MV/m
4-bend magnetic chicane	
Dipole magnet length	0.3 m
Distance between 1st and 2nd dipole magnets	0.5 m
Distance between 2nd and 3rd dipole magnets	0.5 m
Bending angle	9.3°
Quadrupole triplet 1	
Length	0.1,0.2,0.1 m
Strength	-6.0851, 6.2957, -6.6537 m^{-2}
Quadrupole triplet 2	
Length	0.1,0.2,0.1 m
Strength	4.5075, -5.1962, 8.4596 m^{-2}
Quadrupole triplet 3	
Length	0.1,0.2,0.1 m
Strength	-16.7544, 3.6164, 8.5680 m^{-2}

The beam optics in Figure 3.30 confirms that the horizontal beta function is minimised at the last dipole for reducing the emittance growth due to the CSR effects. Beam parameters for the optimised design are in Table 3.11.

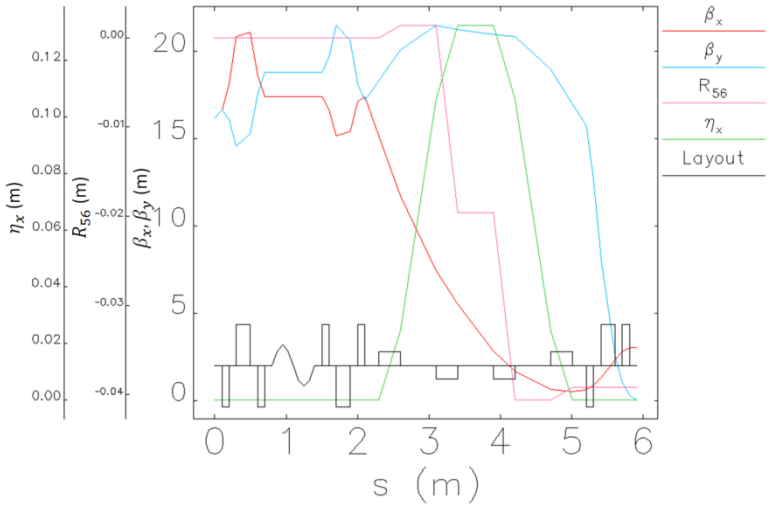


Figure 3.30: Optics functions along the bunch compression region including harmonic cavity and magnetic chicane.

Table 3.11: Initial and final beam parameters in the bunch compression region for THz CSR source design.

Parameter	Before X-band	After chicane
rms bunch length	1.7 ps	126 fs
Peak current	80 A	2.5 kA
Normalised horizontal emittance	0.76 μm·rad	5.0 μm·rad
Normalised vertical emittance	0.76 μm·rad	0.82 μm·rad
Beam energy	55.28 MeV	53.17 MeV

The bunch length in the compression region is reduced by a factor of 13 to 126 fs (Figure 3.31) with the peak current of 2.5 kA (Figure 3.32) thanks to the harmonic cavity and the chicane. However, the bunch has the horizontal emittance growth about 6 times larger after compression. The longitudinal and transverse phase space are illustrated in Figure 3.33 and 3.34.

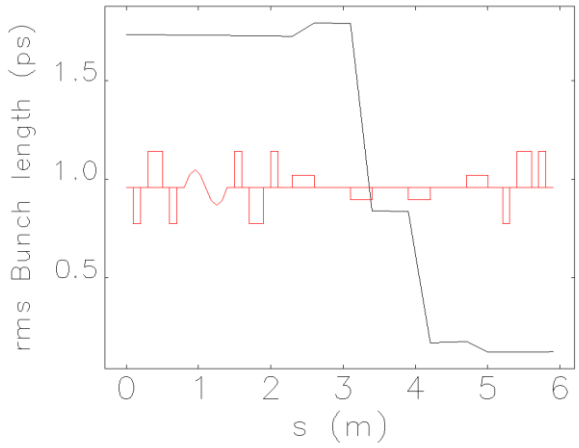


Figure 3.31: rms bunch length in the bunch compression region.

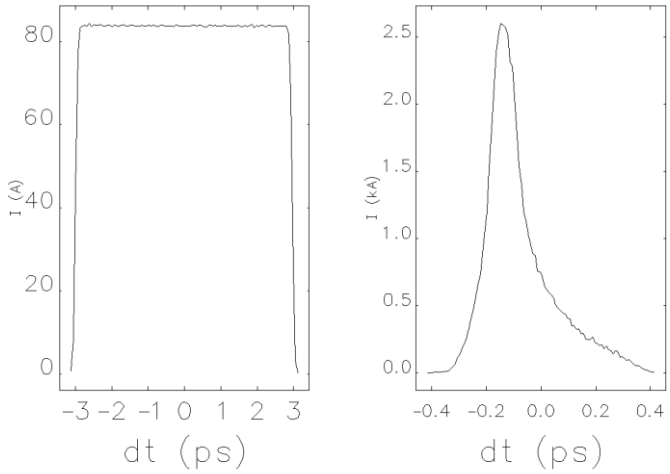


Figure 3.32: Longitudinal distribution of bunch current from the beam generation region (left) and from the compression region (right).

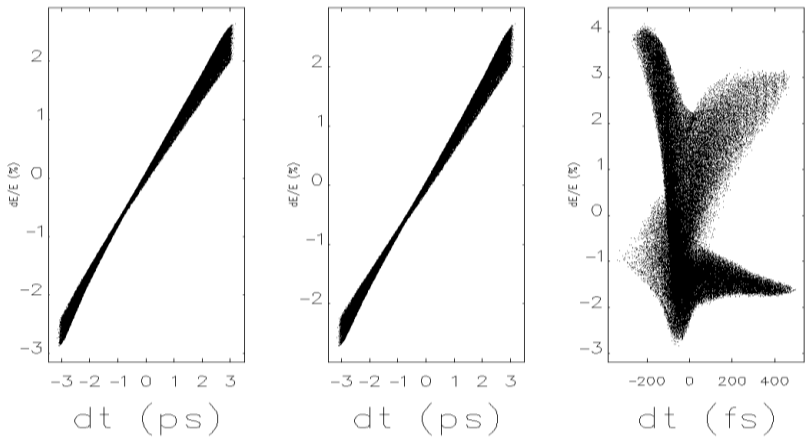


Figure 3.33: Longitudinal phase space at the beginning of the bunch compression region (left), after passing the X-band cavity (middle) and at the end of the region (right).

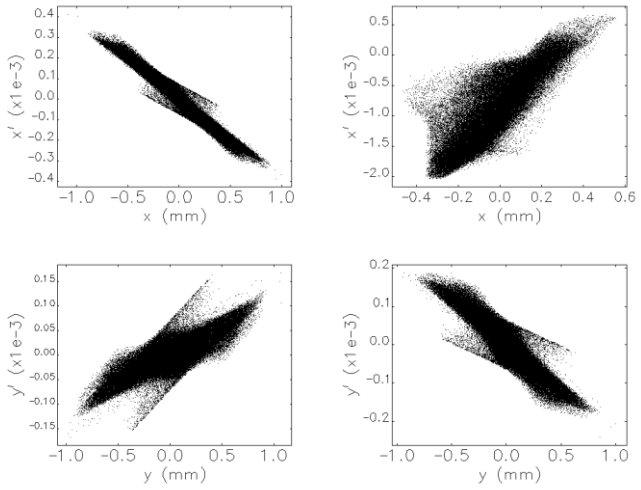


Figure 3.34: Horizontal (top) and vertical (bottom) phase space before (left) and after (right) bunch compression.

CSR from the compressed bunch

The spectrum emitted by the compressed bunch is estimated analytically. The spectrum from a single electron is evaluated following Equation (1.6). The longitudinal bunch profile is used to find the form factor then the single particle spectrum and the form factor are used to calculate the spectrum of the whole bunch.

Figure 3.35 shows that the spectral intensity at frequency below 16 THz is enhanced by the factor of $\sim 3 \times 10^9$ corresponding to the number of electrons in the bunch.

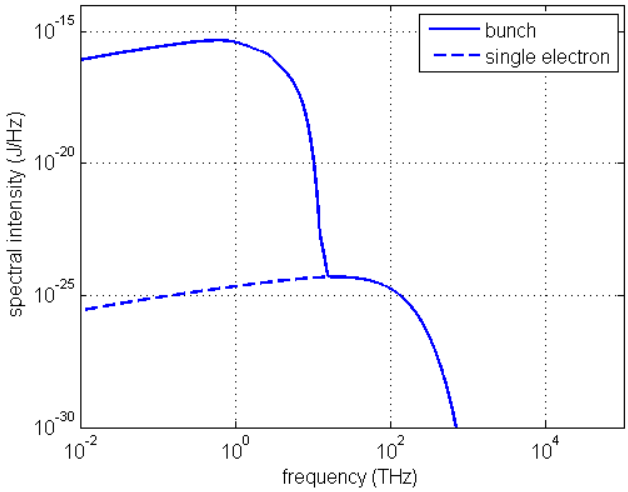


Figure 3.35: Spectrum of radiation emitted by the 500-pC bunch at the last chicane bending magnet with 1.85 m bending radius.

The bunch is compressed to rms bunch length of 126 fs and it emits CSR with broad spectral range up to 16 THz. For the frequency range below 100 THz, the energy per pulse is 0.9 mJ, the peak power per pulse is about 3 GW (estimating the radiation pulse length with the electron bunch length) and the average power of 90 mW for the repetition rate of 100 Hz. The start-to-end simulations in both THz FEL and THz CSR designs give reasonably good results in terms of bunch length, peak current, peak power and radiated spectrum. In this design, the total length of the source is 10.5m (4.5 m for beam generation and 6 m for bunch compression).

3.4 Summary

In this chapter, an RF-linac driven THz sources is studied in two designs based on two different processes: FEL radiation generated with an undulator and CSR generated with

a bending magnet. The design of the machine is optimised to fit in a small-medium size laboratory like the one devised for the ASL project in the Oxford University.

Full start-to-end simulations were performed in both cases to investigate the beam dynamics from the RF gun to the bunch compression and the generation of THz radiation. The emittance compensation theory was used as a guidance for the optimisation to compensate and control the emittance growth due to space charge forces, however the final parameters were set on the basis of the more comprehensive results of extensive numerical simulation. The 4-bend magnetic chicane and the harmonic cavity were included in the bunch compression region for longitudinal bunch compression to reduce the bunch length and the resulting radiation pulse length. The radiation at the end of the linac was evaluated with different methods for each generation process.

For the THz FEL, the beam was accelerated to low energy of 17.5 MeV in order to have the FEL resonance wavelength in THz range. The bunch length was compressed to 0.7 ps rms with peak current of 0.5 kA. By passing the electron bunch through a planar undulator of 4.7 m long, the FEL can be produced at frequency of 6.46 THz (wavelength of 46.45 μm), peak power of 1.49 MW, and radiation pulse duration (rms) of 2.07 ps which gives the energy 7.26 μJ per pulse. Assuming repetition rate of 100 Hz, the average power is 726 μW.

For the THz CSR, a higher beam energy was used to reduce space charge effects in the beam generation resulting in smaller transverse emittance. The compressed electron bunch has rms bunch length of 126 fs with the peak current of 2.5 kA. The CSR with broad spectrum up to 16 THz can be produced. Considering over a broad spectrum up to 100 THz, the energy per pulse is 0.9 mJ, peak power of 3 GW, and average power of 90 mW for 100 Hz repetition rate. The FEL radiated power is generated in a much smaller bandwidth.

For comparison the CSR radiation in the same bandwidth 6.46±0.05 THz is considered. In this case, the radiation energy is 0.51 μJ per pulse emitted from an electron bunch of rms length 126 fs. The peak power is then 1.7 MW and the average power is 51 μW assuming 100 Hz repetition rate.

The machine parameters proposed for the operation of the linac based THz source were used as baseline for the calculation of the shielding requirement for the ASL as discussed in Chapter 5.

Chapter 4

THz Radiation and Short Pulses with a LPWA

In Chapter 2 we have discussed the possibility of generating THz radiation in storage ring light sources and we have seen that this can be done in specific operating modes that are incompatible with the standard operation of the machine. Therefore storage rings provide a rather limited access to THz sources. The sources based on RF linacs, discussed in Chapter 3, provide a more affordable, dedicated, solution being driven by relatively small size accelerators. It is evident, however, that THz radiation sources could profit from more compact and economic solutions, based on more advanced and novel acceleration technologies. Laser plasma wakefield accelerators (LPWAs) have been intensely studied in the recent years as a possible candidate for providing alternative acceleration method to the standard RF technology. In this chapter, we explore the possibility of using a LPWA to drive low photon energy source with the aim of reaching IR and THz radiation in a small compact accelerator device that can be installed in small areas, affordable by university–sized laboratories.

LPWAs have the potential to accelerate particle beams by means of extremely high accelerating gradients, typically 100-1000 times larger than the gradient available in conventional RF technology. For example, 1-GeV electron beam can be generated in a plasma channel of a few cm length [77], implying gradients in the order of tens GV/m rather that the more common tens of MV/m achievable in RF cavities. An important feature of the LPWA is that it naturally produces ultra-short charged particle bunch, in the order of tens of fs. Such ultra-short bunch length is of great interest for the production of short pulse

THz radiation. In this chapter, we investigate the possibility of generating THz and IR radiation from the LPWA, the challenges met in dealing with such bunches and the possible expected performances of a radiator driven by a LPWA.

The chapter begins with a short discussion of the physics principle of the laser plasma acceleration including linear and nonlinear regimes for the creating the cavity-like structure with high accelerating gradient in the plasma and self-injection scheme for producing the electron bunch. The characteristic of the beam are analysed in order to gain an insight in the properties of the IR radiation that can be generated from such electron bunches.

4.1 Physics of laser plasma acceleration

The concept of plasma acceleration was proposed in 1979 [78]. In its original form, the acceleration is based on an intense laser pulse that is sent in a plasma where it generates a strong charge density modulation. Such density modulation is responsible for the generation of strong electric fields, called plasma wakefields, which can be used to accelerate the charged particle beam. The electric fields generated in the plasma do not suffer from the limits imposed by the breakdown of the material sustaining the fields in the RF cavity, since the plasma is already electrically broken down, and this is the main reason why high electric field can be obtained. The acceleration of electrons in plasma can be done by exciting the plasma with high intensity laser pulse or high energy charged particle bunch. In this chapter, we have analysed a first scenario where a high power laser is used to generate ultra-short electron pulses in the bubble regime.

4.1.1 Excitation of plasma wakefield by an intense laser pulse

When the laser pulse enters the plasma, the electric field of the laser acts on the electrons in the plasma pushing them away from the laser propagation direction. Indicating the electric field of the laser pulse in the form of

$$\vec{E}(\vec{r},t) = \vec{E}_0(\vec{r},t)\cos\omega_0 t \tag{4.1}$$

where ω_0 is the angular frequency and $\vec{E}_0(\vec{r},t)$ is the slow varying field amplitude, the time-averaged force known as "ponderomotive force" acting on a plasma electron is given by

$$\vec{F}_p = -\frac{e^2}{4m_e\omega_0^2}\vec{\nabla}\left|\vec{E}_0\right|^2. \tag{4.2}$$

The ponderomotive force is larger in the regions where the gradient of the intensity of the laser pulse is large, since the laser intensity is $I \propto \left|\vec{E}_0\right|^2$ and the ponderomotive force reads $F_p \propto -\nabla I$. Such force pushes electrons out of a region with high laser intensity.

As the ponderomotive force pushes electrons out of the laser axis, the plasma ions pull them back towards their original positions to re-establish the charge neutrality. In this way the electrons start an oscillation about their positions and such oscillation continue trailing the propagation of the laser pulse. When the plasma electrons are perturbed and move away from their equilibrium position, they generate an electric field

$$E = \frac{nex}{\varepsilon_0} \tag{4.3}$$

where x is the displacement of the electrons from their equilibrium positions and n is the electron density in the plasma and ε_0 is the permittivity of free space [79]. The Coulomb forces between the displaced electrons and the whole plasma act as the restoring forces initiating plasma oscillations at the electron plasma frequency (ω_p) express by

$$\omega_p = \sqrt{\frac{ne^2}{\varepsilon_0 m_e}} \tag{4.4}$$

here m_e is the electron rest mass. It is useful to define the plasma wavelength $\lambda_p = \frac{2\pi c}{\omega_p}$ and plasma wavenumber $k_p = \frac{2\pi}{\lambda_p} = \frac{\omega_p}{c}$ from the plasma frequency Equation (4.4).

The plasma oscillation therefore creates a longitudinal electron density wave with a longitudinal electric field, known as "plasma wakefield" that can be used for accelerating particles behind the laser pulse. The laser pulse length should be comparable to or smaller than the plasma wavelength so that the laser field can effectively excite the plasma. In the linear regime, the accelerating field in the plasma from Equation (4.3), assuming electrons moving at speed of light and the maximum displacement between the plasma wave front of $x \approx \frac{c}{\omega_p}$, is expressed by

$$E_0 = \frac{ne}{\varepsilon_0}\left(\frac{c}{\omega_p}\right) = \frac{m_e c \omega_p}{e}. \tag{4.5}$$

The plasma wakefield can accelerate charged particles that become trapped or are injected in the plasma. The dynamics of the plasma is characterised by the laser intensity or normalised vector potential defined by

$$\vec{a} = \frac{e\vec{A}}{m_e c^2} \tag{4.6}$$

where $\vec{A}$ is the vector potentials of the laser field and the amplitude of the normalised vector potential in terms of the laser electric field amplitude E_{max} is

$$a_0 = \frac{eE_{max}}{m_e \omega_0 c}. \tag{4.7}$$

For the low intensity laser ($a_0 \ll 1$) propagating through underdense plasma $n < n_c$, where $n_c = m_e \varepsilon_0 \omega_0^2 / e^2$ is the plasma critical density which is $n_c = 1.75 \times 10^{21}\ cm^{-3}$

for the laser of wavelength 800 nm, the electrons in the plasma oscillate generating the sinusoidal plasma wakefields trailing the laser pulse. In this case, we say that the plasma acceleration is in a linear regime. For the interaction of the high intensity laser ($a_0 \gg 1$) with the underdense plasma, the plasma electrons develop a cavity-like structure or "bubble" with extremely high axial electric fields inside the bubbles. This is the so–called nonlinear or bubble regime.

The bubble regime is of particular interest for us because, besides producing the extremely high accelerating fields generated in the bubble, it also creates an electron bunch inside the bubble itself. This phenomenon is referred to as self-injection. This bunch is then accelerated in the bubble as will be discussed in more details below. Examples of linear and nonlinear plasma wakefields excited by a laser pulse are shown in Figure 4.1.

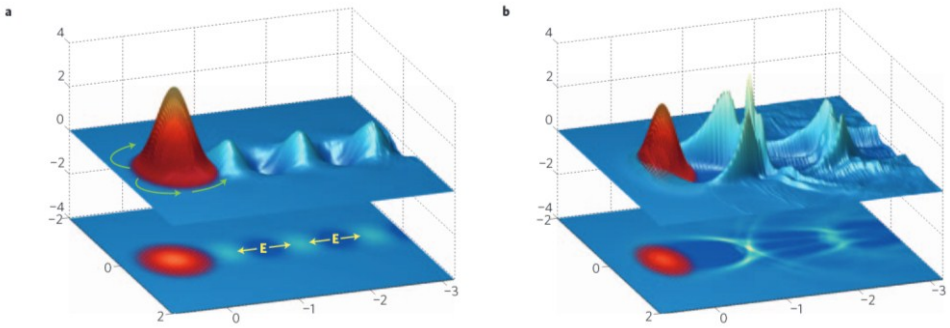


Figure 4.1: Examples of linear (left) and nonlinear (right) plasma wakefields [80].

The present technology of lasers allows the operation of LPWA in the bubble regime ($a_0 \gg 1$). Commercially available laser system used in the plasma acceleration produce many tens of TW in typically 30 fs (FWHM) pulses with Ti:Sapphire lasers operating at 800 nm [81]. However, the repetition rate of such lasers is limited to few Hz.

An intense R&D effort is ongoing in trying to increase the repetition rate and efficiency of the driving laser by using fibre laser [82], or by devising alternative excitation

techniques like multi-pulses laser excitation [83]. In this chapter, we have analysed a first scenario where a laser in the bubble regime is used to generate ultra-short electron pulses.

4.1.2 Laser plasma wakefield acceleration in the bubble regime

When a highly intense laser pulse with $a_0 \gg 1$ is launched into the plasma, the ponderomotive force completely expels the plasma electrons out of the laser propagation direction and the region becomes almost in a spherical shape or so-called a bubble with only plasma ions inside following the laser pulse at relativistic velocity.

The bubble regime is characterised by a region along the axis of propagation of the laser with a longitudinal accelerating field that varies linearly with the distance from the laser pulse $\zeta = z - ct$ and a radial focussing field that varies linearly with the radial distance from the axis of the bubble. An example of the bubble region is shown in Figure 4.2. Assuming a spherical bubble of radius r_B moving at relativistic velocities, the axial, radial and azimuthal electric fields, respectively, inside the bubble are given by [84]

$$\begin{aligned} E_z &\approx \left(\frac{k_p \zeta}{2}\right) E_0 \\ E_r &\approx \left(\frac{k_p r}{4}\right) E_0 \\ B_\theta &\approx -\left(\frac{k_p r}{4}\right) E_0. \end{aligned} \tag{4.8}$$

The axial electric field reaches its maximum value at the longitudinal distance $\zeta \approx r_B$ both at front and back of the bubble with opposite directions. The transverse focussing force is given by $F_r = -e(E_r - B_\theta) = -e\left(\frac{k_p r}{2}\right) E_0$. These forces guarantee the simultaneous acceleration and focussing of electrons inside the bubble.

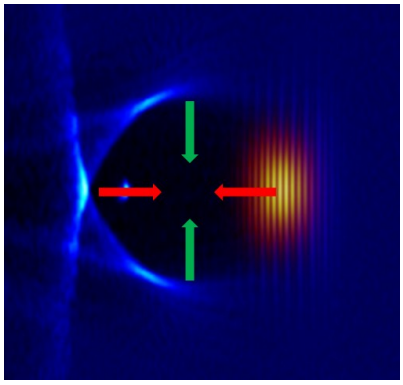


Figure 4.2: Accelerating field in a bubble region. The red arrows show the accelerating/decelerating forces and the green arrows show the direction of focussing forces inside the plasma bubble (adapted from [85]).

Assuming a Gaussian laser pulse with profile $a = a_0 \exp(-2\,r^2/r_0^2)$ and laser spot size r_0 at the focus, in circular polarisation, the bubble can be formed if the laser intensity satisfies the condition [84]

$$\frac{a_0^2}{\sqrt{1+a_0^2}} \geq \frac{k_p^2 r_0^2}{4} \tag{4.9}$$

In the high intensity limit $a_0 \gg 1$, (4.9) reads $a_0 \geq \frac{k_p^2 r_0^2}{4}$ and the laser spot size should satisfy the relation $r_0 \leq \frac{2\sqrt{a_0}}{k_p}$. In these conditions the bubble radius is

$$r_B \approx \frac{2\sqrt{a_0}}{k_p} \tag{4.10}$$

The corresponding maximum electric field reads

$$E_{max} \approx \sqrt{a_0} E_0 \tag{4.11}$$

which exceeds the accelerating field in the linear regime given by Equation (4.5) and therefore allowing the operation of the LPWA in the nonlinear regime ($a_0 > 1$).

4.1.3 Self-injection in the bubble regime

The electrons expelled by the high-intensity laser pulse move along the boundary of the bubble and move backward to the base of the bubble. Some of the electrons accumulated at the bubble base may travel faster than the plasma wakefield and then possibly slip and are trapped into the bubble. This phenomenon is called "self-injection". When this happens, the trapped electrons experience the accelerating field at the back half of the bubble and undergo acceleration in the plasma. The schematic of self-injection in the bubble regime is shown in Figure 4.3.

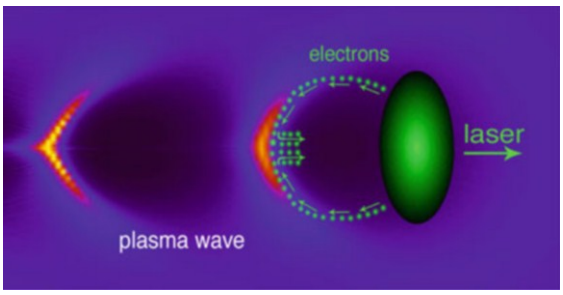


Figure 4.3: Self-injection in bubble regime [86].

4.1.4 Self-focussing and matching conditions of the laser

A short laser pulse of length $L < \lambda_p$ can be guided by relativistic self-focussing when the laser power $P \gg P_c$ where $P_c = 17\frac{\omega_0^2}{\omega_p^2}\ [GW]$ is the critical power for relativistic self-focussing. Since the laser intensity on the propagation axis is stronger than the off-axis intensity, the relativistic factor γ of the plasma electrons decreases with increasing radial distance from the propagation axis resulting in a radial variation of the electron's relativistic mass which gives rise to a spatially varying refractive index of the plasma. The laser is, therefore, focussed due to the relativistic mass increase. In the case of $P \geq P_c$, the laser can be guided by introducing a transverse plasma density modulation by means of electrical discharges in a plasma capillary [87]. However, self-guiding of the laser with $P \geq P_c$ in the

uniform plasma density is possible if the laser has appropriate spot size and intensity satisfying matching conditions found in [88] which are

$$r_0 = \frac{2\sqrt{a_0}}{k_p}, \qquad a_0 \approx 2\left(\frac{P}{P_c}\right)^{\frac{1}{3}} \tag{4.12}$$

The matched laser spot size can estimate the bubble radius $r_B \approx r_0$.

4.1.5 Energy gain in plasma acceleration

There are three main mechanisms which limit the achievable energy gain of the electron bunch in plasma. First, in vacuum, the laser spot size r_s increases as the laser pulse propagates due to diffraction according to

$$r_s = r_0\left(1 + \frac{z^2}{Z_R^2}\right)^{1/2} \tag{4.13}$$

where r_0 is the minimum spot size and $Z_R = \frac{\pi r_0^2}{\lambda_0}$ is the Rayleigh length. In plasma, the laser can propagate through several Z_R without any optical guiding. Second, at a certain distance in the plasma, the accelerated electrons travel at highly relativistic velocities and start outrunning the wakefield hence the plasma acceleration cannot continue. This phenomenon is called de-phasing and for the nonlinear limit $a_0 \gg 1$, this distance or dephasing length is given by [88]

$$L_d \approx \frac{2}{3}\frac{\omega_0^2}{\omega_p^2}R = \frac{4}{3}\frac{\omega_0^2}{\omega_p^2}\frac{\sqrt{a_0}}{k_p} \tag{4.14}$$

where λ_0 is the wavelength of the laser pulse. Third, the laser pulse loses its energy to drive the plasma wakefield, i.e. the pump depletes. The pump depletion length is the length after which the energy in the laser pulse equals to the energy lost to the wakefield and is given by [88]

$$L_{pd} \approx \frac{\omega_p^2}{\omega_0^2} c\tau_{FWHM}. \tag{4.15}$$

Typically, Z_R is much shorter than L_d and L_{pd} and $L_d \sim L_{pd}$ in nonlinear regime and hence the energy gain is limited by the dephasing length.

The energy gain and the number of accelerated electrons in the LPWA in the nonlinear regime was estimated analytically and numerically in [88]. The energy gain is given by

$$\Delta E \approx m_e c^2 \left(\frac{P}{m_e^2 c^5/e^2}\right)^{\frac{1}{3}} \left(\frac{n_c}{n}\right)^{\frac{2}{3}} \tag{4.16}$$

and the energy gain in practical units is expressed by

$$\Delta E[GeV] \approx 1.7 \left(\frac{P[TW]}{100}\right)^{\frac{1}{3}} \left(\frac{10^{18}}{n[cm^{-3}]}\right)^{\frac{2}{3}} \left(\frac{0.8}{\lambda_0[\mu m]}\right)^{\frac{4}{3}}, \tag{4.17}$$

whereas the number of accelerated electrons can be estimated as

$$N \approx \frac{8}{15 k_0 r_e} \sqrt{\frac{P}{m_e^2 c^5/e^2}} \tag{4.18}$$

here $k_0 = \frac{2\pi}{\lambda_0}$ and $r_e = \frac{e^2}{m_e c^2}$ is the classical electron radius, and in practical units given by

$$N \approx 2.5 \times 10^9 \left(\frac{\lambda_0[\mu m]}{0.8}\right) \left(\frac{P[TW]}{100}\right)^{\frac{1}{2}}. \tag{4.19}$$

As an example, using a commercially available Ti:Sapphire laser generating pulses with wavelength of 800 nm and power of 10 TW into plasma of density of $8 \times 10^{18}\ cm^{-3}$ is expected to accelerate an electron bunch of charge ~120 pC to the maximum energy gain of 197 MeV. These parameters will be used in the following simulations to drive a LPWA based radiation source with a modest Ti:Sapphire laser system that can fit in a university

based laboratory. In the following paragraph, an example of the self-injected electron beam from a LPWA simulation is presented.

4.2 Simulation of a self-injected electron beam

The beam dynamics in the LPWA is defined by the complex nonlinear interactions between laser and particles in plasma and can only be studied in details with numerical simulations based on particle-in-cell (PIC) codes. These are capable of handling the evolution of a large number of macro-particles representing the electron beam and to follow the evolution of the laser pulse. The evolution of the beam is characterised by the Vlasov-Maxwell equation given by

$$\frac{\partial f}{\partial t} + \vec{v} \cdot \vec{\nabla}_x f + \frac{e}{m}\left(\vec{E} + \vec{v} \times \vec{B}\right) \cdot \vec{\nabla}_v f = 0 \tag{4.20}$$

where $f(\vec{x}, \vec{v}, t)$ is the density distribution in phase space, $\vec{x}$ and $\vec{v}$ are spatial and velocity coordinates and $\vec{E}$ and $\vec{B}$ are the electromagnetic field of the laser pulse propagating in the plasma.

4.2.1 Particle-in-cell simulation

There are several PIC codes available which can be used to study the laser plasma interactions under different assumptions. We used EPOCH [89] that allows the analysis of the 1D (*epoch1d*), 2D (*epoch2d*) and 3D (*epoch3d*) dynamics on a moving window. The 2D version *epoch2d* is fast enough to allow scanning and optimising parameters to improve the operation of the LPWA in the nonlinear or bubble regime with self-injected electron bunch. This has been used to make preliminary estimates of the performance of a possible LPWA to drive THz/IR radiation.

The PIC simulation is a numerical method used to solve the Vlasov-Maxwell equation given by Equation (4.20). Macro-particles are used to represent the actual collection of

particles in the system and the space is discretised in grid cells. The dynamics of both particles and electromagnetic field is followed on a grid in space and time. The steps of the PIC algorithm are the following:

1. Initialise macro-particle distribution on continuum space
2. Extrapolate coordinates of particles to discrete charge density distribution on the grid and solve Maxwell's equations to obtain discrete electromagnetic fields on the grid
3. Calculate forces from the discrete fields and act on the macro-particles
4. Solve equation of motions due to the electromagnetic forces for getting new charge density distribution

The algorithm continues in a loop in discrete time step.

4.2.2 2D PIC simulation of nonlinear LPWA

The simulation was done aiming to produce an electron beam of energy below ~200 MeV for generating either CSR from a dipole magnet or driving FEL. Parameters for both simulations are shown in Table 4.1. In order to maintain the laser power to reasonable values, we opted for a case with $a_0 = 2.8$ corresponding to 10 TW in 20 fs pulses.

The results of the eopch2d-runs are presented below. Bubble structures can be seen in the first simulation output at 0.2 ps as shown in Figure 4.4. Some electrons are injected at the back of the first bubble and a self-injected bunch starts to develop. Figure 4.5 gives the electric field components, transverse and longitudinal respectively. It is clear that, inside the bubble, the fields are linear with transverse and axial coordinates hence providing the linear focussing and accelerating forces, respectively, inside the bubble.

Table 4.1: EPOCH parameters for generation of an electron bunch from the LPWA in the bubble regime.

Parameter	Value
Laser	
Wavelength (λ)	800 nm
Power (P)	10 TW
FWHM Pulse duration (T)	20 fs
rms spot size (r_0)	9 µm
Intensity (I)	$1.66 \times 10^{19}\ W/cm^2$
Normalised vector potential (a_0)	2.8
Plasma	
Density (n)	$8 \times 10^{18}\ cm^{-3}$
Simulation control	
Window	80 µm × 100 µm
Number of grids	4000×256
Longitudinal resolution ($k\Delta z$)	0.16
Transverse resolution ($k_p \Delta y$)	0.21
Number of electrons per cell	16

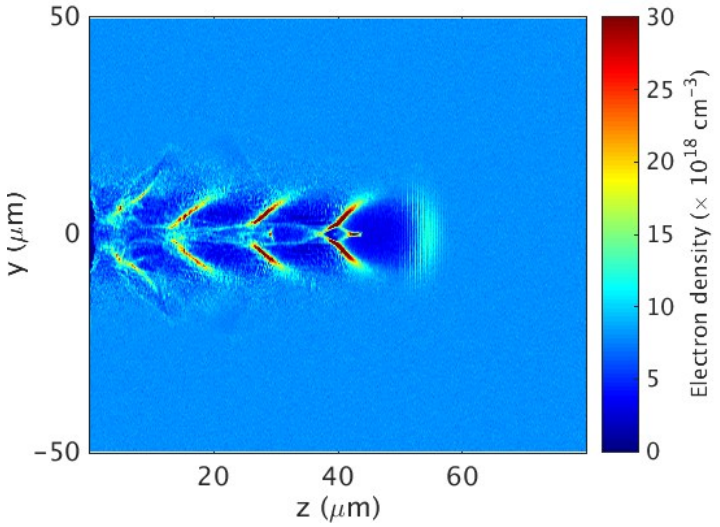


Figure 4.4: 2D electron density at 0.2 ps.

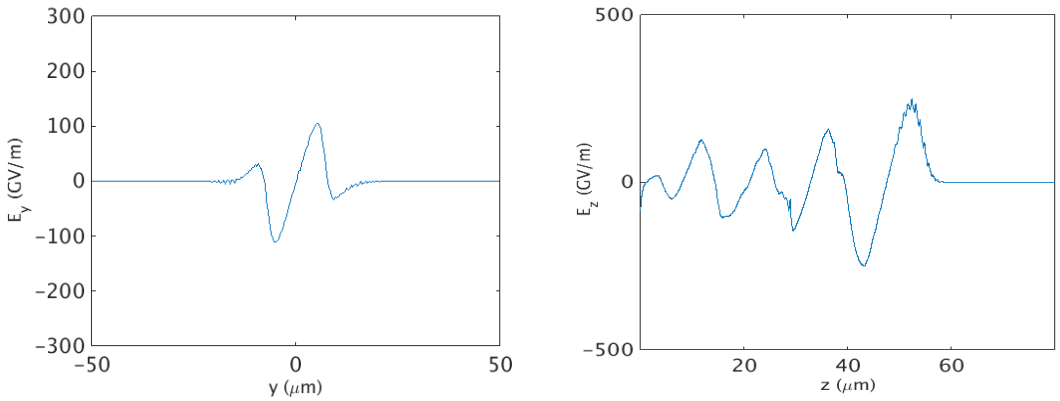


Figure 4.5: Transverse electric field at $z = 44\ \mu m$ corresponding to the position of the first bubble (left) and longitudinal electric field on axis of laser propagation (right) at 0.2 ps.

The electrons reach the maximum energy after 3 ps, reaching 132 MeV with a relative energy spread of 13%. The dephasing length predicted by Equation (4.14) is 3 ps in good agreement with the results of the simulation while the energy is lower than the expected maximum of 197 MeV given by Equation (4.17), probably due to the fact $a_0 = 2.8$ is not yet fully in the so called nonlinear regime. Figure 4.6 illustrates the longitudinal phase space at this time point.

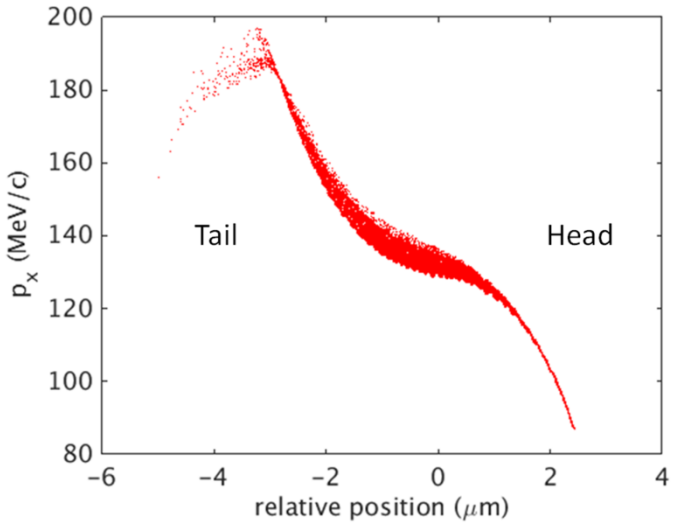


Figure 4.6: Longitudinal phase space of the self-injected electron bunch in the bubble at 3 ps.

With the aim using such system to drive a THz/IR radiation source we considered the possibility to limit the active length of the plasma so that the interaction stops for a beam energy of about 60 MeV. Indeed, after 1 ps, the beam energy is of 56.8 MeV. The 2D electron density is shown in Figure 4.7 and the longitudinal phase space of the injected bunch is displayed in Figure 4.8. The bunch charge of the injected bunch in our simulation is 120 pC, according to Equation (4.19). The current distribution in Figure 4.9 shows the peak current of 10 kA. It is interesting to observe that the relative energy spread is reduced to 5.8% compared to the 3 ps case. The energy spread is due to the fact that the beam has undergone the acceleration in the bubble where the slope of the electric field is large. The energy spread will change with the interaction time in the plasma. The self-injected electron beam typically has small normalised emittance in μm·rad scale thanks to the focussing fields in a bubble and short bunch length about 10s fs. In this case we achieved a normalised emittance of 0.77 μm·rad.

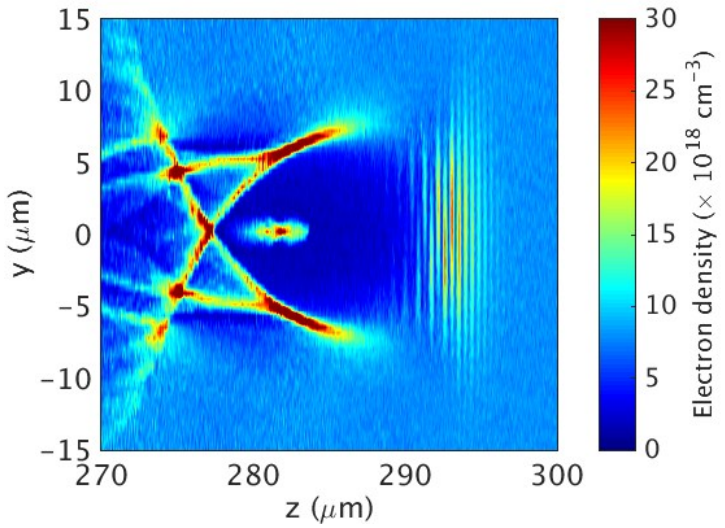


Figure 4.7: 2D electron density at 1 ps.

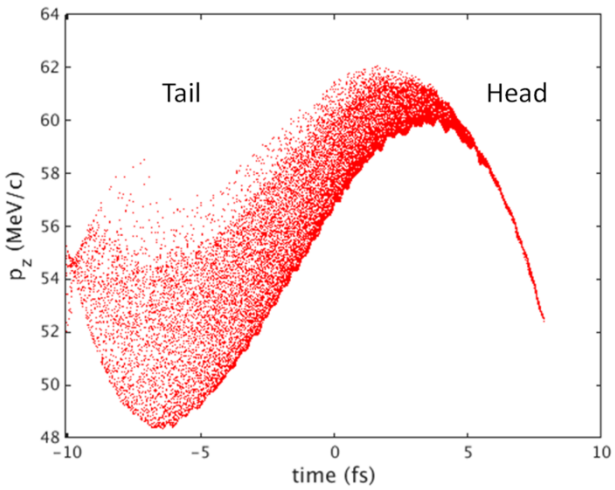


Figure 4.8: Longitudinal phase space of the self-injected electron bunch in the bubble at 1 ps.

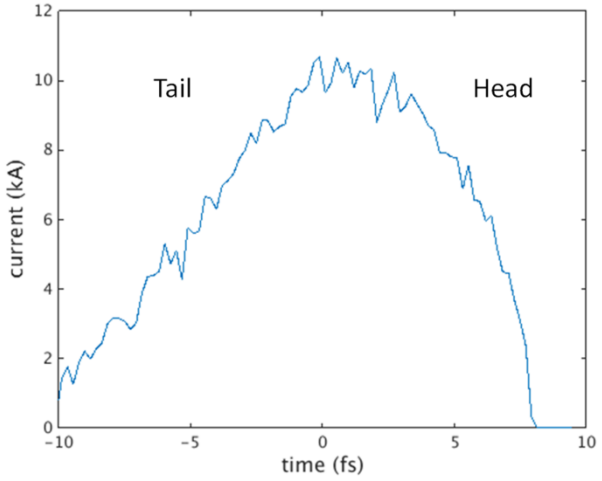


Figure 4.9: Current distribution of the self-injected bunch at 1 ps laser propagation time.

The main parameters of the electron bunch are shown in Table 4.2. The longitudinal phase space distribution of the bunch is imported into Elegant preparing for further investigation of a beam transfer line from the LPWA to the undulator. The divergence of the beam from our simulation is very large due to, in part, abrupt termination of plasma. A huge increase in the transverse beam size of 40 times occurs when transferring the beam through just 1 mm drift space, whereas the bunch length increases to 4.8 fs. The large

divergence and energy spread of the beam make the transporting the beam to undulator and the propagation in the undulator train very challenging.

Table 4.2: Parameters of self-injected bunch from *epoch2d* simulations.

Parameter	Symbol	Value
Beam energy	$\gamma_0 mc^2$	57 MeV
Energy spread	σ_γ/γ	5.8%
Normalised transverse emittance	ε_{nx}	0.77 μm·rad
Geometric emittance	ε_x	6.9 nm·rad
Peak current	I_0	10 kA
rms bunch duration	σ_z	4.2 fs
rms horizontal beam size	σ_x	0.4 μm
rms horizontal beam divergence	$\sigma_{x'}$	17.5 mrad

We have simplified the problem at this stage, assuming that a suitable transfer line can be envisaged and made a preliminary investigation of driving SASE FEL with the self-injected LPWA beam modifying the 6D phase space of the beam with an SDDS function (sddsmatchtwiss) in Elegant to have the Twiss parameters $\beta_{x,y} = 1\,m$ and $\alpha_{x,y} = 0$. With this optics we have a beam size $\sigma_x = 83\,\mu m$ and beam divergence $\sigma_{x'} = 83\,\mu rad$: these values correspond to the same geometrical emittance of ε_x = 6.9 nm·rad of the original beam. Such beam was then used to investigate the THz/IR radiation generation.

In order to drive a SASE FEL in the THz/IR we have selected the undulator parameters according to Equation (1.26) as a planar undulator with period $\lambda_u = 20\,mm$ and gap $g = 4\,mm$. The FEL resonance wavelength is 2.8 μm (107 THz). A preliminary analysis of the FEL gain shows that the estimated 1D Pierce parameter from Equation (1.28) is $\rho = 0.044$ and the gain length from Equation (1.31) is $L_g = 0.022\,m$ ($L_{coop} = 3.08\,\mu m$). These formulae are valid, however, in the limits of an ideal beam satisfying the

conditions in Equation (1.36). The beam parameter shown in Table 4.2, clearly miss the target on the energy spread, expected to be below 1%. Using the more realistic parameterisation of the gain length given by M. Xie [38] to include effects of diffraction, emittance and energy spread the 3D Pierce parameter from Equation (1.34) is $\rho_{3D} = 0.019$ corresponding to a gain length from Equation (1.35) given by $L_{g,3D} = 0.051\ m$ ($L_{coop,3D} = 7.14\ \mu m$). Therefore, our beam with energy spread of 5.8% has a saturation length estimated to $L_{sat} \approx 20 L_{g,3D} = 1.02\ m$.

The peak power at distance z in the undulator from the GENESIS simulation in Figure 4.10 shows that the saturation is not reached within the saturation length $L_{sat} \approx 1\ m$ as predicted. This can be explained due to the fact that the electron bunch length of 4.2 fs or 1.26 µm rms is shorter than the cooperation length, so the radiation pulse slips forward out of the bunch quickly and the interaction between the bunch and the radiation can happen only within a few undulator periods. Therefore, the resultant radiated power is quite low and does not reach saturation even within 10 m along the undulator.

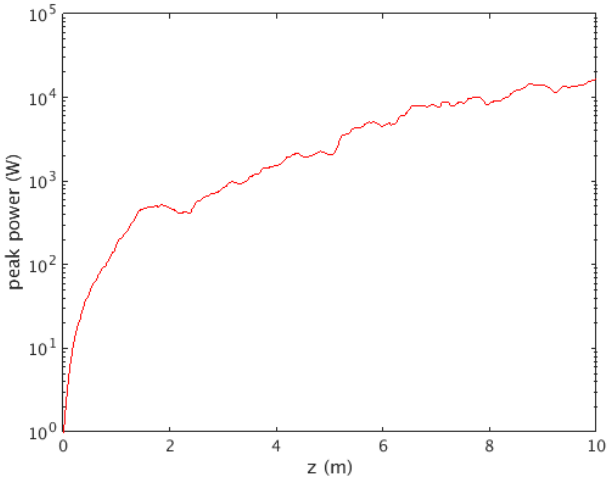


Figure 4.10: Peak power emitted in a planar undulator by the 57-MeV beam from the LPWA.

It is clear from these simulations that the exploitation of such bunches for THz/IR FEL radiation is extremely challenging and requires definite improvement of the properties of the beam in terms of energy spread and bunch length.

Another way to utilise such a short electron bunch is to generate CSR in a dipole. We have investigated the CSR spectrum of the radiation generated in a dipole magnet with the analytical approach used in Chapter 3 based on Equation (1.6). Assuming a dipole magnet of length 0.3 m and bending radius 1.85 m the calculated CSR spectrum are shown in Figure 4.11.

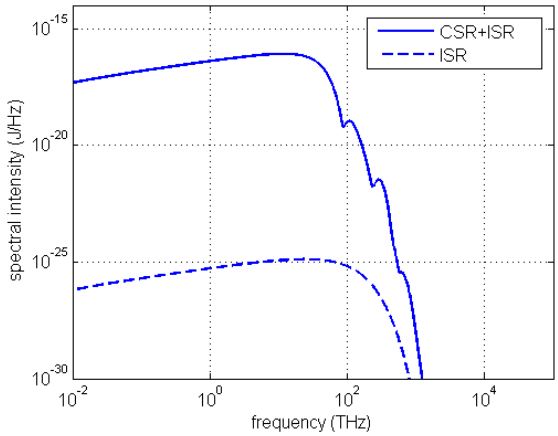


Figure 4.11: Spectrum of total radiation (CSR and ISR) emitted by the self-injected bunch (solid) compared with the spectrum of ISR (dashed) assuming a 0.3-m dipole magnet with bending radius of 1.85 m.

The ISR spectrum extends up to 400 THz since the critical frequency of the dipole radiation is 359 THz for the beam energy of 57 MeV. The CSR spectrum is pushed to cover a broader frequency band due to short bunch duration of 4.2 fs and hence the CSR range extends to ~900 THz taking over the range of ISR. As the bunch profile is not fully a Gaussian distribution, a bump appears at ~120 THz. The CSR generated from the LPWA beam gives a good result which can fulfil our goal to generate short pulse THz/IR radiation.

For the spectrum up to 900 THz, the energy per pulse is 2.8 mJ and the corresponding peak power is 283 GW and average power of 2.8 mW assuming a repetition rate of 1 Hz. For a narrow band spectrum of 0.1 THz about the FEL frequency of 107 THz, the pulse energy is 10.95 nJ which gives peak power of 1.11 kW and average power of 10.95 nW.

4.3 FEL driven by large energy spread beam using a transverse gradient undulator

The self-injected bunch simulated with EPOCH has large energy spread which results in large spread of the radiation wavelength in the undulator. However, the energy spread is correlated with the longitudinal position in the bunch due to the linear dependence of the electric field with the position inside the bubble. It was recently suggested that such a correlation can be exploited to improve the FEL performance by using a special type of undulator known as a transverse gradient undulator (TGU) which is proposed to use with a beam generated by the LPWA [90] [91].

The way to exploit the energy correlation in the longitudinal phase space is to transform it in energy correlation with the transverse coordinate, via dispersion, and introducing at the same time a correlation of the magnetic field and transverse position inside the undulator, i.e. transverse gradient of the magnetic field provided by the TGU. The electrons with different energy experience different magnetic field when they pass through the undulator and hence they can generate FEL at the same resonance wavelength. The TGU is an undulator canted the magnetic poles in transverse dimension, as shown in Figure 4.12, for varying the undulator gap in transverse position. The transverse variation in an undulator gap introduces a gradient of magnetic field. In case of the TGU canted the poles in horizontal, the gradient of the undulator parameter due to the undulator field gradient is given by

$$\Delta K = \alpha K_0 x \tag{4.20}$$

where K_0 is the undulator parameter at the average undulator gap g, x is horizontal position and α is the gradient parameter for a normal conducting planar undulator with cant angle ϕ and undulator period λ_u by

$$\alpha = 2\phi\left(\frac{5.47}{\lambda_u} - 3.6\frac{g}{\lambda_u^2}\right). \tag{4.21}$$

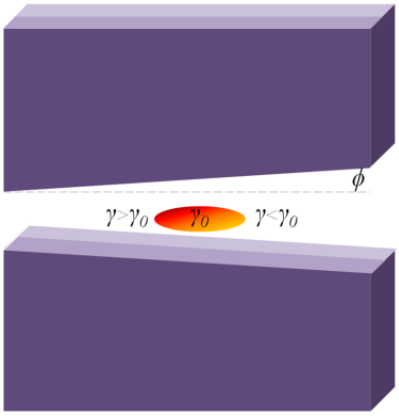


Figure 4.12: An undulator canted the magnetic poles to introduce transverse gradient of magnetic field in the horizontal plane.

To deal with the energy spread effects using the TGU, the beam need to pass the bunch through a dispersive element before travelling into the TGU. The dispersive element, such as a dog leg, will transform the spread of energy in longitudinal phase space into transverse displacement in the bunch. When the beam of average energy $\gamma_0 mc^2$ is dispersed in a way that the horizontal position is $x = \eta\frac{\Delta\gamma}{\gamma_0}$ with the horizontal dispersion given by

$$\eta = \frac{2 + K_0^2}{\alpha K_0^2} \tag{4.22}$$

the electrons with different energy in horizontal position will travel in the TGU and will experience different magnetic field strength such that they all have the same FEL resonance wavelength

$$\lambda_r = \frac{\lambda_u}{2\gamma_0^2}\left(1 + \frac{K_0^2}{2}\right). \quad (4.23)$$

This method shows a great potential to enhance FEL perform by the large energy spread beam.

4.3.1 Analysis of FELs driven LPWA and transverse gradient undulator

In this section, we tried to exploit the idea of the TGU to test whether a SASE THz FEL can be successfully driven by a 57-MeV beam with energy spread of 5.8% generated from the EPOCH simulation presented in section 4.2. The SASE FEL was simulated with a modified version of GENESIS that takes into account the magnetic field of the TGU by adding a linear term of the magnetic field depending on the transverse gradient α. In order to produce feasible canting angle in the TGU based on normal conducting planar undulator we used a transverse gradient $\alpha = 57\ m^{-1}$ corresponding to the cant angle $\phi = 0.12\ rad$, undulator period $\lambda_u = 20\ mm$ and gap $g = 4\ mm$. The dispersion function should be of 2.46 cm, according to Equation (4.22), making electrons with different energy satisfy the resonance wavelength of 2.8 μm or at frequency of 107 THz. Table 4.3 summarises the parameters for the TGU simulation.

The peak power radiated by the LPWA bunch along the TGU (simulated with modified GENESIS) is shown in Figure 4.13 compared with the peak power radiated along the normal planar undulator as shown in Figure 4.10. The transverse gradient enhances the peak power to local maximum over 6 kW at 3.5 m in the TGU but the FEL saturation still cannot be reached within 10 m like using the normal undulator.

Table 4.3: Parameters for generation of SASE FEL using TGU to compensate energy spread effects.

Parameter	Symbol	Value
Beam energy	$\gamma_0 mc^2$	56.8 MeV
Normalised transverse emittance	ε_{nx}	0.77 μm·rad
Peak current	I_0	10 kA
rms bunch duration	σ_z	4.27 fs
rms energy spread	σ_δ	5.8%
Undulator period	λ_u	20 mm
Undulator gap	g	4 mm
Undulator parameter	K_0	2.24
Transverse gradient	α	57 m^{-1}
Horizontal dispersion	η	2.46 cm
Resonance wavelength	λ_r	2.8 μm

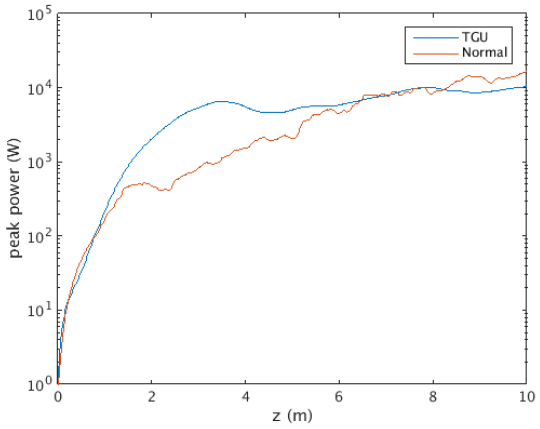


Figure 4.13: The peak power generated by propagating a 57-MeV electron beam with energy spread of 5.8% along TGU and normal planar undulator.

Looking at the FEL radiation in the undulator after a length of 3.5 m, we notice that the use of the TGU produces a cleaner and sharper spectrum around the resonance frequency as seen in Figure 4.14.

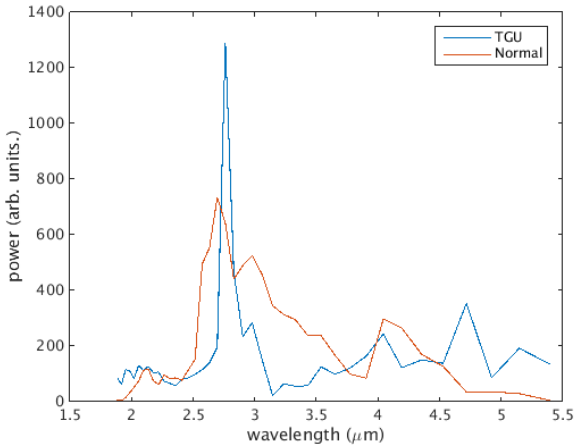


Figure 4.14: Spectrum of radiation generated by TGU and normal planar undulator at undulator length of 3.5 m.

In order to check whether lower energy spread would improve the radiation properties we also investigation on the effects of energy spread using a Gaussian electron beam generated with Elegant having almost similar beam parameters as the LPWA beam simulated with EPOCH but with the energy spread of 1%. The results are shown in Figure 4.15 and 4.16.

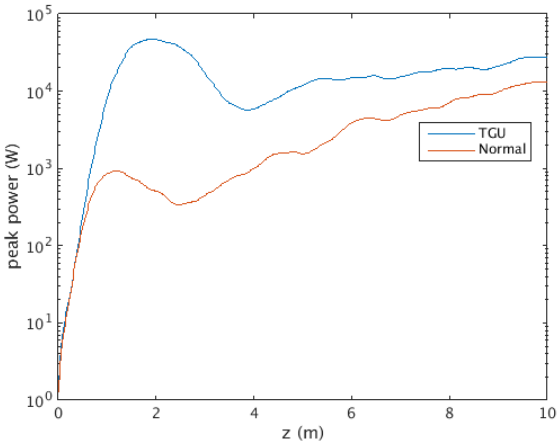


Figure 4.15: The peak power along TGU and normal planar undulator emitted by a 57-MeV beam with energy spread of 1% simulated with Elegant.

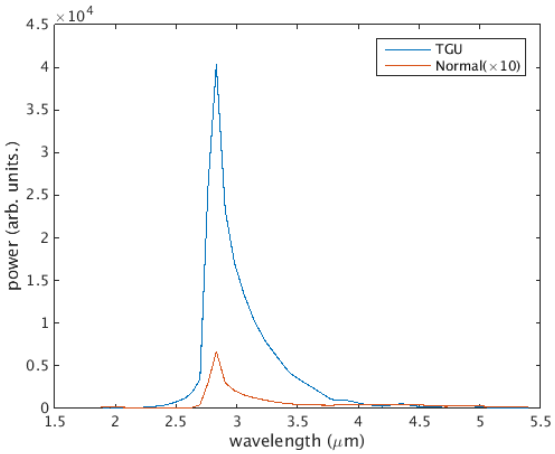


Figure 4.16: Spectrum in TGU and normal planar undulator at undulator length of 2 m emitted by a 57-MeV beam with energy spread of 1% simulated with Elegant.

Results of the 1% energy spread beam shows that, in case of the normal undulator, the peak power reaches a local maximum of ~1 kW at 1.2 m undulator length and after 2 m the power is comparable to the power emitted by the 6% energy spread beam. A clear improvement is clearly seen in case of the TGU. The local maximum of the peak power is at 2 m, almost half of the length that the high energy spread beam reaches the local maximum, and also the power is an order of magnitude higher. The spectra from the lower energy spread beam for both TGU and normal undulator have a clearer peak at the resonance wavelength of 2.8 μA compared with the spectra from the high energy spread beam. The spectrum of TGU from 1% spread, however, is broader.

Even though the FEL saturation cannot be reached, the TGU demonstrates potentials to improve FEL performance of electron beams generated by the LPWA in nonlinear bubble regime as supported by our results in both high and low energy spread cases. It is clear that the main limitation in achieving SASE THz FEL gain and saturation depends on the very short bunch length as compared to the FEL cooperation length of and the slippage effect discussed in the previous paragraph.

As a final study, we have used the TGU idea increasing the electron beam energy in order to shift the FEL resonance wavelength and the cooperation length to values much shorter than the electron bunch length, so that the aforementioned pulse propagation effect are diminished.

By assuming beam qualities which consist of moderate improvements on what can be currently achieved by the LPWA, we have done a GENESIS simulation by using a 750-MeV beam generated with Elegant [92], with energy spread 1%. The beam parameters are summarised in Table 4.4. The FEL radiation is now 4.67 nm, compared to the bunch length 1.5 μm (i.e. 5 fs).

Table 4.4: Parameters for 750-MeV electron beam generated with Elegant and undulator parameters used in GENESIS simulation for this case.

Parameter	Symbol	Value
Beam energy	$\gamma_0 mc^2$	750 MeV
Normalised transverse emittance	ε_{nx}	0.1 μm·rad
Peak current	I_0	10 kA
rms bunch duration	σ_z	5 fs
rms energy spread	σ_δ	1%
Undulator period	λ_u	10 mm
Undulator gap	g	1.5 mm
Undulator parameter	K_0	1.42
Transverse gradient	α	150 m^{-1}
Horizontal dispersion	η	1.32 cm
Resonance wavelength	λ_r	4.67 nm

GENESIS results for this case are shown in Figure 4.17 and 4.18. The FEL saturation is achieved within 5 m using the TGU with transverse gradient 150 m^{-1} and the saturation power is 8 GW, almost one order of magnitude improvement from the FEL using

the normal undulator. The spectrum from the TGU shows a sharper peak at the resonance wavelength compared to the spectrum from the normal undulator. The TGU also gives the radiation in the higher harmonics with significant power as shown in Figure 4.19.

As can be seen, the TGU concept is very effective in increasing the FEL power but the wavelength range under consideration is well outside the THz/IR range that is the main theme of this thesis.

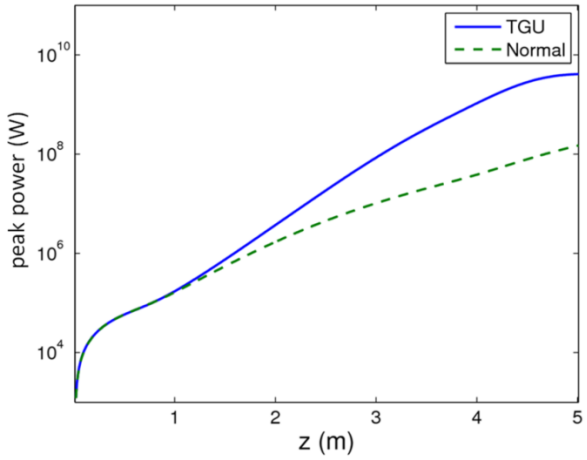


Figure 4.17: Peak power along the undulator radiated by the 750-MeV beam with energy spread of 1% in normal undulator and TGU.

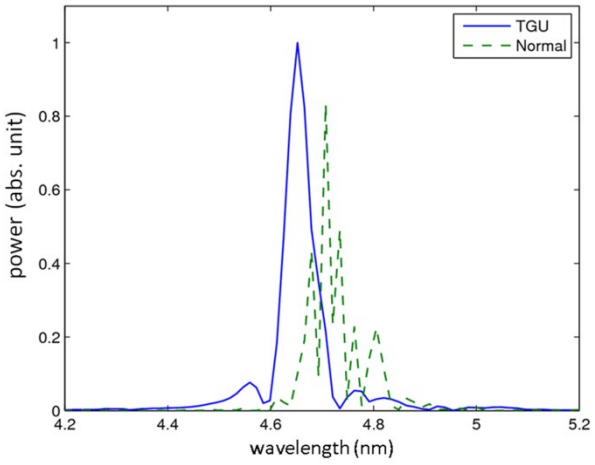


Figure 4.18: Spectrum of SASE FEL generated by a 750-MeV beam with energy spread of 1% at 5 m in normal undulator and TGU.

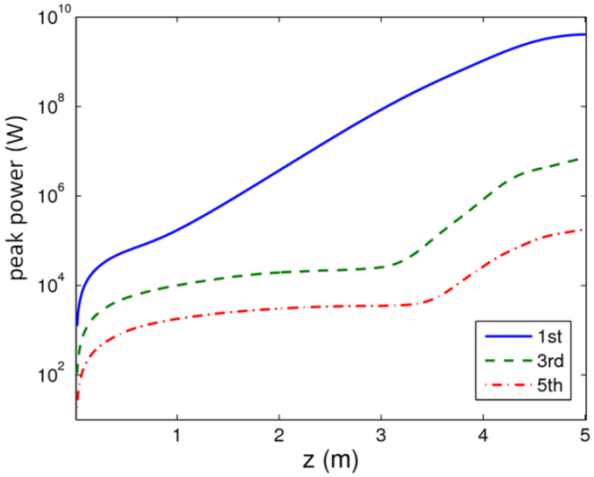


Figure 4.19: Peak power of SASE FEL generated with TGU in the fundamental, third and fifth harmonics.

Future perspective for full start-to-end simulation

We discussed the generation of the self-injected bunch with the LPWA in bubble regime in section 4.1 and preliminary attempts to use this bunch for driving a FEL in section 4.2. We have shown that the beam qualities generated by the LPWA pose very strong challenges already in a simple transport channel for transferring the beam from the LPWA to the undulator, mostly due to the large beam divergence of the LPWA beam. A basic layout of the FEL source driven by the LPWA is displayed in Figure 4.20.

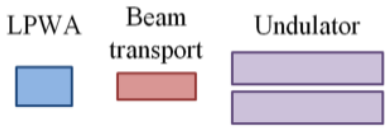


Figure 4.20: Layout of LPWA-based THz/IR source.

The realistic profile of the plasma density, in particular, tapering the plasma density at the exit of the LPWA should be included into simulations to decrease the beam divergence. In order to focus the beam, strong focussing, for instance, by quadrupole

triplets at the beginning and at the end of the system is necessary and a dogleg consisting of two dipoles with opposite bending angle is also needed to give the beam appropriate dispersion for application of the TGU to deal with large energy spread beam as presented in previous section. A transfer line for 120-MeV electron beams generated by a laser wakefield accelerator to the TGU was also designed by a group in Jena [93]. Their beam however has smaller divergence of 2.5 mrad than our beam divergence from the simulation. The potential range of energy spread and beam divergence should be lower than 1% and 5 mrad respectively. The beam transport simulation should be studied further to obtain a suitable transfer line for the THz/IR FEL source driven by the LPWA beam.

4.4 Summary

In this chapter, compact THz/IR radiation sources driven by the LPWA technology were discussed. First, we explained backgrounds of the LPWA in nonlinear bubble regime and generation of electron bunch in the bubble by self-injection method. Second, a simulation of the LPWA in bubble regime with EPOCH was presented and we also show FEL and CSR radiated by the electron beam from the LPWA simulation. Third, the TGU was introduced for making electrons with large energy spread to satisfy the same FEL resonance frequency.

The simulations of the LPWA were performed using the parameters of commercially available lasers and the beam energy targeted to generated radiation in THz/IR. We presented simulations for self-injected bunch at beam energy of 56.8 MeV and bunch charge of 120 pC which has an ultra-short bunch duration of 4.2 fs but rather large energy spread of 5.8%. The FEL simulation with GENESIS using the self-injected beam gives the FEL power in kW range and not reaching saturation due to the bunch length shorter than the resonance wavelength. In case of CSR, the CSR spectrum covers the whole

spectrum of ISR due to low beam energy and ultra-short bunch length. By using a TGU, the FEL power from such large energy spread beam is increased but after 4 m the power is comparable to the undulator without transverse gradient. We investigated further the effect of energy spread by using a tailored beam generated with Elegant having similar parameters as given by the LPWA but reducing the energy spread to 1%. In this case, the radiation power from the undulator is increased by an order of magnitude compared with the case using TGU with 5.8% energy spread.

Studies on generating low energy self-injected beam with lower energy spread and divergence using a tapered density of the plasma and on a beam transport system for transferring the LPWA beam with good parameters to the undulator need to be done further to complete start-to-end simulations of the compact LPWA driven radiation source. The results in this chapter provide an overview of the challenges that will be met in the design of a compact THz/IR source driven by LPWA technology.

Chapter 5

The Accelerator Science Laboratory

In the last years, the John Adams Institute for Accelerator Science (JAI) in Oxford has carried out a number of feasibility studies in order to build an accelerator laboratory with the main aim of providing ultra-short pulse X-ray and THz radiation by a compact linear accelerator or advanced accelerator as LPWAs. The aim is to prove that such radiation sources can be built in small size laboratories like the basement of the Sub-department of Particle Physics in the University of Oxford.

The initial project proposed by the JAI in 2012 [94], was based on the construction of the "Accelerator Science Laboratory (ASL)" hosting a compact linear accelerator based on RF technology and later on a LPWA. The aim of the ASL is to provide new opportunities for accelerator research, including advance and novel accelerator technologies and their applications. Not only university members and staff at JAI, but also students will have access to the advanced accelerator facility within the university campus.

With regards to the production of a short pulse THz source at the ASL, there are two potential accelerator options based on different types of acceleration technology. First, a conventional RF cavity is used as a main accelerating component. After acceleration, the electron bunches are shortened in time in order to achieve short bunch length suitable for production of short pulse THz radiation (see Chapter 3). Second, a novel technology – LPWA – is also considered as a driver of THz/IR FEL. The LPWA can produce electron bunches with ultra-short duration below 10 fs which can radiate short radiation pulses (see Chapter 4).

In this chapter, we present the work done in the investigation of practical aspects of the ASL including design layout, options of the accelerator to be installed and radiation safety. We present the infrastructure of the proposed laboratory area of the ASL and the analysis of the radiation safety of the area.

5.1 Proposal of Accelerator Science Laboratory

A design of the ASL floor plan given in [94] is shown in Figure 5.1. The proposed location is the basement of the Denys Wilkinson Building (DWB) which takes advantage of existing infrastructure available in the area including concrete wall, concrete block for shielding and high ceiling offering more storage and space for ancillary utility. However, the area has limitations on space available, in particular the length of the main laboratory hall is about 27 m. Furthermore, special care in installation of accelerator equipment and radiation safety is required since the surrounding area is used for teaching in the Sub-department. The length constraint can be dealt with by designing a compact accelerator and a study of radiation shielding is essential for radiation protection in the area around the designated location. Design of compact radiation sources and radiation shielding will be discussed in the following paragraphs.

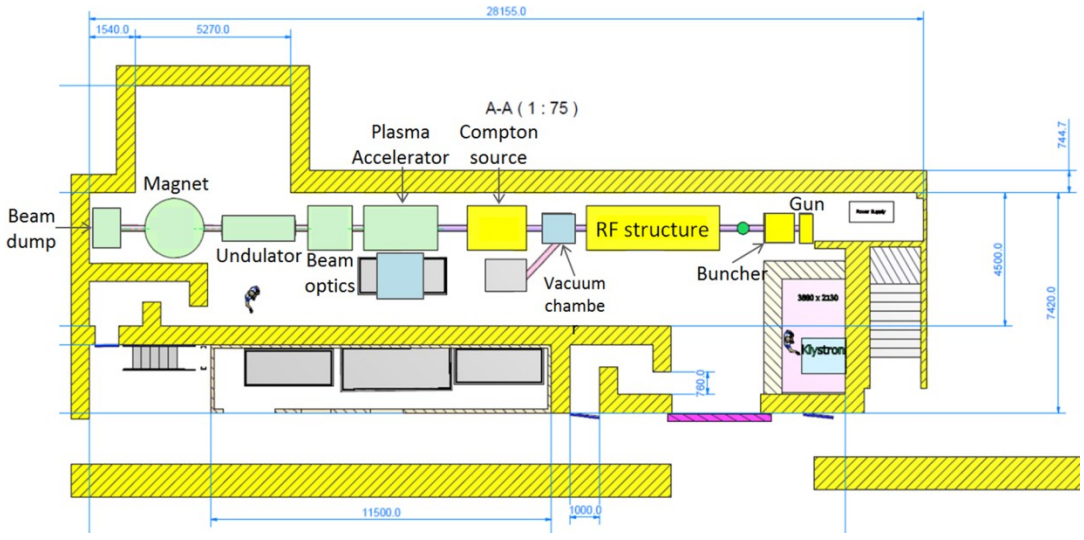


Figure 5.1: Top view of the ASL floor plan [94].

5.2 Design of compact radiation sources for the ASL

The available space in the main area of the ASL as shown in Figure 5.1 should be occupied by an electron accelerator, radiation source and potentially experimental areas. Therefore, the accelerator and the radiation source need to be compact to utilise the space efficiently. According to the proposal of the ASL, one main goal is to provide short pulse THz radiation. Typically, the radiation in THz frequency range can be produced by the electron accelerator-based sources with electron beam energy not as high as the sources for X-ray production. This gives us more relaxed conditions for the accelerator design. Potential choices of accelerators for the ASL are an RF linac and LPWA.

THz source driven by RF linac

We presented the design of RF linac based THz radiation source in Chapter 3 with two options of radiation generation: FEL from an undulator and CSR produced by a dipole. The design for both options is shown in Figure 5.2.

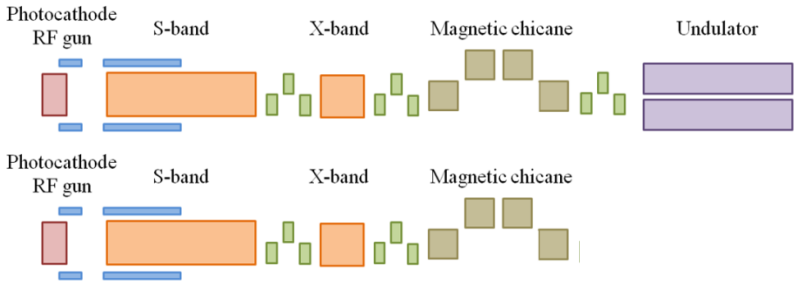


Figure 5.2: Layout of compact RF driven THz sources: FEL (top) and CSR (bottom). Components in blue are solenoids and in green are the quadrupoles.

Start-to-end simulations using a 500-pC bunch show that the FEL at 6.46 THz (46.45 μm) with the peak power of 1.5 MW and average power of 726 μW (according to photon pulse of 2.07 ps) assuming 100 Hz repetition rate can be generated by passing an electron beam with energy of 17.5 MeV and rms bunch duration of 0.7 ps into the 5-m

undulator. In the CSR case, the spectrum emitted from 53.2 MeV beam of 126 fs rms bunch duration covers the frequency 16 THz. For a bandwidth of 0.1 THz around 6.46 THz, the CSR peak power is 1.7 MW and average power is 51 μW assuming 100 Hz repetition rate.

Length of the source from RF gun to the end of bunch compressor is10.5 m and the 5-m undulator suffices for generation of THz radiation.

THz/IR source driven by LPWA

The THz/IR FEL driven by the LPWA was presented in Chapter 4 taking advantage of the high accelerating gradient to reduce the length occupied by the radiation source as shown in Figure 5.3.

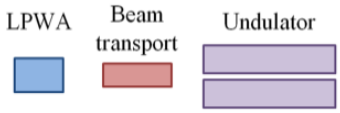


Figure 5.3: Layout of THz FEL driven by LPWA.

2D PIC simulations were done to produce an electron bunch from self-injection in the LPWA operated in nonlinear bubble regime. As the self-injected LPWA beam typically has large energy spread, the TGU can be used to enhance the FEL performance. The FEL simulations show that 57-MeV beam with relative energy spread of 6% can generate near infrared (NIR) FEL, within 4 m of the undulator length, the peak power of 1 kW using a normal planar undulator and 6 kW using the TGU. By reducing the energy spread to 1%, the peak power from the TGU is increased to about 50 kW.

The length of the LPWA is quite short, less than 0.5 m, and the undulator length as derived from the simulations is 4 m. The variation of the total length is then determined by the beam transport system. Chapter 4 highlighted some technical difficulties in the design of an effective transfer line for such beam quality and decisive improvements are needed,

especially in the control of the energy spread. We estimated, however, that a reasonable transfer line length for low-energy electron beams (<100 MeV) could be in the order of 5 m. Therefore, the total LPWA-driven FEL should be about 10 m. The radiation safety of the ASL will be presented in next section.

5.3 Radiation safety of the ASL

Electrons propagating through matters lose their energy by collision and radiation. The radiation is known as bremsstrahlung, which results in photons emitted when the electrons are scattered or decelerated by the electromagnetic fields of nuclei in matter. The energy loss rate due to bremsstrahlung increases linearly with the electron beam energy, while the collision loss rate is logarithmically proportional to the beam energy. The electron beam energy at which the loss rate of collision and bremsstrahlung are equal is defined as the critical energy

$$E_c \approx \frac{800\ MeV}{Z+1} \tag{5.1}$$

where Z is the atomic number of the matter the electron traverses.

When electrons from the accelerated beam and the photons generated from bremsstrahlung incident on an absorber such as a beam dump or accidentally on other components, an electromagnetic shower is initiated by bremsstrahlung and pair production that generates electrons and positrons. These electrons and photons with lower energy than the primary electrons from the accelerating beam continue the electromagnetic shower further and generate more electrons and photons, dissipating their energy in the absorber both longitudinally and radially until the electron energy falls below the critical energy. The distance traversed by the electrons and photons in matter is characterised by the radiation length, given approximately by [51]

$$X_0 = \frac{716.4A}{Z(Z+1)\ln(287/\sqrt{Z})} \tag{5.2}$$

where A is the matter's atomic mass. The longitudinal length after which 99% of the initial electron beam energy E_0 is absorbed is expressed as [95]

$$L_{99\%} = (1.52\ln(E_0[MeV]) - 4.1\ln(E_c[MeV]) + 17.6)X_0. \tag{5.3}$$

In radial dimensions, the distribution of the electromagnetic shower is characterised by the Moliere radius [96]

$$R_M \approx \frac{E_s}{E_c} X_0 \tag{5.4}$$

where the scale energy $E_s = \sqrt{4\pi/\alpha} m_e c^2 \approx 21.2\ MeV$, the fine structure constant $\alpha = 1/137$ and 99% of the electron beam energy is contained within the radial distance

$$R_{99\%} = 3.5R_M. \tag{5.5}$$

In high energy electron accelerators, neutrons can also be generated by photonuclear reactions. The main mechanism for generating neutrons is the giant dipole resonance, which is caused by photons of energy from approximately 10 to 30 MeV. Electromagnetic fields of photons excite a nucleus and induce collective vibration of protons against neutrons by increasing the dipole moment. If high enough energy is transferred from photons to the nucleus, neutrons can be separated and emitted from the nucleus.

From the above, the main radiation sources in an electron accelerator are electrons, photons and neutrons. In order to control all these hazardous radiation sources, the shielding of the accelerator enclosure must be capable of absorbing them. For this purpose it turns out that the most effective way for the radiation shielding in our accelerator design is to build a dedicated beam dump, while the external shieling of the enclosure can take care of the residual radiation that can be generated in the accelerator. The electron beam

dump should be designed to be longer than $L_{99\%}$ and have lateral extension covering more than $R_{99\%}$ so that it absorbs all radiation sources, mainly generated by electromagnetic showers, and the residual radiation is contained by the enclosure of the beam dump and can be further captured by the shield walls. Particles and radiation are mainly generated inside the beam dump, but also in some locations of the accelerator or possibly be the result of mis-steering of the beam, which produces an extended region of beam losses along the vacuum pipe.

5.3.1 Quantities related to radiation protection

The physical quantities which are used to characterise the radiation protection are as follows [51]:

Absorbed dose D (Gy) is the energy from ionising radiation absorbed by a material per unit mass.

Organ absorbed dose $D_{T,R}$ (Gy) is the energy absorbed in an organ or tissue T with mass m_T generated by a specific type of radiation R defined by

$$D_{T,R} = \frac{1}{m_T} \int_{m_T} D dm \tag{5.6}$$

Equivalent dose H_T (Sv) is the sum of organ absorbed dose $D_{T,R}$ in a specified tissue T caused by various radiation types R expressed as

$$H_T = \sum_R w_R \, D_{T,R} \tag{5.7}$$

with different weighting factors w_R recommended by the International Commission on Radiological Protection (ICRP) [97] which is unity for electrons and photons and varies with the beam energy in case of neutrons.

Ambient dose equivalent $H^*(d)$ (Sv) at a point in a radiation field is the dose equivalent produced by the radiation field in a sphere of 30 cm diameter made of tissue-equivalent plastics with unit density ($1\ g/cm^3$) at a depth d in such sphere on the radius opposing direction of the field. This sphere is used to approximate the human body. The ambient dose equivalent is normally considered at 10 mm depth. The ambient dose equivalent is a fundamental quantity for monitoring radiation in specific areas and most instruments for radiation protection are calibrated to measure this quantity.

5.3.2 Radiation levels

In normal circumstances, there is a certain level of background radiation due to radioactive materials in the nature, cosmic-rays from outer space and so on. The radiation levels of this background radiation and recommended limits of radiation level for facilities related to radiation are described as follows.

Natural background radiation: the dose equivalent rate in a whole body in most areas over the world ranges from 1 to 13 mSv per year and on average is 2.4 mSv per year.

Cosmic-ray background radiation: the dose equivalent rate due to cosmic ray back ground radiation, mostly from muons, depends on altitude and it is < 0.1 μSv/h at sea level and a few μSv/h at aircraft altitude level.

Cancer induction: the entire population has the cancer induction probability about 5% per Sv [97].

Recommended dose limits: The dose limit recommend in working areas is 20 mSv per year in EU countries and Switzerland and it is 50 mSv per year in the USA. For the general public the limit is typically 1 mSv per year. People who work with radiation should not have an annual dose over 20 mSv.

We estimate the annual working hours as 2000 hours and therefore the dose limits of 0.5 μSv per hour outside the accelerator hall during beam on and 10 μSv per hour inside the accelerator hall with beam off are used as the criteria of the radiation shielding study of the ASL.

5.3.3 Simulations of radiation shielding for the ASL

To investigate the radiation safety of the ASL, we performed simulations with FLUKA [98], which is a Monte Carlo code for simulation of interaction and transport of particles. The main construction material is concrete. Due to the proposed location of the ASL in the current building of the Sub-department, the thickness of concrete of the outer laboratory infrastructure is restricted and hard to be modified. Therefore, the study of radiation shielding focussed more on a beam dump and shielding around the beam dump. The study focusses on the accelerator area with a simplified model of the infrastructure, including side walls, floor and ceiling modelled following the design of the ASL (Figure 5.1). The design of the beam dump and shielding around the beam dump was optimised in order to achieve the dose rate below the limit but maintaining acceptable size and weight.

The beam parameters assumed in the radiation safety calculations are the ones used in most of the simulations in Chapter 3 and 4. The electron beam energy is below 100 MeV, however, for contingency and future upgrade, we assume a Gaussian electron beam of energy 500 MeV. The bunch charge is 0.5 nC and the repetition rate of 100 Hz, so that

the beam intensity is 3.12×10^{11} particles/s. We also assumed a relative momentum spread of 1%, beam size of 0.5 mm and beam divergence of 0.01 mrad.

The infrastructure is made of concrete with density $\rho = 2.34\ g/cm^3$. The concrete thickness of the side walls is 80 cm, of the floor it is 100 cm and of the ceiling it is 50 cm. The concrete shielding in the accelerator area of the ASL is shown in Figure 5.4.

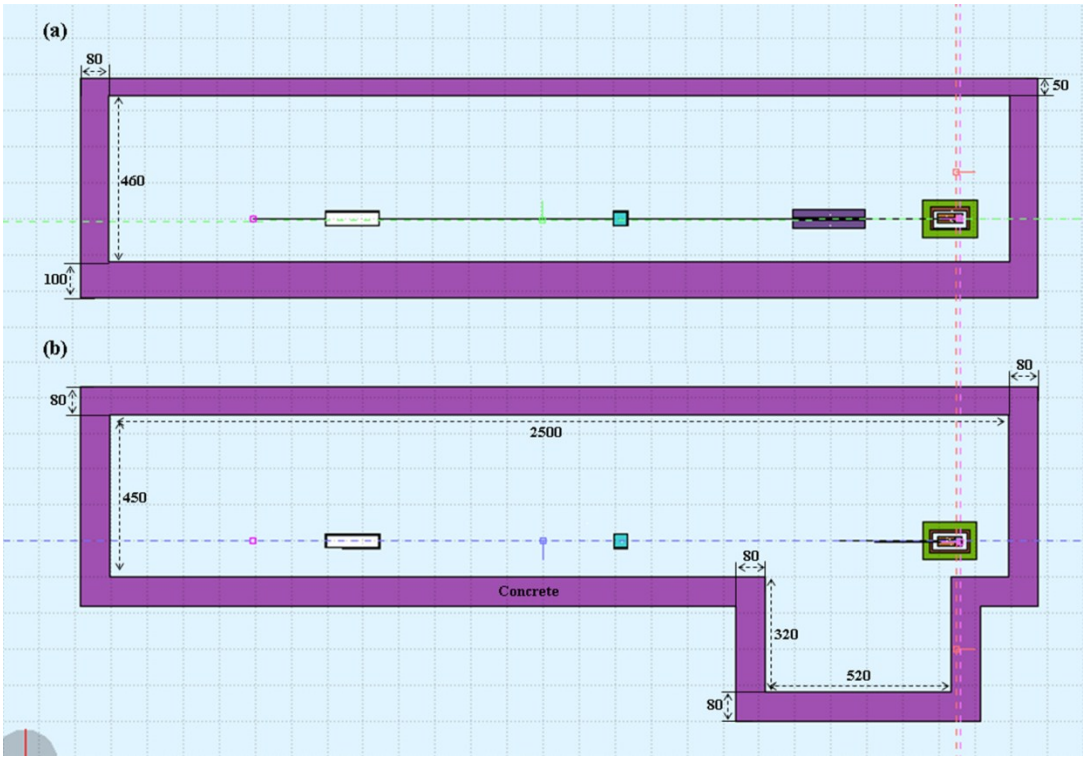


Figure 5.4: Side view (a) and top view (b) of the accelerator area of the ASL in FLUKA simulation. The concrete shielding is in purple. The accelerator elements and the beam dump are also shown. All dimensions are given in cm.

The accelerator beam line in the FLUKA model consists of beam pipe, RF linac, plasma chamber, undulator and beam dump as can be seen in Figure 5.4. The beam pipe is made of stainless steel with inner radius 1 cm and the thickness of the pipe equals 0.2 cm. The RF linac is modelled as a copper cylinder of 4 m long, inner radius of 18 cm and thickness of 2 cm. The plasma chamber is a stainless steel box of inner dimension of

$36\ cm \times 36\ cm \times 36\ cm$ and thickness of 2 cm. The undulator is modelled as a couple of 2-m long magnets placed on top and bottom of the pipe 2 cm away from the pipe axis. Each array of the undulator is 40 cm wide and 20 cm high and the material is assumed to be NdFeB with a density of $7.5\ g/cm^3$. Inside beam pipe and RF linac is vacuum, whereas the plasma chamber is filled with hydrogen gas.

The beam dump has to be designed to absorb 99% of the beam energy by having the longitudinal and radial dimension more than $L_{99\%}$ and $R_{99\%}$, respectively. The beam dump was chosen to be in a cylindrical shape reflecting the beam symmetry. The beam dump has three components: cylindrical core made of graphite, copper outer cylindrical shell covering the core, and lead disk at the bottom end. Graphite was chosen due to its low atomic number to reduce equilibrium temperature as a result of the beam dump [95] and low linear expansion coefficient resulting in low mechanical stress in the beam dump structure. Copper has low thermal resistance, so the heat can be transferred out of the beam dump rapidly, for this reason it was used in the outer cylinder. Lead has a short radiation length which can be used to shorten the total length of the beam dump, and was most effectively used at the end of the dump to stop particles and radiation.

Shielding around the beam dump was included in the design to contain the radiation, reducing the dose rate outside the accelerator area below the limit. The shielding consists of two components, which are the inner iron box and outer polyethylene box. Iron ($\rho = 7.87\ g/cm^3$) is one of the high atomic number materials which can shield photons effectively. Neutrons are shielded by using high hydrogen content materials like water or concrete. We chose polyethylene ($\rho = 0.94\ g/cm^3$) instead of concrete which is a common shielding material because it is lighter than concrete.

Dose equivalent rate of radiation generated during beam operation known as prompt radiation and residual radiation generated by radioactive materials after the beam operation was investigated in Monte Carlo simulations done with FLUKA. The residual dose equivalent rate was estimated, assuming the accelerator has been operated for 40 hours continuously, for decay times of zero second (or when the beam is terminated), one hour and eight hours after the beam operation.

Optimisation was done by using length, radius and thickness of each component in the beam dump and the shielding as optimising parameters targeting to have the dose equivalent rate of the prompt radiation outside the accelerator hall below 0.5 μSv/h and the dose equivalent rate of the residual radiation inside the accelerator hall below 10 μSv/h. The optimised design is shown in Figure 5.5. The properties of the materials used in the design are given in Table 5.1. Total length of the beam dump is $2.4L_{99\%}$ and the beam dump radius is $6.4R_M$. The beam dump weighs 0.45 tons and the shielding is 4.29 tons. Note that the top inner shielding is thicker in order to compensate the ceiling concrete slab which is the thinnest compared with side walls and floor slab.

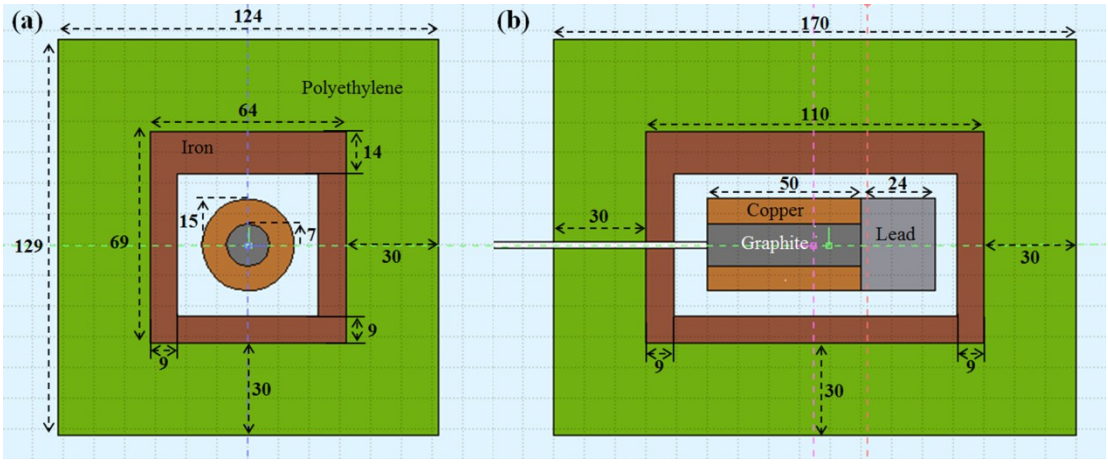


Figure 5.5: Front view (a) and side view (b) of the optimised design of the beam dump. All length is given in cm.

Table 5.1: Properties of materials used in beam dump design for the ASL.

Material	$\rho\ (g/cm^3)$	X_0 (cm)	E_c (MeV)	R_M(cm)	$L_{99\%}$ (cm)
Graphite	1.71	25.1	84.25	6.32	249.02
Copper	8.96	1.44	20.17	1.51	22.73
Lead	11.35	0.56	7.33	1.62	11.16

2D projections of the dose equivalent rate of prompt radiation are shown in Figure 5.6. The radiation can be mainly contained within the accelerator hall but the dose equivalent rate in the areas above the ceiling and below the floor exceed the public limit of 0.5 μSv/h. The radiation going to the floor can be absorbed further by the earth under the building. The more critical areas are above the ceiling and behind the wall downstream the beam. Fortunately, the average dose equivalent rate in these two locations is confirmed to be well below the public limit as shown in Figure 5.7. These results demonstrate that the beam dump, the shielding covering the beam dump and the concrete walls are adequate to contain prompt radiation in the accelerator hall.

In case of residual radiation inside the hall with beam-off, the dose equivalent outside the shielding around the beam dump is lower than the limit for radiation workers of 10 μSv/h for the decay times longer than one hour as seen in Figure 5.8. This suggests that the ASL accelerator room can be safely accessed just after the beam is switched off for an hour.

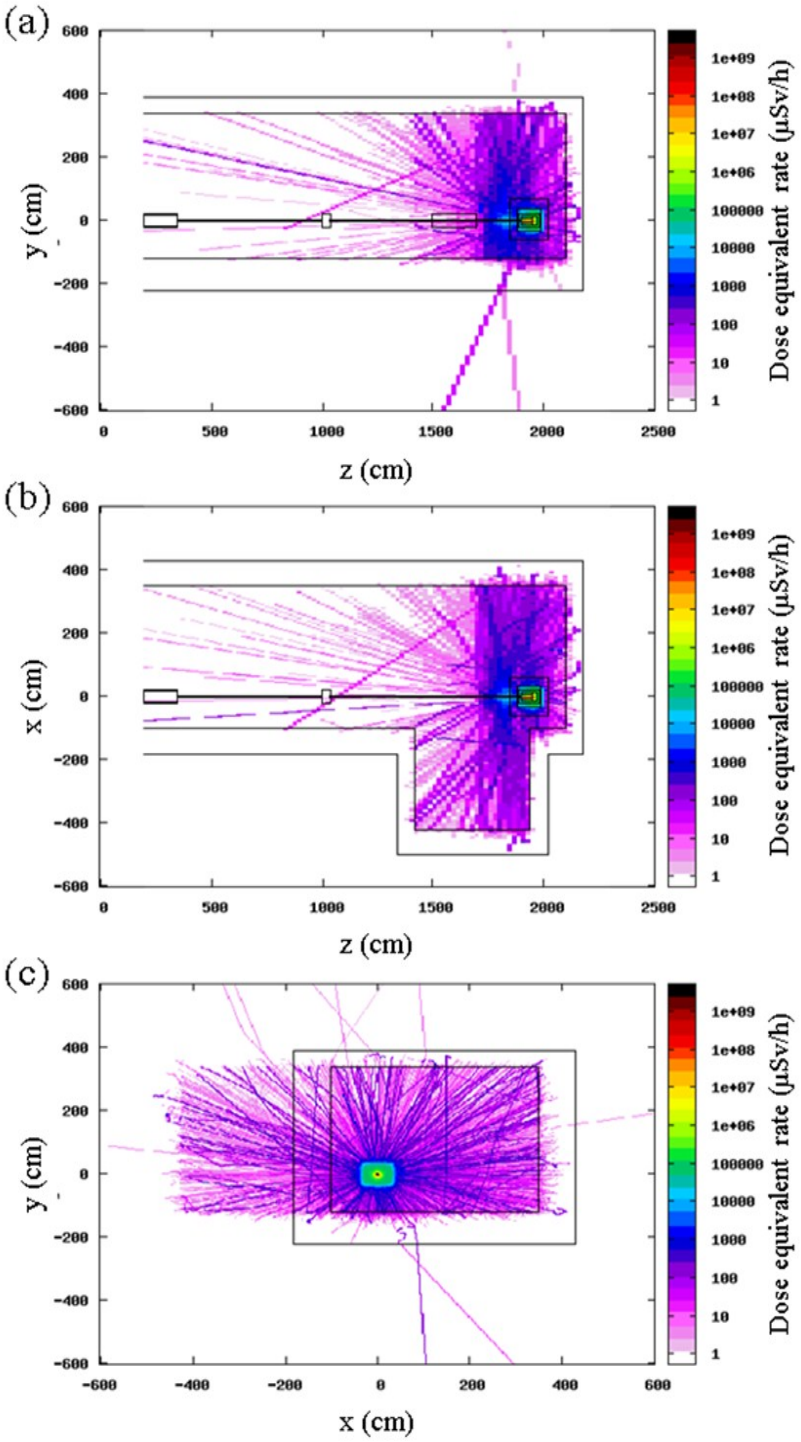


Figure 5.6: 2D dose equivalent rate shown in three directions: side view (a), top view (b) and direction facing the beam (c) in the accelerator room of the ASL from FLUKA simulations. The minimum of colour scale shown is at 0.5 µSv/h.

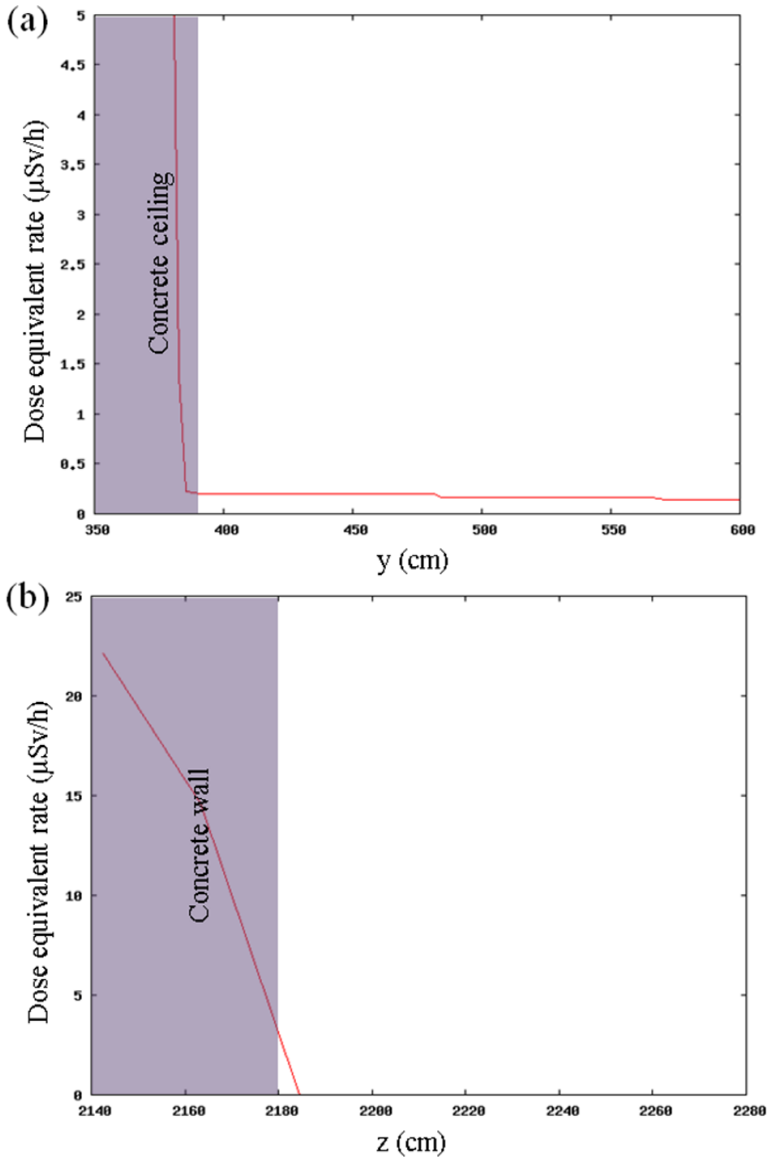


Figure 5.7: Prompt dose equivalent rate averaged over the area (a) above concrete ceiling on top of the beam dump and (b) behind concrete wall in the beam direction. The area behind the concrete wall that the beam is directed towards includes 3 m distance from the beam axis in horizontal and vertical plane, and the area above the ceiling covers 3 m distance from the beam axis in the horizontal plane and 3 m on axis above the beam dump and shielding.

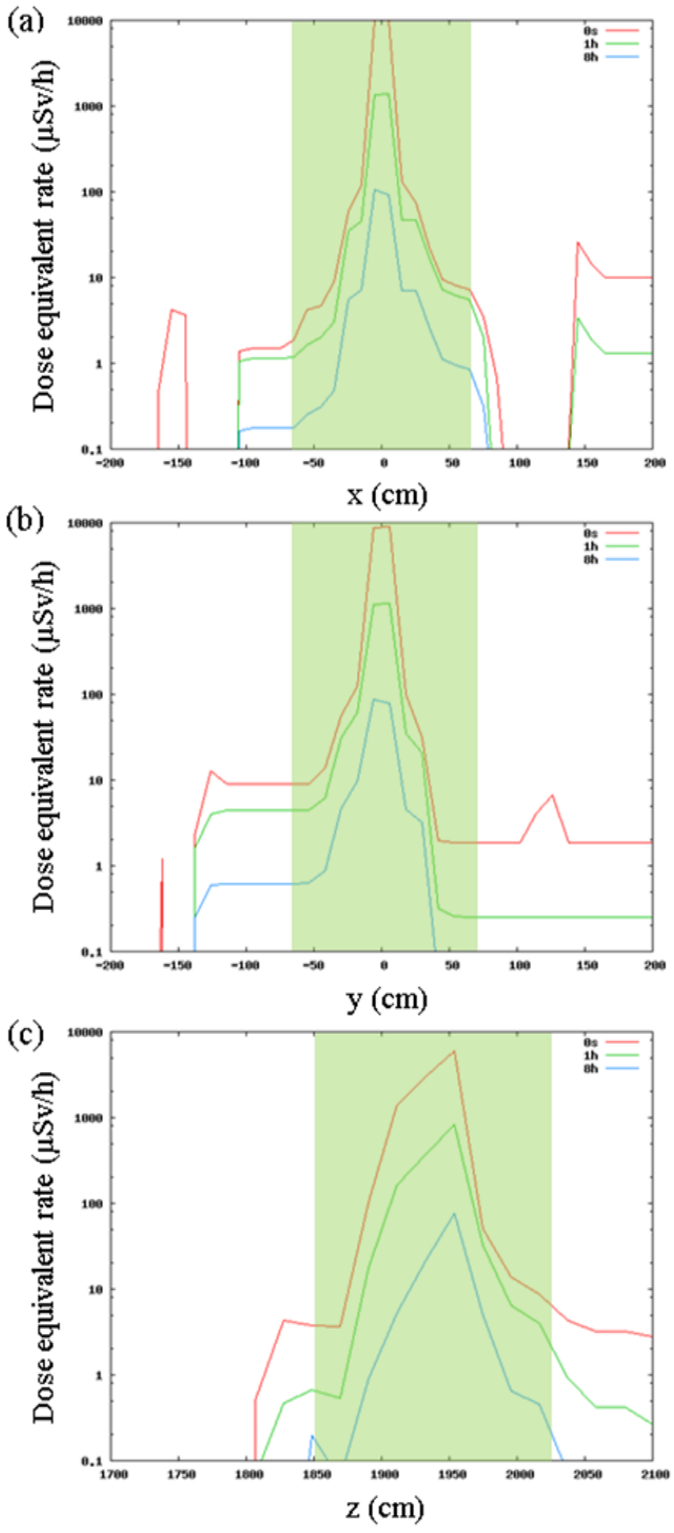


Figure 5.8: Residual dose equivalent rate inside the accelerator area in horizontal (a), vertical (b) and longitudinal (c) direction at time the beam terminated (0s), and after beam operations for one hour (1h) and eight hours (8h). Shaded green area shows the region occupied by the dump shielding.

5.4 Summary

The ASL is a project aiming to become an advanced accelerator laboratory in the Sub-department of Particle Physics in the University of Oxford. We have studied the designs of the compact THz radiation sources based on the RF linac and the LPWA in the previous chapters, which can be considered as potential options to be established in the ASL.

Radiation safety of the ASL was also investigated in order to control the radiation levels inside and outside of the ASL accelerator room. The radiation shielding simulations were conducted assuming the electron beam energy of 500 MeV, bunch charge of 0.5 nC and repetition rate of 100 Hz with FLUKA. Due to the difficulties of modifying the infrastructure of the proposed area, the study focusses on specifically designing the beam dump and the shielding around the dump to provide adequate radiation levels and having acceptable physical properties. Both the beam dump and shielding weigh 4.74 tons, the total length is 1.7 m and the lateral size is 1.24 m in the horizontal and 1.29 m in the vertical directions. The Monte Carlo simulations with FLUKA show that the design of the beam dump and the shielding can provide sufficient radiation protection for the public area outside the accelerator hall from the prompt radiation during beam operations and to provide radiation safety for the workers from the residual radiation in the hall after beam-off for an hour.

Other aspects, such as radiation levels due to beam loss, mechanical stress and material expansion could be studied further and combined with this study to provide a more complete view of the ASL.

Chapter 6

Conclusion

The notable characteristics of THz radiation, non-ionising, non-invasive and non-destructive, have allowed numerous applications across different disciplines, for instance, weapon detection for security scanning, coating thickness measurement for drug quality assurance, skin cancer examination, and telecommunication at high altitude. The radiation range of 0.3-10 THz is hardly accessible by conventional devices like semiconductor lasers and hence THz sources based on accelerators are continuously proposed to generate THz radiation which does not only produce high power but also short pulse length. This thesis presents the research work focussing on ideas generating short pulse THz radiation from storage rings in a dedicated operating mode and from compact linacs based on RF linacs and LPWAs. Advantages of producing THz radiation in such large-scale storage rings are ability to provide the radiation for many beamlines simultaneously, while compact linacs require smaller space which can be installed in university laboratories.

6.1 Generation of Short Pulse THz Radiation with Storage Rings

The natural or zero-current bunch length in storage rings is proportional to square root of momentum compaction factor which can be manipulated by tuning the lattices. The Diamond storage ring has been operated in low-alpha mode for generating CSR at wavelength longer than bunch length of the nominal user modes. In this work, we investigated a new operating mode, the so-called “ultra-low alpha mode” pushing the momentum compaction factor to lower possible value by performing particle tracking of a single bunch with the numerical code *sbtrack* using an impedance model consisting of

resistive wall, BBR and CSR with shielding effects. The shunt impedance and resonance frequency of the resonators were determined by the comparison of tracking results with the measurements taken from a trial run of ultra-low alpha mode at Diamond. The best qualitative agreements between the simulation and the measurement, reproducing the bunch lengthening measured with streak cameras, the spectrograms plotted from turn-by-turn data from SBDs and the FTIR spectrum of average CSR signals measured with FTIR interferometer on the beamline B22, were obtained using an impedance model with two resonators: low-frequency resonator ($f_l = 8.3\ GHz, R_l = 0.5\ k\Omega$) which is used in the analysis of Diamond standard optics and high-frequency ($f_l = 100\ GHz, R_l = 90\ k\Omega$). The CSR spectral range is extended to cover frequency of 1.6-2.0 THz by operating Diamond storage ring with ultra-low alpha.

6.2 THz Radiation and Short Pulses with an RF Linac

A compact THz radiation sources using an RF linac to accelerate the electron beams was designed and start-to-end simulations of a 500-pC bunch from beam generation to radiation generation were performed in FEL and CSR cases. The electron bunch in RF linacs can be shortened by using a bunch compression technique applicable by a dispersive element like a 4-dipole chicane. The compressed bunches were used to drive short-pulse FEL and CSR in THz spectral range. The main components of the accelerator are the photoinjector, the S-band booster linac, the X-band cavity and the magnetic chicane. An undulator is located next to the chicane to drive FEL, while CSR spectrum is calculated at the last bending chicane magnet.

For the FEL, a 17.5-MeV electron beam with rms compressed bunch length of 0.7 ps and peak current of 0.5 kA was simulated and used to generate FEL at frequency of 6.46 THz by a planar undulator with a period of 3.5 cm and a gap of 1.2 cm. The FEL power

saturates within 5 m undulator length with peak power of 1.49 MW and rms pulse duration of 2.07 ps.

For the CSR, the electron beam was used at higher beam energy of 53.2 MeV and was shortened to 0.13 ps with the peak current of 2.5 kA to generate CSR spectrum covering frequency up to 16 THz. The peak power of CSR within bandwidth of 0.1 THz around the frequency 6.46 THz is 1.7 MW.

6.3 THz Radiation and Short Pulses with a LPWA

The radiation source based on LPWAs was studied by performing PIC simulations to generate a self-injected electron bunch in a plasma bubble excited by interaction between a laser pulse and plasma. We obtained the electron bunch of 120 pC bunch charge and 4.2 fs bunch length at 56.8 MeV but with relative energy spread of 5.8%. The FEL saturation cannot be reached within a 10-m long undulator because the bunch is shorter than the FEL cooperation length. The SASE FEL operation is prevented by the large energy spread and by strong slippage effects associated to the short bunch length.

In order to compensate the effect of the energy spread, we considered a TGU which is an undulator with transverse undulator field variation. The longitudinal energy modulation can be transformed to transverse energy modulation by dispersive element like a dogleg. As a result, electrons with different energies are dispersed transversely. When the dispersion function is set to correspond to transverse gradient of the undulator, the electrons with different energy experience different undulator field strength and as a result, all electrons radiate at the same FEL resonance wavelength.

FEL SASE simulations with the transverse gradient were performed. The results obtained using a TGU with transverse gradient of 57 m^{-1} and the beam with 5.8% energy spread from the LPWA showed that a power in 10 kW range can be generated by the TGU

within 4 m, less than half of the length in the planar undulator without transverse gradient. By reducing the energy spread to 1%, the power can be increased by about 5 times higher at 2 m in the TGU. Investigation with a beam at higher energy of 750 MeV with 1% energy spread demonstrated that the SASE FEL in GW range can be generated in a 5-m undulator with transverse gradient of 150 m^{-1}. All FEL simulations were done by manipulating the beam parameters manually with Elegant to simplify a problem of transporting the large divergence beam obtained from the LPWA simulations.

Further studies on using realistic plasma density profile in the LPWA and the transfer line connecting the LPWA and the undulator are necessary to achieve a complete start-to-end simulation of the THz/IR FEL driven by the LPWA.

6.4 The Accelerator Science Laboratory

The Accelerator Science Laboratory (ASL) is a project presented by JAL in Oxford to build an accelerator laboratory in the Sub-department of Particle Physics in the University of Oxford for providing ultra-short pulse of X-ray and THz radiation driven by a compact linear accelerator or a LPWA. The designated location for the ASL has limited space, in particular the length of the accelerator hall of 27 m, surrounded by departmental areas. This thesis focusses on the compact THz radiation sources. The radiation sources based on RF linac and LPWAs from our studies in Chapter 3 and 4, respectively, were considered as potential design options for the ASL.

The radiation shielding of the ASL was investigated to provide proper radiation safety by performing Monte Carlo simulations with FLUKA with beam energy of 500 MeV, bunch charge of 0.5 nC and repetition rate of 100 Hz for potential future upgrade. We focussed on the design of beam dump and shielding covering the beam dump in order to cope with difficulties to change the infrastructure of the proposed area. Our design of the

beam dump and the shielding, 4.74 tons in weight and the external dimensions are 1.7 m long, 1.24 m wide and 1.29 high, can shield the radiation both during and after the beam operation. The dose equivalent rate outside the accelerator hall is below limit for public area during beam time and the accelerator hall is safe for workers to access into one hour after beam-off.

6.5 Conclusion

There is an increasing research field and applications using high power and short pulse THz radiation which can be produced by an accelerator based radiation sources both storage ring and linear accelerator.

Storage rings have potentials to generate such radiation by operating in the low alpha mode to reduce the equilibrium electron bunch length so that the electrons in a bunch radiate coherently in a broad spectrum covering THz frequency range. A new operating mode called “ultra-low alpha operating mode” was tested to shorten the bunch length further for generating shorter radiation pulse and pushing the spectrum of CSR to higher THz frequency. The signal-to-noise ratio from the ultra-low alpha mode needs to be improved in order to achieve better quality of THz CSR.

A linear accelerator based THz radiation has clear advantages over the storage rings in terms of the occupied space and the potential to generate short electron bunches with high peak current. The bunch length is shortened by the bunch compression process provided by a magnetic chicane. Our designs of the compact radiation source based on RF linac for THz SASE FEL and THz CSR provide possible options for the development of the ASL project. Further study was done by using the LPWA to drive the radiation source giving a more compact design of the THz/IR radiation source. However, the transfer line between the LPWA and the undulator need to be investigated in more details in order to

complete a full start-to-end simulation of the LPWA based THz/IR source. The works presented in this thesis demonstrate adequate potentials for the ASL to allow advanced accelerator science research and education in the University of Oxford. The designs of radiation sources are also applicable and affordable to other projects aiming at installing a linac based radiation source in small-scale facilities or universities.

Related Publications

T. Chanwattana, R. Bartolini, A. Seryi, and E. Tsesmelis, "Short Pulses THz FEL for the Oxford Accelerator Science Laboratory", in *Proceedings of the 5th International Particle Accelerator Conference (IPAC2014)*, pp. 2934–2936, (2014).

T. Chanwattana, A. Seryi, and R. Bartolini, "Studies on LPWA-based Light Sources Driven by a Transverse Gradient Undulator", in *Proceedings of the 5th International Particle Accelerator Conference (IPAC14)*, pp. 2937–2939, (2014).

T. Chanwattana, R. Bartolini, A. Seryi, and E. Tsesmelis, "Development of Advanced Fourth Generation Light Sources for the Accelerator Science Laboratory", in *Proceedings of the 6th International Particle Accelerator Conference (IPAC2015)*, pp. 1765–1767, (2015).

T. Chanwattana, M. Atay, R. Bartolini, G. Cinque, M. Frogley, E. Koukovini-Platia, and I. Martin, "THz Coherent Synchrotron Radiation from Ultra-Low Alpha Operating Mode at Diamond Light Source", in *Proceedings of the 7th International Particle Accelerator Conference (IPAC2016)*, pp. 1682–1684, (2016).

Appendix A

Single Particle Dynamics

Charged particles in an accelerator move under the Lorentz force equation for a particle of charge q travelling at velocity of $\vec{v}$

$$\vec{F} = q\left(\vec{E} + \vec{v} \times \vec{B}\right) \tag{A1}$$

which combines together the electric force applied by the electric field $\vec{E}$ and the magnetic force influenced by the magnetic field $\vec{B}$. In the accelerator, the role of the electric force is to accelerate particles, while the magnetic force is used to control the particles' direction of motion.

A.1 Longitudinal dynamics

The main component in accelerators used to accelerate particles is RF cavities which are resonant cavities occupied by electromagnetic fields oscillating at radio frequency. The structure of the RF cavities is designed in a way that the phase velocity of the electromagnetic fields is slower allowing the fields to interact with particles with significant energy exchange. The particle beam is accelerated by the electric field pointing in the desired longitudinal direction. The acceleration continues repetitively if the particles arrive each of the RF cavities in phase with the electric field. This phase is known as synchronous phase

$$\phi_s = \omega t - kz = constant \tag{A2}$$

where ω is the oscillating frequency of the RF fields. The synchronicity condition can be found from the time derivative of Equation (A2) with $\frac{dz}{dt} = \beta c$ as

$$\dot{\phi}_s = \omega - k\beta c = 0. \tag{A3}$$

with the wavenumber defined as

$$k = \frac{2\pi}{L}. \tag{A4}$$

A.2 One turn map in longitudinal phase space in storage rings

For an electron circulating in a storage ring with relativistic speed $\gamma > 1$, the longitudinal phase space variables for position z and relative energy deviation δ are given as

$$z = c(t_s - t) \tag{A5}$$

$$\delta = \frac{E - E_s}{E_s} \tag{A6}$$

where t_s and E_s are synchronous time and energy the electrons arrive in the RF cavity at the phase corresponding to synchronous phase ϕ_s. The change in the longitudinal coordinate in one storage ring circumference L_0 is given by

$$\frac{dz}{ds} \approx \frac{\Delta z}{L_0} = \frac{(-c\Delta T)}{L_0} \tag{A7}$$

which can be expressed in the form of the momentum compaction factor $\alpha_c = \frac{\Delta L/L_0}{\delta} = \frac{c\Delta T}{L_0 \delta}$ as

$$\frac{dz}{ds} = -\alpha_c \delta. \tag{A8}$$

The change in energy deviation in one turn

$$\Delta\delta = \frac{\Delta E}{E_0} = \frac{eV_{RF}}{E_0}(\sin\phi - \sin\phi_s) \tag{A9}$$

with $\phi = \phi_s - \frac{\omega}{c}$ is given by

$$\frac{d\delta}{ds} \approx \frac{\Delta\delta}{L_0} = \frac{eV_{RF}}{L_0 E_0}\left[\sin\left(\phi_s - \frac{\omega}{c}\right) - \sin\phi_s\right]. \tag{A10}$$

The Equations (A8) and (A10) in the discretised form are

$$z_{n+1} = z_n - \alpha_c \delta_{n+1} \cdot \Delta s \tag{A11}$$

$$\delta_{n+1} = \delta_n + \frac{eV_{RF}}{CE_0}\left[\sin\left(\phi_s - \frac{\omega}{c}\right) - \sin\phi_s\right] \cdot \Delta s. \tag{A12}$$

Integrating both in one turn i.e. $\Delta s = L_0$, the one turn map equations of the longitudinal phase space for tracking simulation are expressed by

$$z_{n+1} = z_n - \alpha_c L_0 \delta_{n+1} \tag{A13}$$

$$\delta_{n+1} = \delta_n + \frac{eV_{RF}}{E_0}\left[\sin\left(\phi_s - \frac{\omega_{RF}}{c} z_n\right) - \sin\phi_s\right]. \tag{A14}$$

A.3 Transverse dynamics

Transverse motions of particles in accelerators are controlled by various types of magnets. Linear beam optics is manipulated mainly by dipole and quadrupole magnets. Dipoles are used to bend the particle beam to travel in the desired trajectory, whereas quadrupoles are responsible for transverse beam focussing.

In a circular accelerator, transverse equation of motion can be derived from the Lorentz force equation assuming only transverse magnetic fields. The equation of motion in linear beam dynamics approximation in the horizontal plane is given by

$$x'' + K(s)x = \frac{\delta}{\rho_0} \tag{A15}$$

where x is the horizontal coordinate, $K(s)$ is the focussing strength depending on position on the orbit s, $\delta = \frac{\Delta p}{p_0}$ is the deviation of momentum from the nominal value and ρ_0 is the nominal radius of curvature of the orbit. The focussing strength $K(s) = \frac{1}{\rho^2} - k(s)$ includes

weak focussing from dipoles (the first term) and strong focussing from quadrupoles (the second term).

For the on-momentum particle, the principal solution of the homogenous equation $x'' + K(s)x = 0$ is given by

$$x_0(s) = \sqrt{\varepsilon}\sqrt{\beta(s)}\cos[\,\phi(s) + \phi_0] \tag{A16}$$

here $\beta(s)$ is the betatron (or beta) function which is depending of the beam focussing, $\phi(s) = \int_0^s \frac{1}{\beta(u)} du$ is the betatron phase, and ε and ϕ_0 are integration constants. Equation (A16) demonstrates that the particle undergoes the betatron oscillation in transverse plane by focussing effects applied by the magnet lattice of the ring. Transverse beam size can be determined by the amplitude of betatron oscillation or known as the beam envelope given by

$$\sigma_{x,y}(s) = \pm\sqrt{\varepsilon_{x,y}\beta_{x,y}(s)}. \tag{A17}$$

The transverse beam size can be manipulated by focussing the beta function along the accelerator. The constant ε is the emittance is associated with the area of transverse phase space ellipse.

In case of the off-momentum particles, the general solution is superposition of the principal solution in Equation (A16) and the particular solution in Equation (A15)

$$x_\eta(s) = \eta(s)\delta \tag{A18}$$

here $\eta(s)$ is a dispersion function defined as the dispersive trajectory of the off-momentum particles with the momentum deviation $\delta = 1$. The particles travel on different path depending on their momentum. Therefore, path length of the off-momentum is a function of momentum deviation. In linear beam dynamics approximation, the total path length of a particle is

$$L = \int (1 + Kx)\, ds = L_0 + \int K(s) x_\eta(s)\, ds \tag{A19}$$

where L_0 is the length of the ideal orbit of the on-momentum particles. The deviation path length of the particle with the momentum deviation δ is then

$$\Delta L = \delta \int K(s)\eta(s)\, ds. \tag{A20}$$

From this, the momentum compaction factor is defined as

$$\alpha_c = \frac{\Delta L / L_0}{\delta} \tag{A21}$$

which can be expressed as a power series of the momentum deviation as

$$\alpha_c = \alpha_1 + \alpha_2 \delta + O(\delta^2) \tag{A22}$$

here α_1 and α_2 are the first and second-order momentum compaction factor which can be calculated by

$$\alpha_1 = \frac{1}{L_0} \int_0^{L_0} \frac{\eta_1(s)}{\rho} ds \tag{A23}$$

$$\alpha_2 = \frac{1}{L_0} \int \left[\frac{\eta_1'(s)^2}{2} + \frac{\eta_2(s)}{\rho} \right] ds \tag{A24}$$

where η_1 and η_2 are the first and second-order dispersion expanded in terms of momentum deviation and η_1' is the derivative of the first-order dispersion with respect to the longitudinal coordinate.

A.4 One turn map in transverse phase space in storage rings

Each element in a storage ring, for example drift, dipole, quadrupole and sextupole, can be expressed by a transfer matrix which maps transverse position (x, y) and angle (x', y') at initial longitudinal position s_0 to at final longitudinal position s_1

$$\begin{pmatrix} x \\ x' \end{pmatrix}_{s_1} = M \begin{pmatrix} x \\ x' \end{pmatrix}_{s_0} \tag{A25}$$

$$\begin{pmatrix} y \\ y' \end{pmatrix}_{s_1} = M \begin{pmatrix} y \\ y' \end{pmatrix}_{s_0}. \tag{A26}$$

Multiplication of the matrices for elements in a beamline or a complete storage ring, as shown in Figure A.1 represents the transfer matrix of a beamline or a storage ring,

$$M_{one\ turn} = M_n M_{n-1} \dots M_2 M_1. \tag{A27}$$

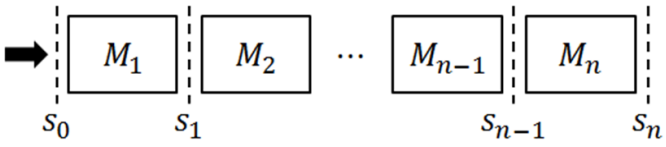


Figure A.1: Schematic of transfer matrices in a beamline for transferring a particle from the longitudinal position s_0 to s_n.

The one turn matrix of the synchronous particle on the ideal orbit is

$$M_{one\ turn} = \begin{pmatrix} \cos(2\pi Q_0) + \alpha \sin(2\pi Q_0) & \beta \sin(2\pi Q_0) \\ -\gamma \sin(2\pi Q_0) & \cos(2\pi Q_0) - \alpha \sin(2\pi Q_0) \end{pmatrix} \tag{A28}$$

where Q_0 is the betatron tune of synchronous particle and α, β, γ are twiss parameters. In case of the off-momentum particle, the momentum deviation induces change in the quadrupole strength $\Delta K = K_0 \delta$, the one turn map can be found by including a quadrupole with infinitesimal length ds which has the transfer matrix given by

$$M_{ds} = \begin{pmatrix} 1 & ds \\ \Delta K ds & 1 \end{pmatrix} \approx \begin{pmatrix} 1 & 0 \\ K_0 \delta ds & 1 \end{pmatrix}. \tag{A29}$$

The one turn map for the off-momentum particle is then

$$\begin{aligned} &M_{one\ turn}(\delta) \\ &= \begin{pmatrix} 1 & 0 \\ K_0 \delta ds & 1 \end{pmatrix} \begin{pmatrix} \cos(2\pi Q_0) + \alpha \sin(2\pi Q_0) & \beta \sin(2\pi Q_0) \\ -\gamma \sin(2\pi Q_0) & \cos(2\pi Q_0) - \alpha \sin(2\pi Q_0) \end{pmatrix} \end{aligned} \tag{A30}$$

which can also be written in the basic form as Equation (A28) with the new tune Q as

$$M_{one\ turn}(\delta) = \begin{pmatrix} \cos(2\pi Q) + \alpha \sin(2\pi Q) & \beta \sin(2\pi Q) \\ -\gamma \sin(2\pi Q) & \cos(2\pi Q) - \alpha \sin(2\pi Q) \end{pmatrix}. \tag{A31}$$

Since both matrices in Equation (A30) and (A31) are the same transformation, their traces should be the same

$$\frac{1}{2}Tr\left(M_{one\ turn}(\delta)\right) = \cos(2\pi Q) \\ = \cos(2\pi Q_0) + \frac{1}{2}K_0\delta\beta\sin(2\pi Q_0)\,ds. \tag{A32}$$

Expressing the new tune as $Q = Q_0 + dQ$ with small dQ, we have

$$\cos(2\pi Q) \approx \cos(2\pi Q_0) - 2\pi\sin(2\pi Q_0)\,dQ \tag{A33}$$

and comparing with Equation (A32) gives $dQ = -\frac{\delta}{4\pi}K_0\beta ds$ therefore the total tune shift in one turn is

$$\Delta Q = -\frac{\delta}{4\pi}\oint K_0\beta ds. \tag{A34}$$

According to the definition of relative chromaticity

$$\xi = \frac{\Delta Q/Q_0}{\delta} = -\frac{1}{4\pi Q_0}\oint K_0\beta ds, \tag{A35}$$

the new turn is a function of chromaticity and the momentum deviation given by $Q = Q_0(1 + \xi\delta)$.

The one turn map from nth turn to (n+1)th turn in transverse phase space depends on tune, chromaticity and momentum deviation and is expressed by

$$\begin{pmatrix} u_i \\ u_i' \end{pmatrix}_{n+1} = M[Q_0(1 + \xi_u\delta_n)] \cdot \begin{pmatrix} u_i \\ u_i' \end{pmatrix}_n \tag{A36}$$

where u defines whether in horizontal (x) or vertical (y) phase space.

Bibliography

[1] B. M. Fischer, M. Walther, and P. U. Jepsen, “Far-infrared vibrational modes of DNA components studied by terahertz time-domain spectroscopy", *Phys. Med. Biol.*, vol. 47, no. 21, pp. 3807–3814, (2002).

[2] R. J. Steed, M. D. Frogley, M. Matthews, E. Clarke, R. Murray, C. C. Phillips, H. Luo, and H. C. Liu, “Angular momentum kinetics in intersubband transitions in semiconductor quantum wells", *Phys. Rev. B*, vol. 78, no. 20, p. 205319, (2008).

[3] G. Cinque, M. D. Frogley, and R. Bartolini, “Far-IR/THz Spectral Characterization of the Coherent Synchrotron Radiation Emission at Diamond IR Beamline B22", *Rend. Lincei*, vol. 22, no. S1, pp. 33–47, (2011).

[4] lightsources.org, “Terahertz Radiation or T-Rays”. [Online]. Available: http://www.lightsources.org/terahertz-radiation-or-t-rays. [Accessed: 01-Aug-2016].

[5] I. F. Akyildiz, J. M. Jornet, and C. Han, “Terahertz band: Next frontier for wireless communications”, *Phys. Commun.*, vol. 12, pp. 16–32, (2014).

[6] D. A. Valverde-Chá vez, C. S. Ponseca Jr, C. C. Stoumpos, A. Yartsev, M. G. Kanatzidis, V. Sundströ, and D. G. Cooke, “Intrinsic femtosecond charge generation dynamics in single crystal $CH_3NH_3PbI_3$”, *Energy Environ. Sci. Energy Environ. Sci*, vol. 3700, no. 8, pp. 3700–3707, (2015).

[7] A. Y. Pawar, D. D. Sonawane, K. B. Erande, and D. V. Derle, “Terahertz technology and its applications”, *Drug Invent. Today*, vol. 5, no. 2, pp. 157–163, (2013).

[8] D. K. Polyushkin, I. Márton, P. Rácz, P. Dombi, E. Hendry, and W. L. Barnes, “Mechanisms of THz Generation from Silver Nanoparticle and Nanohole Arrays Illuminated by 100 fs Pulses of Infrared Light”, *Phys. Rev. B*, vol. 89, no. 12, p. 125426, (2014).

[9] S. E. Korbly, A. S. Kesar, J. R. Sirigiri, and R. J. Temkin, “Observation of frequency-locked coherent terahertz Smith-Purcell radiation”, *Phys. Rev. Lett.*, vol. 94, no. 5, p. 054803, (2005).

[10] A. S. Müller, I. Birkel, B. Gasharova, E. Huttel, R. Kubat, Y. L. Mathis, D. A. Moss, W. Mexner, R. Rossmanith, M. Wuensch, P. Wesolowski, F. Pérez, M. Pont, and C. J. Hirschmugl, "Far Infrared Coherent Synchrotron Edge Radiation at ANKA", in *Proceedings of the IEEE Particle Accelerator Conference*, pp. 2518–2520, (2005).

[11] A.-S. Müller, I. Birkel, S. Casalbuoni, B. Gasharova, E. Huttel, Y.-L. Mathis, D. A. Moss, N. Smale, and P. Wesolowski, "Characterizing THz Coherent Synchrotron Radiation at the ANKA Storage Ring", in *Proceedings of the European Particle Accelerator Conference (EPAC'08)*, pp. 2091–2093, (2008).

[12] A. S. Muller, F. Caspers, A. Scheuring, N. Smale, B. Kehrer, M. J. Nasse, A. Semenov, M. Schwarz, P. Probst, C. Meuter, E. Brundermann, M. Siegel, E. Huttel, M. Streichert, A. Hofmann, K. Ilin, S. Marsching, M. Klein, A. Plech, H. W. Hubers, V. Judin, S. Naknaimueang, N. Hiller, and M. Schuh, "Experimental Aspects of CSR in the ANKA Storage Ring", *ICFA Beam Dyn.Newslett.*, vol. 57, pp. 154–165, (2012).

[13] X. Huang, J. Safranek, J. Corbett, Y. Nosochkov, J. Sebek, and A. Terebilo, "Low Alpha Mode for SPEAR3", in *Proceedings of the IEEE Particle Accelerator Conference*, pp. 1308–1310, (2007).

[14] J. Safranek, "Short Bunches in SPEAR", in *Presentations in Topics in Coherent Synchrotron Radiation: Experimental Consequences of Radiation Impedance*, (2010).

[15] A. Streun, K. Manukyan, D. Gishyan, A. Sargsyan, V. Schlott, N. Milas, F. Müller, H. Sigg, M. Böge, and G. Amatuni, "Low-Alpha Operation of the SLS Storage Ring", in *Proceedings of the 23rd Particle Accelerator Conference (PAC09)*, pp. 2285–2287, (2009).

[16] J. Feikes, K. Holldack, P. Kuske, and G. Wuestefeld, "Compressed Electron Bunches for THz Generation - Operating BESSY II in a Dedicated Low Alpha Mode", in *Proceedings of the 9th European Particle Accelerator Conference (EPAC2004)*, pp. 2290–2292, (2004).

[17] M. A. Tordeux, J. Barros, A. Bence, P. Brunelle, N. Hubert, M. Labat, A. Nadji, L. Nadolski, and C. Evain, “Low-Alpha Operation for the SOLEIL Storage Ring”, in *Proceedings of the 3rd International Particle Accelerator Conference (IPAC2012)*, pp. 1608–1609, (2012).

[18] I. Martin, G. Cinque, G. Rehm, R. Bartolini, and C. Thomas, “Operating the Diamond Light Source in Low Alpha Mode for Users”, in *Proceedings of the 4th International Particle Accelerator Conference (IPAC2013)*, pp. 246–248, (2013).

[19] E. Karantzoulis, A. Carniel, and S. Krecic, “Low Momentum Compaction Optics for ELETTRA”, in *Proceedings of the 2nd International Particle Accelerator Conference (IPAC2011)*, pp. 2963–2965, (2011).

[20] G. P. Gallerano and S. Biedron, “Overview of Terahertz Radiation Sources”, in *Proceedings of the 26th International Free Electron Laser Conference (FEL2004)*, pp. 216–221, (2004).

[21] M. Gensch, “Super-Radiant Linac-Based THz Sources in 2013”, in *Proceedings of the 35th International Free-Electron Laser Conference (FEL2013)*, pp. 474–476, (2013).

[22] J. Park, C. Kim, J. Lee, C. Yim, C. H. Kim, J. Lee, S. Jung, J. Ryu, H.-S. Kang, and T. Joo, “Generation, transport, and detection of linear accelerator based femtosecond-terahertz pulses”, *Rev. Sci. Instrum.*, vol. 82, no. 1, p. 013305, (2011).

[23] E. Chiadroni, M. Bellaveglia, P. Calvani, M. Castellano, L. Catani, A. Cianchi, G. Di Pirro, M. Ferrario, G. Gatti, O. Limaj, S. Lupi, B. Marchetti, A. Mostacci, E. Pace, L. Palumbo, C. Ronsivalle, R. Pompili, and C. Vaccarezza, “Characterization of the THz radiation source at the Frascati linear accelerator”, *Rev. Sci. Instrum.*, vol. 84, no. 2, p. 022703, (2013).

[24] M. Gensch, L. Bittner, A. Chesnov, H. Delsim-Hashemi, M. Drescher, B. Faatz, J. Feldhaus, U. Fruehling, G. A. Geloni, C. Gerth, O. Grimm, U. Hahn, M. Hesse, S. Kapitzki, V. Kocharyan, O. Kozlov, E. Matyushevsky, N. Morozov, D. Petrov, E. Ploenjes, M. Roehling, J. Rossbach, E. L. Saldin, B. Schmidt, P. Schmueser, E. A. Schneidmiller, E. Syresin, A. Willner, and M. V. Yurkov, “New infrared undulator beamline at FLASH”, *Infrared Phys. Technol.*, vol. 51, no. 5, pp. 423–425, (2008).

[25] Z. Wu, A. S. Fisher, J. Goodfellow, M. Fuchs, D. Daranciang, M. Hogan, H. Loos, and A. Lindenberg, "Intense terahertz pulses from SLAC electron beams using coherent transition radiation", *Rev. Sci. Instrum.*, vol. 84, no. 2, p. 022701, (2013).

[26] S. V. Benson, J. R. Boyce, D. R. Douglas, P. Evtushenko, F. E. Hannon, C. Hernandez-Garcia, J. M. Klopf, G. R. Neil, M. D. Shinn, C. D. Tennant, S. Zhang, and G. P. Williams, "The VUV/IR/THz Free Electron Laser Program at Jefferson Lab", *Nucl. Instruments Methods Phys. Res. Sect. A Accel. Spectrometers, Detect. Assoc. Equip.*, vol. 649, no. 1, pp. 9–11, (2011).

[27] M. J. Nasse, M. Schuh, S. Naknaimueang, M. Schwarz, A. Plech, Y. L. Mathis, R. Rossmanith, P. Wesolowski, E. Huttel, M. Schmelling, and A. S. Müller, "FLUTE: A Versatile Linac-Based THz Source", *Rev. Sci. Instrum.*, vol. 84, no. 2, pp. 2–4, (2013).

[28] F. R. Elder, A. M. Gurewitsch, R. V. Langmuir, and H. C. Pollock, "Radiation from Electrons in a Synchrotron", *Phys. Rev.*, vol. 71, no. 11, pp. 829–830, (1947).

[29] M. Eriksson, J. Friso Van Der Veen, and C. Quitmann, "Diffraction-Limited Storage Rings – A Window to the Science of Tomorrow", *J. Synchrotron Rad*, vol. 21, no. 21, pp. 837–842, (2014).

[30] P. Emma, "First Lasing of the LCLS X-Ray FEL at 1.5 Å", in *Proceedings of the 23rd Particle Accelerator Conference (PAC09)*, (2010).

[31] B. McNeil, "Free Electron Lasers: First Light from Hard X-ray Laser", *Nat. Photonics*, vol. 3, no. 7, pp. 375–377, (2009).

[32] J. D. Jackson, *Classical Electrodynamics Third Edition*. (1999).

[33] K. Halbach, "Permanent Magnet Undulators", *Le J. Phys. Colloq.*, vol. 44, no. C1, pp. C1–211–C1–216, (1983).

[34] R. Walker, "Insertion Devices: Undulators and Wigglers", in *CERN Accelerator School: synchrotron radiation and free electron lasers*, CERN-98–04, (1998).

[35] F. Sannibale, J. M. Byrd, Á. Loftsdóttir, M. Venturini, M. Abo-Bakr, J. Feikes, K. Holldack, P. Kuske, G. Wüstefeld, H. W. Hübers, and R. Warnock, "A Model Describing Stable Coherent Synchrotron Radiation in Storage Rings", *Phys. Rev. Lett.*, vol. 93, no. 9, (2004).

[36] P. Schmüser, "Free-Electron Lasers", in *CERN Accelerator School: Intermediate Accelerator Physics Course*, CERN-2006–002, pp. 477–493, (2003).

[37] M. Dohlus, A. Kabel, and T. Limberg, "Optimal Beam Optics in the TTF-FEL Bunch Compression Sections : Minimizing the Emittance Growth", in *1999 Particle Accelerator Conference*, pp. 1650–1652, (1999).

[38] M. Xie, "Design Optimization for an X-ray Free Electron Laser Driven by SLAC Linac", in *Proceedings of the 1995 Particle Accelerator Conference and International Conference of High-Energy Accelerators (PAC95)*, vol. 1, no. l, pp. 183–185, (1995).

[39] S. Reiche, "GENESIS 1.3: A Fully 3D Time-Dependent FEL Simulation Code", *Nucl. Instruments Methods Phys. Res. Sect. A Accel. Spectrometers, Detect. Assoc. Equip.*, vol. 429, no. 1, pp. 243–248, (1999).

[40] R. Bartolini, G. Rehm, J. H. Rowland, and C. Thomas, "Low Alpha Operation of the Diamond Storage Ring", in *Proceedings of the 1st International Particle Accelerator Conference (IPAC2010)*, pp. 4599–4601, (2010).

[41] I. P. S. Martin, R. Bartolini, J. Rowland, B. Singh, and C. A. Thomas, "A Low Momentum Compaction Lattice for the Diamond", in *Proceedings of the 23rd Particle Accelerator Conference (PAC09)*, vol. 1, no. 6, pp. 9–11, (2009).

[42] M. Sands, "The Physics of Electron Storage Rings: An Introduction", in *Proceedings of International School of Physics, Enrico Fermi, Course XLVI: Physics with Intersecting Storage Rings*, vol. C6906161, pp. 257–411, (1970).

[43] D. Robin, H. Hama, and A. Nadji, "Experimental Results on Low Alpha Electron-Storage Rings", in *Workshop on the Production, Measurement and Applications of Short Bunches of Electrons and Positrons in Linacs and Storage Rings*, (1995).

[44] D. Robin, E. Forest, C. Pellegrini, and A. Amiry, “Quasi-Isochronous Storage Rings”, *Phys. Rev. E*, vol. 48, no. 3, pp. 2149–2156, (1993).

[45] CERN-BE/ABP Accelerator Beam Physics Group, “MAD-X, Methodical Accelerator Design”. [Online]. Available: http://madx.web.cern.ch/madx/. [Accessed: 01-Sep-2016].

[46] M. Borland, “Elegant: A Flexible SDDS-Compliant Code for Accelerator Simulation”, *Adv. Phot. Source LS-287*, pp. 1–11, (2000).

[47] I. P. S. Martin, “Short Pulse X-Ray Generation in Synchrotron Radiation Sources”, DPhil thesis, University of Oxford, (2011).

[48] A. W. Chao, *Physics of Collective Instabilities in High Energy Accelerators*. New York: Wiley, (1993).

[49] R. L. Gluckstern, J. Van Zeijts, and B. Zotter, “Coupling Impedance of Beam Pipes of General Cross Section”, *Phys. Rev. E*, vol. 47, no. 1, pp. 656–663, (1993).

[50] V. Smaluk, I. Martin, R. Fielder, and R. Bartolini, “Beam-Based Model of Broad-Band Impedance of the Diamond Light Source”, *Phys. Rev. Spec. Top. - Accel. Beams*, vol. 18, no. 6, p. 064401, (2015).

[51] A. W. Chao, K. H. Mess, M. Tigner, and F. Zimmermann, *Handbook of Accelerator Physics and Engineering*, 2nd ed. World Scientific, 2013.

[52] J. B. Murphy, S. Krinsky, and R. L. Gluckstern, “Longitudinal Wakefield for an Electron Moving on a Circular Orbit”, *Part. Accel.*, vol. 57, pp. 9–64, (1997).

[53] R. Nagaoka, J. Rowland, and R. Bartolini, “Studies of Collective Effects in SOLEIL and Diamond Using the Multiparticle Tracking Codes Sbtrack and Mbtrack”, in *Proceedings of Particle Accelerator Conference 2009*, pp. 4637–4639, (2009).

[54] R. Bartolini, “Numerical Analysis of Collective Effects in Electron Storage Rings”, in *Workshop on Simulations and Computing for Accelerators*, (2011).

[55] E. Koukovini-Platia, M. Apollonio, R. Bartolini, R. Fielder, and I. Martin, “Single Bunch Instability Studies at Diamond Light Source”, in *Proceedings of the 7th International Particle Accelerator Conference (IPAC2016)*, pp. 637–640, (2016).

[56] S. L. Kramer, “Direct Observation of Beam Impedance Above Cutoff”, *Phys. Rev. Spec. Top. - Accel. Beams*, vol. 5, no. 11, p. 112001, Nov. (2002).

[57] G. Cinque, “Private Communication”. (2016).

[58] I. P. S. Martin, G. Rehm, C. Thomas, and R. Bartolini, “Experience with Low-Alpha Lattices at the Diamond Light Source”, *Phys. Rev. Spec. Top. - Accel. Beams*, vol. 14, no. 4, (2011).

[59] A. Finn, P. Karataev, and G. Rehm, “A Multi-Band Single Shot Spectrometer for Observation of Mm-Wave Bursts At Diamond Light Source”, in *Proceedings of the 6th International Particle Accelerator Conference (IPAC2015)*, pp. 1126–1128, (2015).

[60] A. Finn, P. Karataev, and G. Rehm, “Using a Single Shot Spectrometer To Determine the Spectral Characteristics of the Beam As a Result of Micro-Bunching Instabilities”, in *Proceedings of the 7th International Particle Accelerator Conference (IPAC2016)*, pp. 6–9, (2016).

[61] Keit Spectrometers, “FTIR Spectroscopy”. [Online]. Available: http://keit.co.uk/ftir-spectrometer-technology/. [Accessed: 01-Aug-2016].

[62] L. M. Bobb, A. F. D. Morgan, G. Rehm, and D. L. Source, “Streak Camera PSF Optimisation and Dual Sweep Calibration for sub-ps Bunch Length Measurement”, in *Proceeding of IBIC2015*, pp. 206–210, (2015).

[63] Max Planck Institute for Quantum Optics, “The Fastest Stopwatch in the World”, (2004). [Online]. Available: https://www.mpg.de/495195/pressRelease200402241. [Accessed: 01-Aug-2016].

[64] Klaus Floettmann, “ASTRA”, (2011). [Online]. Available: http://www.desy.de/~mpyflo/. [Accessed: 01-Aug-2016].

[65] M. Ferrario, M. Migliorati, and L. Palumbo, “Space Charge Effects”, in *CERN Accelerator School: Advanced Accelerator Physics Course*, CERN-2014–009, pp. 331–356, (2016).

[66] L. Serafini and J. B. Rosenzweig, “Envelope Analysis of Intense Relativistic Quasilaminar Beams in RF Photoinjectors: A Theory of Emittance Compensation”, *Phys. Rev. E*, vol. 55, no. 6, pp. 7565–7590, (1997).

[67] M. Ferrario, L. Serafini, D. T. Palmer, J. E. Clendenin, and J. B. Rosenzweig, “HOMDYN Study for the LCLS RF Photoinjector”, in *Proceedings of the 2nd ICFA Advanced Accelerator Workshop on the Physics of High Brightness Beams*, pp. 534–563, (2000).

[68] Y. Kim, “Accelerator Design and S2E Simulations for Sapphire-I Project”, (2007).

[69] M. Ferrario, K. Flöttmann, B. Grigoryan, T. Limberg, and P. Piot, “Conceptual Design of the XFEL Photoinjector”, (2001).

[70] C. Ronsivalle, L. Giannessi, M. Quattromini, M. Ferrario, L. Ficcadenti, D. Filippetto, V. Fusco, B. Marchetti, M. Migliorati, A. Mostacci, L. Palumbo, C. Vaccarezza, A. Cianchi, A. Bacci, A. R. Rossi, and L. Serafini, “Simulations of the Emittance Compensation in Photoinjectors and Comparison with SPARC Measurements”, in *Proceedings of EPAC 2008*, pp. 21–25, (2008).

[71] M. Dohlus and T. Limberg, “Impact of Optics on CSR-Related Emittance Growth in Bunch Compressor Chicanes”, in *Proceedings of the IEEE Particle Accelerator Conference*, vol. 2005, pp. 1015–1017, (2005).

[72] M. Borland, “Simple Method for Particle Tracking with Coherent Synchrotron Radiation”, *Phys. Rev. Spec. Top. - Accel. Beams*, vol. 4, no. 7, pp. 7–14, (2001).

[73] S. Di Mitri and M. Cornacchia, “Electron Beam Brightness in Linac Drivers for Free-electron-lasers”, *Physics Reports*, vol. 539, no. 1. pp. 1–48, (2014).

[74] J. Marangos, G. Diakun, and R. Walker, “New Light Source (NLS) Project: Conceptual Design Report”, (2010).

[75] J. Yang, F. Sakai, T. Yanagida, M. Yorozu, Y. Okada, K. Takasago, A. Endo, A. Yada, and M. Washio, “Low-Emittance Electron-Beam Generation with Laser Pulse Shaping in Photocathode Radio-frequency Gun”, *J. Appl. Phys.*, vol. 92, no. 3, pp. 1608–1612, (2002).

[76] R. Tikhoplav, G. Kazakevich, D. Mehalcea, and P. Piot, “Manipulation of the Longitudinal Profile”, in *AIP Conference Proceedings*, vol. 877, pp. 694–700, (2006).

[77] W. P. Leemans, B. Nagler, A. J. Gonsalves, C. Tóth, K. Nakamura, C. G. R. Geddes, E. Esarey, C. B. Schroeder, and S. M. Hooker, “GeV Electron Beams from a Centimetre-Scale Accelerator”, *Nat. Phys.*, vol. 2, no. 10, pp. 696–699, (2006).

[78] T. Tajima and J. M. Dawson, “Laser Electron Accelerator”, *Phys. Rev. Lett.*, vol. 43, no. 4, pp. 267–270, (1979).

[79] A. Seryi, *Unifying Physics of Accelerators, Lasers and Plasma*. CRC Press, (2016).

[80] S. M. Hooker, “Developments in Laser-Driven Plasma Accelerators”, *Nat. Photonics*, vol. 7, no. 10, pp. 775–782, (2013).

[81] C. Danson, D. Hillier, N. Hopps, and D. Neely, “Petawatt Class Lasers Worldwide”, *High Power Laser Sci. Eng.*, vol. 3, no. January, p. e3, (2015).

[82] L. Corner, A. Aryshev, G. A. Blair, S. T. Boogert, P. Karataev, K. Kruchinin, L. J. Nevay, N. Terunuma, J. Urakawa, and R. Walczak, “Laserwire: A High Resolution Non-Invasive Beam Profiling Diagnostic”, *Nucl. Instruments Methods Phys. Res. Sect. A Accel. Spectrometers, Detect. Assoc. Equip.*, vol. 740, pp. 226–228, (2014).

[83] S. M. Hooker, R. Bartolini, S. P. D. Mangles, L. Corner, J. Limpert, A. Seryi, R. Walczak, and A. Tünnermann, “Multi-Pulse Laser Wakefield Acceleration: A New Route to Efficient, High-Repetition-Rate Plasma Accelerators and High Flux Radiation Sources”, *J. Phys. B At. Mol. Opt. Phys.*, vol. 47, no. 23, p. 234003, (2014).

[84] E. Esarey, C. B. Schroeder, and W. P. Leemans, “Physics of Laser-Driven Plasma-Based Electron Accelerators”, *Rev. Mod. Phys.*, vol. 81, no. 3, pp. 1229–1285, (2009).

[85] Simon Hooker, “Laser-Plasma Accelerators”, (2015). [Online]. Available: https://www2.physics.ox.ac.uk/research/laser-plasma-accelerators. [Accessed: 01-Aug-2016].

[86] P. McKenna, D. Neely, R. Bingham, and D. Jaroszynski, “Laser-Plasma Interactions and Applications”, *Springer*, (2013).

[87] A. Butler, D. J. Spence, and S. M. Hooker, “Guiding of High-Intensity Laser Pulses with a Hydrogen-Filled Capillary Discharge Waveguide”, *Phys. Rev. Lett.*, vol. 89, p. 185003, (2002).

[88] W. Lu, M. Tzoufras, C. Joshi, F. S. Tsung, W. B. Mori, J. Vieira, R. A. Fonseca, and L. O. Silva, “Generating Multi-GeV Electron Bunches Using Single Stage Laser Wakefield Acceleration in a 3D Nonlinear Regime”, *Phys. Rev. Spec. Top. - Accel. Beams*, vol. 10, no. 6, (2007).

[89] “EPOCH: Extendable PIC Open Collaboration”. [Online]. Available: http://www.ccpp.ac.uk/codes.html. [Accessed: 01-Aug-2016].

[90] Z. Huang, Y. Ding, and C. B. Schroeder, “Compact X-ray Free-Electron Laser from a Laser-Plasma Accelerator Using a Transverse-Gradient Undulator”, *Phys. Rev. Lett.*, vol. 109, no. 20, pp. 1–5, (2012).

[91] M. Fuchs, R. Weingartner, A. Popp, Z. Major, S. Becker, J. Osterhoff, I. Cortrie, B. Zeitler, R. Hörlein, G. D. Tsakiris, U. Schramm, T. P. Rowlands-Rees, S. M. Hooker, D. Habs, F. Krausz, S. Karsch, and F. Grüner, “Laser-Driven Soft-X-ray Undulator Source”, *Nat. Phys.*, vol. 5, no. 11, pp. 826–829, (2009).

[92] T. Chanwattana, A. Seryi, and R. Bartolini, “Studies on LPWA-based Light Sources driven by a Transverse Gradient Undulator”, in *Proceedings of the 5th International Particle Accelerator Conference*, pp. 2937–2939, (2014).

[93] C. Widmann, V. A. Rodriguez, N. Braun, M. Nicolai, A. Papash, M. Reuter, R. Rossmanith, A. Sävert, W. Werner, M. C. Kaluza, A. Bernhard, A. Mueller, and F. Schiller, “Beam Transport System From a Laser Wakefield Accelerator To a Transverse Gradient Undulator”, in *Proceedings of the 5th International Particle Accelerator Conference (IPAC2014)*, pp. 8–11, (2014).

[94] K. Aplin, G. Barr, R. Bartolini, N. Bourgeois, P. Burrows, L. Corner, G. Doucas, C. Foot, G. Gregori, S. Hooker, W. Lau, P. Lau, A. Reichold, A. Seryi, R. Walczak, M. Warren, J. Wark, Stephanie Yang, G. Blair, S. Boogert, P. Karataev, A. Lyapin, S. Molloy, E. Tsesmelis, and L. Rinolfi, "Accelerator Science Lab – updated proposal". (2011).

[95] M. Maslov, M. Schmitz, V. Sychev, M. Maslov, M. Schmitz, and V. Sychev, "Layout Considerations on the 25GeV / 300kW Beam Dump of the XFEL Project", (2006).

[96] K. A. Olive et al., "Review of Particle Physics", *Chinese Phys. C*, vol. 38, (2014).

[97] ICRP, "ICRP 103: The 2007 Recommendations of the International Commission on Radiological Protection", *Ann. ICRP*, vol. 37, (2007).

[98] A. Ferrari, P. R. Sala, A. Fasso, and J. Ranft, "FLUKA: A Multi-Particle Transport Code", no. CERN-2005–010, SLAC-R-773, INFN-TC-05–11. (2005).